Spring 4-30-2020

Advancing Compact Pulsed Power

Jon C. Pouncey
University of New Mexico

Jon Cameron Pouncey

Candidate

Electrical and Computer Engineering

Department

This thesis is approved, and it is acceptable in quality and form for publication:

Approved by the Thesis Committee:

Dr. Jane M Lehr, Chairperson

Dr. Mark Gilmore

Dr. J. Martin Taccetti

Dr. Daniel Banuti

Advancing Compact Pulsed Power

By

Jon Cameron Pouncey

B.S., Electrical Engineering, Florida State University, 2003

M.S., Electrical Engineering, University of New Mexico, 2017

DISSERTATION

Submitted in Partial Fulfilment of the
Requirements for the Degree of

Doctor of Philosophy
Engineering

The University of New Mexico
Albuquerque, New Mexico

May 2020

DEDICATION

To my wonderful and supportive wife, Carmen Hagin, and my loving mother, Elizabeth Pouncey. Without your support and encouragement, I would not have followed my dreams.

ACKNOWLEDGMENTS

First and foremost, I wish to acknowledge the guidance, support, and encouragement of my advisor – Professor Jane Lehr. As her first full-time graduate student, I have had the privilege of collaborating with her on the creation of the UNM Applied Pulsed Energy Ionization and Discharge Center (APERIODIC) and being part of its evolution for the last six years. The energy that I saw in Jane when we first met at the 2013 IEEE Pulsed Power Conference is one of the primary reasons that I came to UNM to pursue my long-deferred goal of a graduate-level education. Her enthusiasm for the benefits that the technology we research can bring to our nation and society is a constant source of inspiration. Her practical outlook on research and conducting the business of the lab is one of the reasons that I have been able to be successful in achieving my research goals. I am proud that my work and I will be forever associated with Jane.

I would also like to thank my other committee members: Professor Mark Gilmore, Dr. Martin Taccetti, and Professor Daniel Banuti for their time and efforts in reviewing this manuscript and attending my defense. I would like to thank Prof. Gilmore for the excellent special topics classes that he has offered over the years. Dr. Taccetti has been kind enough to remain on my committee – despite the fact that I was unable to complete our collaborative project in time to include it in this thesis. I look forward to continuing to work with him in the future. Prof. Banuti deserves special thanks for agreeing to be on my committee at the last minute.

Over the last six years I have had the privilege of working with a number of undergraduate and graduate students in the APERIODIC research group. As the lab manager, I have been honored to assist and mentor these talented colleagues. All of the students who have worked in our lab have contributed in some way to the work described in this manuscript and for that I am eternally grateful.

I have been fortunate enough to have my education supported by two scholarship programs. The first was the Directed Energy Professional Society Graduate Scholarship. I was awarded this generous scholarship for three consecutive years. I would like to extend my thanks to the DEPS director Mr. Mark Niece and the entire DEPS staff. I look

forward to many more years of membership in DEPS. The second scholarship that I was honored with was the Department of Defense Science, Mathematics, and Research for Transformation (SMART) scholarship. Because of this scholarship I was able to pursue the research that I found most interesting without being constrained by the availability of support funding. This scholarship also provided a guaranteed position at a Navy facility that I am excited to go to work for.

The work that we do in the APERIODIC research group would not be possible without the financial support of our sponsors. The work in this thesis was supported by the Office of Naval Research (ONR); the Defense University Research Instrumentation Program (DURIP), and the Air Force Research Laboratory (AFRL).

Advancing Compact Pulsed Power

By
Jon Cameron Pouncey
B.S. Electrical Engineering, Florida State University, 2003
M.S. Electrical Engineering, University of New Mexico, 2017
Ph.D. Engineering, University of New Mexico, 2020

ABSTRACT

The first two decades of the 21st century have seen significant interest in expanding the application of pulsed power technology beyond its traditional use in physics and nuclear weapons research. Applications in the field of national defense, which present unique constraints on system size, have provided impetus to increase the exploration of compact pulsed power solutions. Innovations related to energy density, insulation, switching, and power conversion systems have been realized, bringing deployable compact pulsed power systems closer to realization than ever before. However, recent systems integration efforts have shown that work still remains to develop needed tools and technologies for enabling the successful development of future systems. This dissertation describes efforts to address three of these needs: to develop tools that improve predictive simulation of compact pulsed power systems; to formalize a set of design principles for compact pulsed power systems; and to leverage new technologies developed for commercial applications to advance compact pulsed power.

TABLE OF CONTENTS

LIST OF FIGURES

LIST OF TABLES

COPYRIGHT NOTICE

In reference to IEEE copyrighted material, which is used with permission in this thesis, the IEEE does not endorse any of the University of New Mexico's products or services. Internal or personal use of this material is permitted. If interested in reprinting/ republishing IEEE copyrighted material for advertising or promotional purposes or for creating new collective works for resale or redistribution, please go to http://www.ieee.org/publications_standards/publications/rights/rights_link.html to learn how to obtain a License from RightsLink. If applicable, University Microfilms and/or ProQuest Library, or the Archives of Canada may supply single copies of the dissertation.

CHAPTER 1
INTRODUCTION

1.1 Introduction

The first two decades of the 21st century have seen significant interest in expanding the application of pulsed power technology to systems beyond its traditional use in physics and nuclear weapons research in universities and national laboratories. Applications in the field of national defense, which present unique constraints on size, weight, power, and operating environment, have provided impetus to increase the exploration of compact pulsed power solutions. The development of reliable compact pulsed power systems is recognized as one of the key technological challenges in the development of deployable directed energy systems [1]. Innovations related to high voltage energy storage density [2] [3] [4] [5], insulation technology [6] [7] [8] [9], and power conversion systems [10] [11] [12] have been realized, bringing deployable compact pulsed power systems closer to realization than ever before. However, recent systems development efforts for deployable compact pulsed power systems have shown that many challenges remain. This thesis seeks to address three of these challenges and thus contribute to the advancement of compact pulsed power technology.

1.2 Background

The field of pulsed power has been an application-driven area of research from the beginning. The invention of modern pulsed power is often credited to John Christopher "Charlie" Martin of the UK Atomic Weapons Establishment (AWE) in the late 1950's [13]. His work, driven by the need to generate fast high dose x-ray pulses for flash radiography on a tight budget, was so comprehensive that he certainly deserves the credit [14]. But even before Charlie started testing the limits of pulsed high voltage systems, the need to drive difficult loads with very high power, short pulses had led engineers to use the fastest available switches to discharge high voltage capacitors into minimum-inductance circuits. An early example is the X-unit developed at Los Alamos

during the Manhattan Project. This system, shown in Figure 1, was developed out of the need to deliver microsecond duration kiloampere pulses with nanoseconds of jitter to 32 detonators on the original plutonium implosion nuclear weapon design. While it is relatively low performance by modern standards, the components, layout, and thought processes of the original designers are immediately recognizable to today's pulsed power engineers.

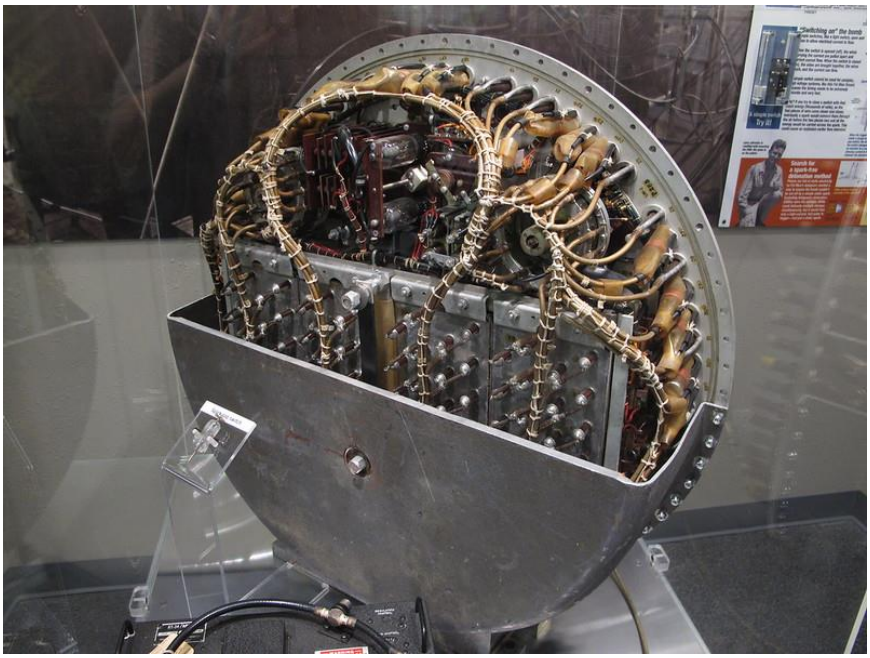

Figure 1 - Photograph of a sectioned example of an original X-unit developed at Los Alamos in 1944-1945 during the Manhattan Project [15].

The basic design consists of high-voltage capacitors discharged by triggered spark gaps through a low-inductance structure into coaxial cables. The novel low-inductance design and spark gaps were disclosed in a patent a number of years after the war as shown in Figure 2. It is instructive to note that the patent was applied for in secret in 1945 but was not publicly issued until 1976 – at which point the technology of pulsed power had advanced well past the design described in the patent.

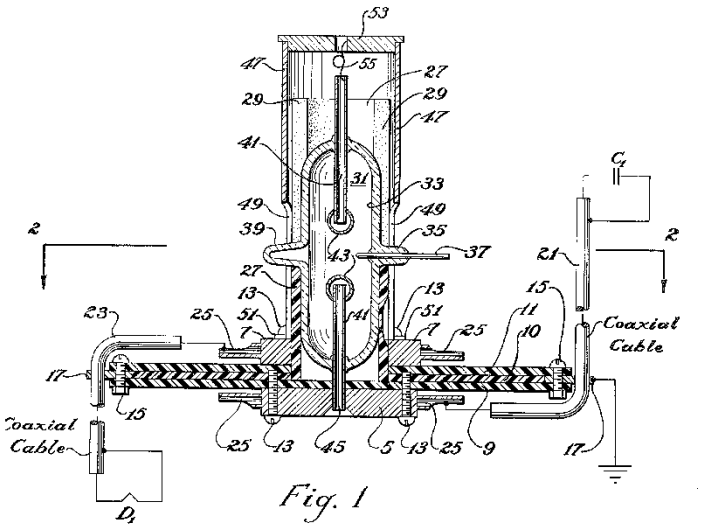

Figure 2 - Figure from US patent 3956658 [16] showing the low-inductance spark gap design from the x-unit shown above. This patent was issued not issued until 1976 for security reasons.

This historical example illustrates that deployable compact pulsed power has been relevant to national defense from the very beginning and that the application almost always drives the development of pulsed power technology – very rarely is pulsed power research undertaken for its own sake. This example also illustrates that, since the applications are often classified as military secrets, the associated pulsed power technology gets wrapped up in the secrecy. These facts impede the development and continuous improvement of a broadly applicable and agreed-upon body of compact pulsed power engineering knowledge. Charlie Martin's greatest contribution was not the experiments that he performed at AWE, but that he framed his investigations in terms of developing usable design principles and scaling laws and that he disseminated this information widely. This led to the use of his work as guidance for the design of systems which continues to the present.

The modern concept of compact pulsed power has been primarily driven by the desire to field high power radio frequency directed energy weapons [1] and other military applications [17]. However, there is no solid criteria for what actually constitutes "compact" pulsed power. As Fazio succinctly put it, "*'compact'… is not the achievement of a minimum size and weight but rather the construction of a device that*

is simply smaller than its predecessor or other similar devices of the time" [18]. Usually, the limitations of the application's intended platform drive the size requirements of the pulsed power system; thus, shipboard compact pulsed power can be significantly different in size and weight than airborne compact pulsed power. Despite the understanding that pulsed power is necessary to enable these applications, the idea of contributing significant resources to compact pulsed power research is hampered by the behind-the-scenes nature of this technology. The application or device enabled by the pulsed power system is the exciting part of the program – a situation best illustrated by the Popular Science magazine illustration shown in Figure 3. This figure unintentionally provides an accurate insight into the perceived relative importance of the load versus the pulsed power, as the focus is the microwave source, while the "power source," i.e. pulsed power system, is cropped out of the picture despite the fact that it would be the most difficult part to develop for deployment of such a system on a UAV.

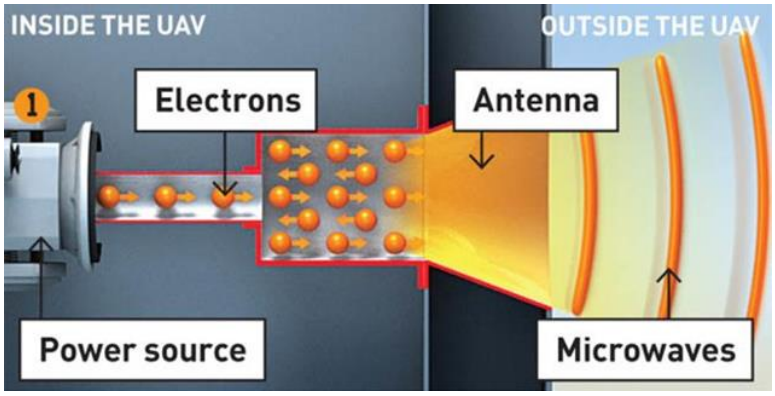

Figure 3 - Illustration of a notional high-power microwave system from the magazine Popular Science [19].

1.3 Research Topics

The first research topic presented in this thesis seeks to address the need for tools that improve predictive simulation of compact pulsed power systems. The principal challenge in satisfying this need is to develop simulation models of components unique to pulsed power systems for use in commonly used simulation tools. In order to address this challenge, a simple, predictive, parametric model of a spark gap switch has been developed and validated for use in the ubiquitous SPICE circuit simulation software.

The second research topic presented in this thesis seeks to address the need to formalize a set of design principles for compact pulsed power systems. The principal challenge in satisfying this need is to improve understanding of the behavior of pulsed power systems as they are made significantly more compact and lower energy. This understanding would be incorporated into design principles that can be applied early in the development of systems to improve confidence that the system will not require significant redesign late in the development cycle. In order to address this challenge, a detailed analysis of the behavior of the compact Marx generator circuit and guidance for improving operation of these devices has been developed.

The final research topic in this thesis seeks to address the need to leverage new technologies developed for other applications, as historically, commercial support for pulsed power systems has been limited. The principal challenge in satisfying this need is to identify and assess technologies for applicability to compact pulsed power systems. In order to begin addressing this challenge, recently developed diode pumped solid state (DPSS) micro-laser technology was identified as having applicability to pulsed power. To further explore the benefits of this technology, a series of original experiments using a commercial micro-laser to trigger gas switches were conducted.

1.3.1 SPICE Modeling of Gas Switches

The use of SPICE-based software for the simulation of pulsed power systems – even large complex systems – has become commonplace in the pulsed power community. This is in contrast to earlier work in the field that relied on specially developed simulation codes such as Sandia's SCREAMER or the Navy Research Lab's BERTHA which natively incorporated models for common pulsed power components like spark gap switches. Unlike these programs, SPICE programs provide a simple and familiar user interface and wide availability. However, SPICE programs do not include realistic models for key pulsed power circuit devices – including the spark gap switch. While simple switch models do exist in SPICE programs, these can only crudely approximate the behavior of a spark gap. The effort described in CHAPTER 2 focuses on developing a

SPICE circuit model for a gas-filled spark gap switch that is physically realistic while being simple enough to permit simulations to run in reasonable times on typical personal computers. Detailed information is provided for implementation in two common versions of SPICE: LTspice and ORCAD PSPICE. Adaptation to other SPICE programs is possible with minimal modification. The model is intended as a design tool that uses physical parameters as inputs to connect it directly to the development of useable pulsed power systems. Data collected from the operation of a high-pressure pulsed-charged switch and a complete 12-stage Marx generator has been used to demonstrate the implementation and accuracy of the model over a wide range of parameters.

1.3.2 Erection Dynamics of Compact Marx Generators

In recent decades, Marx generators have trended towards more compact topologies and have increasingly been used as part of high-power electromagnetic sources. The compact geometry is typically accomplished by limiting the circuit design to the minimal stage components according to the well-known theory of Marx erection with operational goals of hundreds of kilovolts at low energies per pulse. The ease with which these simple generators can be assembled belies the difficulty encountered in obtaining the performance seemingly predicted by the prevailing theory of operation. One often unanticipated behavior is a failure of the Marx to erect when the first gap is triggered. CHAPTER 3 begins with a detailed circuit analysis of a compact Marx generator to examine the root causes limiting the erection process. This is followed by addressing the design considerations that can be used to help ensure that a compact Marx design will exhibit good erection performance.

1.3.3 Micro-laser Triggered Gas Switches

The use of lasers to initiate the closure of high-power gas switches was initially explored soon after the development of suitable high-power pulsed lasers in the 1960's. The low jitter, excellent triggering range, and galvanic isolation provided by laser triggering has been extensively exploited in the triggering of megavolt switches in large pulsed power machines. The fact that the lasers and optical systems used in these machines are very

large, complex, and expensive has led to the perception that these are unavoidable characteristics of laser triggered gas switches, leading to a reluctance among the directed energy and compact pulsed power community to consider their use in compact pulsed power systems.

Fortunately, the large commercial application base of laser technology has continued to drive the development of miniature laser systems, some of which operate in a parameter space that has application to the triggering of gas switches. In particular, the technology of diode-pumped solid-state passively Q-switched micro-lasers was developed in the 1990's. These lasers are capable of producing nanosecond pulses with peak power in the 10's of kilowatts from packages smaller than an AA battery. This opens the possibility of integrating the laser into the switch, thus significantly simplifying the optical design while offering the benefits of laser triggering to the field of compact pulsed power.

CHAPTER 4 describes a series of laser triggering experiments undertaken using a commercially available erbium-doped glass micro-laser. This 28 mm long by 9 mm diameter laser produces 4 ns pulses at 1535 nm with an average energy per pulse of 244 μJ. One of the principal advantages of this laser is that, due to the wavelength and energy, it is a class 1 laser and can be operated without the stringent controls and safety precautions necessary for the lasers typically used for triggering of gas switches. These experiments have demonstrated the feasibility and some of the benefits of using this type of device in a compact pulsed power system.

CHAPTER 2

SPICE MODELING OF GAS SWITCHES[1]

2.1 Introduction

Lumped element circuit simulation software using the SPICE algorithm has been used for some time in the modeling of pulsed power systems. Elements like capacitors, inductors, and even transmission lines can be easily incorporated into simulations via models native to the SPICE environment. Spark gap switches, however, are not native components of the software and thus must be approximated by some combination of other circuit elements.

Two distinct difficulties are encountered when modeling a spark gap in SPICE. The first is that the abrupt change in the impedance of the spark gap can prevent computational convergence of the simulation solution. The second is the difficulty in accurately modeling the various nonlinear behaviors of a spark gap.

While previous investigators have published various SPICE spark gap models for specific applications [20] [21] [22] [23], we believe that the approach presented here will provide practitioners in the pulsed power field with a tool of broad applicability and useful predictive capabilities. The available scaling expressions for key physical phenomena have been brought together with the intent to provide a physics-based model which accurately predicts the behavior of an air insulated spark gap. In the proposed spark gap model, the inputs to the code are the gas pressure, gap capacitance, and the gap length.

2.2 SPICE Simulation Algorithm

SPICE is a general-purpose circuit simulation program for nonlinear dc, nonlinear transient, and linear ac analyses developed as a teaching tool at the University of

[1] Reproduced from: J. C. Pouncey and J. M. Lehr, "A Parametric SPICE Model for the Simulation of Spark Gap Switches," *Review of Sci. Inst.,* vol. 91, no. 3, 2020, with the permission of AIP Publishing. https://aip.scitation.org/doi/10.1063/1.5142006

California - Berkeley for the nascent integrated circuits industry. It is a modified nodal solver governed by Kirchoff's Current Law with each of the components being fed by branches. Circuits may contain resistors, capacitors, inductors, mutual inductors, independent voltage and current sources, four types of dependent sources, lossless and lossy transmission lines, switches, uniform distributed RC lines, and the five most common semiconductor devices: diodes, BJTs, JFETs, MESFETs, and MOSFETs. The name SPICE, an acronym for Simulation Program with Integrated Circuit Emphasis, was coined by its co-creator, Larry Nagel, who received his PhD for its development. It was first presented at Midwest Symposium on Circuit Theory on April 12, 1973 in Waterloo, Canada by Professor Donald O. Pederson [24]. SPICE was public domain and within a few years, it was widely used in electrical engineering classes in many universities. Those students brought SPICE into the rapidly expanding integrated circuit industry and its use proliferated.

Pulsed power applications use the transient analysis, where components are represented in differential or integral form. SPICE solves the ordinary differential equation numerically with an iterative method at each time step. An initial guess at the node voltages is created and the slope and intercept of the tangent to the actual I-V curve is used to calculate a linear approximation of the nonlinear element. Warwick [25] explains the SPICE algorithm: "The linear approximation - a conductance and a current source - is inserted into the conductance matrix as a proxy for the real device. Solution of the linear proxy yields better guess at the voltage vector. A new set of conductance/current source proxies is calculated using tangents at the new voltages. This is repeated until convergence is reached for that time step."

SPICE uses variable time steps. The initial voltage vector guess for each time step is the converged solution of the previous step. If the time step causes accuracy problems, SPICE corrects by disregarding that calculation and taking a smaller step from the previous time point. Convergence problems arise when a device has large conductance swings. This was first identified with the introduction of the MOSFET model by Hodges. The large conductance swing is similar to that found with spark gaps.

SPICE was primarily developed for the simulation and design of low-voltage, low-power systems and the convergence tolerances of the simulation solution parameters have been set to values that are consistent with those applications. Pulsed power circuits, with their typically large rates of change in voltage and current, often exceed these small convergence tolerances – leading to unanticipated difficulties. Fortunately, SPICE applications typically allow the user to change the values of these tolerances. A second issue that often arises in the simulation of pulsed power systems is the fact that the impedances in these circuits are often highly reactive – which further exacerbates the issue of very high rates of change. Furthermore, if one includes the necessary stray reactances in the pulsed power circuit, numerous resonances will exist and can quickly overtax the simulation. This issue is further compounded by the perfect nature of the reactive components provided in SPICE software. Without the addition of suitable lossy elements such as parasitic resistances, the oscillations of these resonances will be undamped and grow without bound – leading to simulation failure.

2.3 Description of Model

2.3.1 Assumptions

While it has been the goal to make the model described in this paper as generally applicable as possible, certain assumptions have been made in order to provide some bounds to the scope of the problem. First, it has been assumed that this model will be used to simulate gas spark gaps with gas pressure and electrode spacing that put operation well to the right of the Paschen minimum. It has also been assumed that the model will be used to simulate spark gaps used as switches where the external circuit will be capable of providing the current necessary to ensure the transition to a true arc mode of operation. It has also been assumed that the user will provide certain input parameters for the model. In particular, the gap separation distance, gas pressure, and stray capacitance are the minimum input parameters for the model as presented.

2.3.2 Software

Since SPICE is a class of circuit simulation algorithms – not a specific application – one must make a choice of which actual SPICE-based simulation program to use. The initial implementation of this model was done in the LTspice application. LTspice, a program developed by semiconductor manufacturer Linear Technology Corp, has become very prevalent due to its ease of use, continuous improvement, and free availability. LTspice also has some advantages over other SPICE implementations when it comes to the simulation of pulsed power circuits. In particular, the LTspice transient algorithm has been optimized for the simulation of switching power converter circuits, which have similar challenges in simulation convergence to pulsed power circuits.

It is also desirable, for the sake of widespread adoption of this model, for it to be implemented in a way that makes for easy adaptation to other SPICE programs. The original implementation in LTspice was made with this in mind. In section 2.4, the adaptation of this model to the commercial ORCAD PSPICE application is described as an example.

2.3.3 Notation

In this chapter, the following notation will be used when referring to the components, parameters, and values of the model. Circuit device names will be identified by bold-face type – e.g. **S_Ch**. Node names will be given in italic font – e.g. *Ch_On*. The voltage at a node will be designated as V(<node name>), likewise the current through a device as I(<device name>) – e.g. V(Ch_on) or I(S_Ch). The names of model parameters will be written enclosed in curly braces, except when they are used in equations – e.g. {Ron} and Ron+1.

2.3.4 Framework

The model described here is based on a framework that is intended to provide a means of implementing all of the relevant physics of a spark gap switch in a way that can be tailored to the requirements of a particular user. The basic circuit of the spark gap, as shown in Figure 4, consists of only two terminals and four elements. The terminals,

nodes *T1* and *T2*, provide the points of interconnection for this model when it is used as a subcircuit in a user simulation. In a physical sense, these points represent the face of each electrode of the spark gap. Any parasitic components of the physical switch under investigation must be added externally. The first element is a behavioral current source, **B_Ind**, which is used to model the parametric inductance of the channel. This is followed by the voltage-controlled switch, **S_Ch**, which models the transition that occurs when a channel initially forms across the entire gap. In series with this switch is the behavioral voltage source, **B_Res**, which is used to model the parametric resistance of the channel. In parallel with the series combination of these three components is **C_Gap**, which represents the fixed capacitance between the gap electrodes and is parameterized by the user input parameter {C}.

Separate from this main circuit are the various behavioral sources and associated circuitry that provide the means of calculating the various parameters that are used to control the behavior of the main circuit elements. The behavioral sources are used to calculate voltages that represent actual physical quantities of the spark gap during operation. These voltages are available at descriptively named nodes. The equations that control each of the behavioral sources can be modified by the user as necessary to implement a preferred model of the physical process.

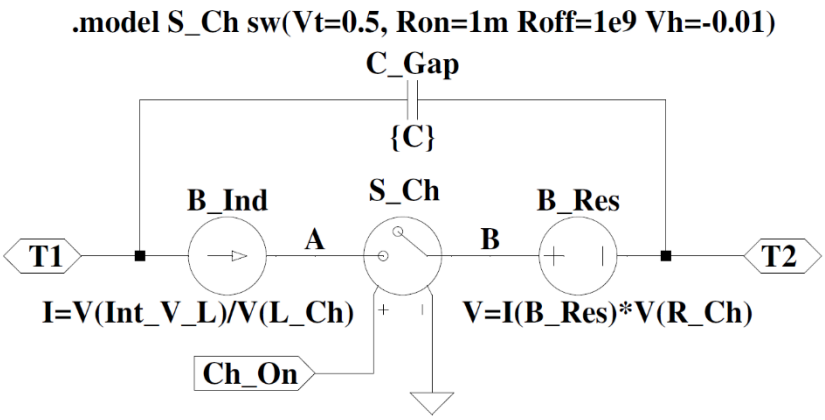

Figure 4 - Main spark gap circuit with elements that simulate the spark gap resistance, inductance, capacitance, and conducting state. These elements are controlled by the circuitry shown in Figure 5 and Figure 6. © 2015 IEEE. Reprinted, with permission, from "A spark gap model for LTspice and similar circuit simulation software," 2015 IEEE Pulsed Power Conference (PPC), Austin, TX, 2015, pp. 1-6.

2.3.5 Breakdown Modeling

The accurate modeling of the breakdown of the gap under the influence of the applied voltage is very important for the accuracy and applicability of the model. Thus, effort has been made to capture all of the various parameters and processes which influence breakdown and incorporate them in the modular framework of this model. The various processes that could influence breakdown are modeled by the circuitry shown in Figure 5.

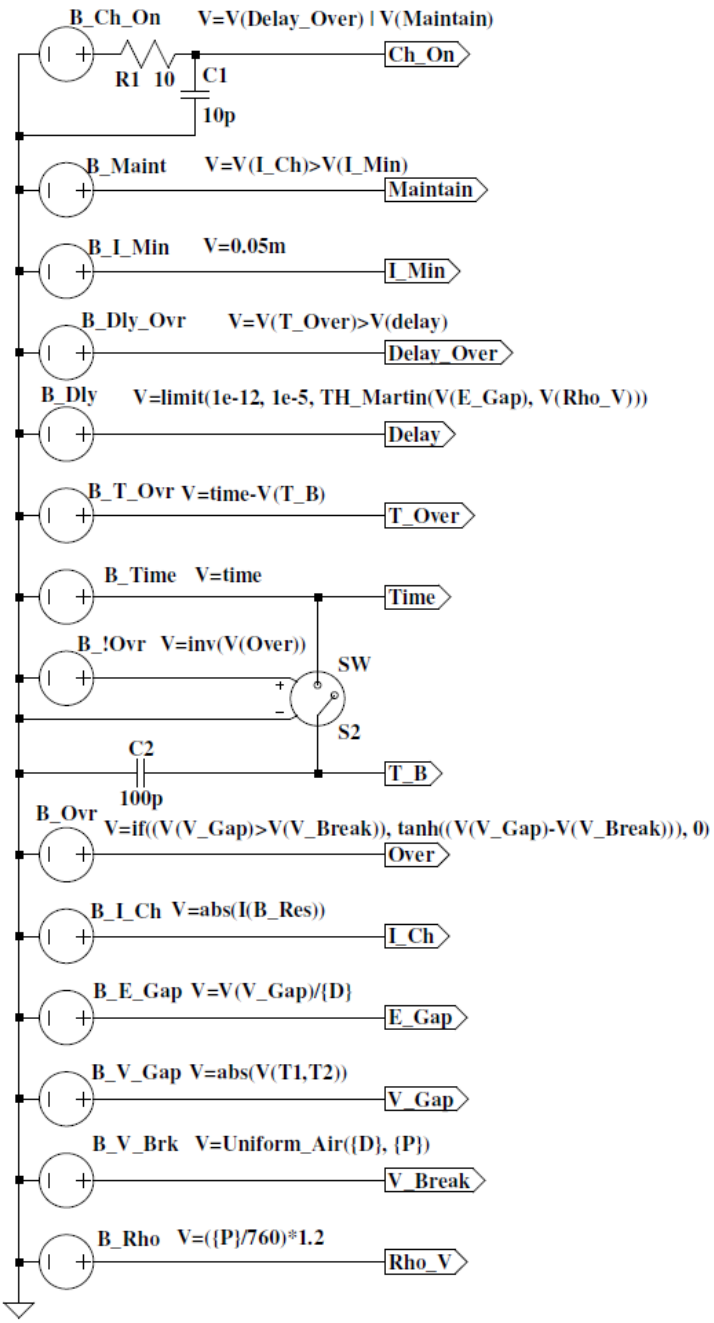

Figure 5 - Breakdown control circuity. Each element calculates a physical parameter that helps to determine the state of the spark gap – either “on” or “off”. This state is ultimately reflected by the voltage at the node Ch_On. © 2015 IEEE. Reprinted, with permission, from "A spark gap model for LTspice and similar circuit simulation software," 2015 IEEE Pulsed Power Conference (PPC), Austin, TX, 2015, pp. 1-6.

2.3.5.1 Control of Channel Closure

In the present model, breakdown is defined as the transition of switch **S_Ch** from the off to the on state. The model statement for **S_Ch** is defined with the parameters for off-state resistance {Roff}, on-state resistance {Ron}, threshold voltage {Vt}, and hysteresis {Vh}. The resistance between nodes *A* and *B* transitions from {Roff} to {Ron} as the voltage at node *Ch_On* varies between Vt-|Vh| and Vt+|Vh|. This transition is controlled by a polynomial function that is inherent to the operation of the switch model in LTspice [26].

The control signal for **S_Ch** is generated at node *Ch_On*. The voltage at node *Ch_On* is generated by the circuit consisting of source **B_Ch_On**, resistor **R1** and capacitor **C1**. Source **B_Ch_On** implements a simple logical OR of the voltages at nodes *Delay_Over* and *Maintain*. LTspice uses a value of 0.5V as the threshold for logical operations. Thus, if the voltage at either node is greater than 0.5V, the output of **B_Ch_On** is 1V; otherwise it is zero. The addition of **R1** and **C1** provides for a finite rise time of the voltage at node *Ch_On* thus leading to a finite transition time for switch **S_Ch**. This time can be made insignificant in comparison to the time scales of interest while still providing a transition that is less likely to lead to simulation errors.

2.3.5.2 Breakdown Delay

One of the two values used to determine the state of **B_Ch_On** and thus the state of the switch **S_Ch** is the voltage at node *Delay_Over*. This voltage is generated by the source **B_Dly_Ovr**. The voltage of this source is determined based on a comparison of the voltage at two additional nodes, *T_Over* and *Delay*, which represent the time that the gap voltage has exceeded the static breakdown voltage and the breakdown delay time, respectively. Thus, when the time that the gap voltage has been higher than the static breakdown voltage exceeds the breakdown delay time, the output of **B_Dly_Ovr** becomes 1V and this in turn drives the output of **B_Ch_On** to 1V and the switch **S_Ch** transitions to the on state.

The overvoltage time, represented by the voltage at node *T_Over*, is generated by source **B_T_Ovr** as the difference between the current simulation time and the most recent time that the gap voltage exceeded the static breakdown voltage. This time is represented, in units of seconds, by the voltage at node *T_B*. This voltage is generated by a sample and hold circuit. The node *Time* is a voltage representing the current simulation time that is generated by the source **B_Time**. Capacitor **C2** is charged to the value of V(Time) under control of switch **S2**. This switch is controlled by the source **B_!Ovr** which has a voltage equal to the logical inverse of the voltage at node *Over*. The value of V(Over) is determined by the relative values of the current gap voltage V(V_Gap) and the static breakdown voltage V(V_Break) through the source **B_Ovr**. The expression for the voltage of **B_Ovr** is an if-then-else that employs a hyperbolic tangent function to smooth the transition from the off to on state in order to eliminate discontinuities that could prevent convergence of the simulation solution. When V(Over) exceeds 0.5V, the output of **B_!Ovr** transitions from 1V to 0V and switch **S1** turns off – freezing the voltage of **C2** and thus the voltage at node *T_B*. This voltage now represents the time at which the overvoltage event began. The value of **C2** is theoretically arbitrary, but smaller values of **C2** limit the size of the current spike that occurs when **S1** re-closes after an overvoltage and thus improve convergence.

For the purposes of this model, the breakdown delay time is considered to be the time between the point at which the gap voltage exceeds the static breakdown voltage and the point at which the channel forms and conduction begins (i.e. the closing of switch **S_Ch**). The delay time, in units of seconds, is represented by the voltage at node *Delay*. This voltage is generated by behavioral source **B_Dly**. The output definition of **B_Dly** is one of the areas of this model for which there is no universally accepted expression and thus it is an area where the user may find benefit in experimentation. The present implementation makes use of the empirical formulation of T.H. Martin [27]:

$$t(E\,,\rho) = 98700\times(E/\rho)^{-3.44}/\rho \quad \text{(s)} \tag{1}$$

where *E* is the average electric field in kV/cm and *ρ* is the gas volume density in g/cm^3. The electric field is calculated by the behavioral source **B_E_Gap** as the ratio of the current gap voltage to the user-input gap separation parameter {D} and is represented as the voltage at node *E_Gap* in units of V/m. The gas volume density is calculated by source **B_Rho** from the ideal gas law using the user input pressure parameter {P} and the STP density of air. The density is represented as the voltage at node *Rho_V* in units of kg/m^3.

While the present implementation of the breakdown delay is deterministic in nature and does not include the random component of the statistical delay, it should be possible to implement a physically realistic statistical delay using the Monte Carlo functions available in LTspice if that behavior is important for a particular user.

2.3.5.3 Static Breakdown Voltage

The static breakdown voltage of the gap is represented in the model as the voltage at node *V_Break*. This voltage is generated by the source **B_V_Brk**. The expression for determining the value of static breakdown voltage is another area in which the user may find it useful to experiment with the various formulations that can be found in the large volume of literature pertaining to gas breakdown. Two different empirical formulations are available in the current implementation. For uniform field gaps filled with air at pressures of up to about 10 atmospheres, the formula of Bruce [28] is applicable:

$$V = 24.22(P/P_0)\text{d}+6.04(P/P_0)^{\frac{1}{2}}d^{\frac{1}{2}} \text{ (kV)} \tag{2}$$

where *P* is the air pressure in the gap, P_0 is standard atmospheric pressure (760 Torr), and *d* is the gap distance in cm. For very small gaps at high pressures, the formulation of Skilling and Brenner [29] is applicable:

$$V = 30(P/P_0)d/\big(1 + 0.009(P/P_0)\big) + 1.7 \text{ (kV)} \tag{3}$$

2.3.5.4 Channel Maintaining Current

After the initial closure of switch **S_Ch** resulting from the action of the breakdown delay circuitry described in the previous section, the voltage across the spark gap will rapidly collapse and current will begin to flow through the components **B_Ind**, **S_Ch**, and **B_Res**. In a physical spark gap, this current maintains a conductive channel through various physical processes. In the present model, an assumption has been made that there is some minimum value of this current that is required to maintain the channel in a conductive state. The value of this minimum current is represented by the voltage at node *I_Min* in units of Amperes. The source **B_Maint** compares the magnitude of the channel current, represented by the voltage at node *I_Ch* with this minimum and generates a voltage of 1V when V(I_Ch) is greater than V(I_Min), otherwise the output is zero.

2.3.6 Channel Dynamics

The dynamic processes that occur after the initial breakdown of the spark gap are often of importance in the application of spark gaps and are thus important in the simulation of spark gaps. The present model seeks to provide a means of simulating these processes in a way that is easy to understand and can be easily tailored by the user to the particular requirements of a problem of interest. The dynamic elements that are modeled are the spark channel resistance and inductance. Figure 6 illustrates the circuitry used to control the simulation of these dynamic components.

2.3.6.1 Channel Resistance

The resistance of the spark channel after breakdown is modeled in the main circuit by voltage source **B_Res**. This source produces a voltage equal to the product of the current through itself and the voltage at node *R_Ch*, which represents the channel resistance in units of Ohms. The voltage at node *R_Ch* is generated by source **B_R_Ch**. Many expressions for the resistance of a spark channel as a function of various parameters have been presented in the literature. A useful overview is provided by Engel et al. [30]. The present implementation of the model includes three such

expressions – those of Vlastos [31], Toepler [32], and Kushner [33] – as user defined functions which may be substituted into the expression for the output of **B_R_Ch**. The proportionality constants for each of these expressions are those proposed by Engel. The expression for **B_R_Ch** also includes a limit function to provide lower and upper bounds on the channel resistance. These limits serve both to represent physical limits as well as to reduce the chances of simulation failure. The upper limit sets the maximum channel resistance that would be measured at the moment that an ionized channel has been established across the gap.

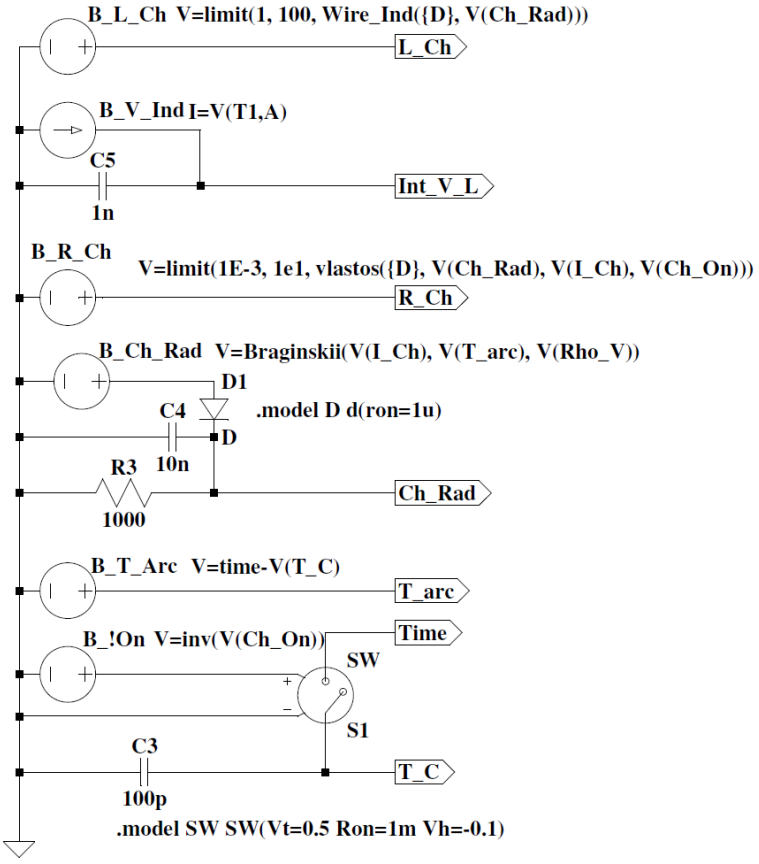

Figure 6 - Channel dynamics control circuitry. Each of these elements calculates a physical parameter that controls the behavior of the spark channel during conduction. © 2015 IEEE. Reprinted, with permission, from "A spark gap model for LTspice and similar circuit simulation software," 2015 IEEE Pulsed Power Conference (PPC), Austin, TX, 2015, pp. 1-6.

Some of these expressions make use of the channel radius as a parameter. Thus, a means has been provided in the present model to calculate the channel radius based on the well-known expression developed by Braginskii [34]:

$$r = 9.3 \times 10^{-4} \left(i^{\frac{1}{3}} \times t^{\frac{1}{2}} / \rho^{\frac{1}{6}} \right) \text{ (m)} \quad (4)$$

where i is the channel current in kA, t is the time since the arc formed in μs, and ρ is the gas density in g/cm^3. This expression is used by source **B_Ch_Rad** to drive the voltage at node *Ch_Rad*, which then represents the arc channel radius in meters. The circuit consisting of **D1**, **C4**, and **R3** has been included because Braginskii's formulation was derived to account for the shock-driven growth of the channel only, and not any contraction or dissipation thereof. Thus, **D1** allows **C4** to charge up to the peak output of **B_Ch_Rad** but then the voltage must decay via **R3**. This mechanism has been added to permit the model to function in a circuit with multiple discharge events – not as a model of the physical contraction or dissipation of the channel. The values of **R3** and **C4** should be chosen to give a relatively long time constant compared to the discharge event so that the simulated channel radius does not contract during the discharge. Alternatively, a switch controlled by the voltage at the *Ch_On* node could be used to keep **C4** discharged (and thus V(*Ch_Rad*) = 0) when the channel is not conducting.

The Braginskii channel radius expression, as well as some of the arc resistance expressions found in the literature, require the time since arc formation as an input variable. Thus, a circuit to calculate the time since the last transition of the switch **S_Ch** from off to on has been incorporated into the model. This time is represented by the voltage at node *T_Arc* and is generated in the same way as the overvoltage time described above using the logical inverse of the voltage at node *Ch_On* as the control signal for the sample and hold circuit that determines the arc start time at node *T_C*.

2.3.6.2 Channel Inductance

The inductance of the spark channel after breakdown is modeled in the main circuit by current source **B_Ind**. This source simulates an inductance by the method described by

Basso in [35]. This method makes use of the fact that the governing differential equation of an inductor can be solved for the inductor current by separation of variables to give:

$$i(t) = \int_0^t v(\tau) d\tau / L \quad (5)$$

This formulation avoids the use of a time-derivative term, which will often produce significant errors in simulations. The voltage across the inductance is converted to a current by source **B_V_Ind** and this current is integrated by capacitor **C5**. This produces a voltage at node *Int_V_L* which is the time integral of the inductor voltage in units of V·s x 10^9. The current produced by **B_Ind** is then set to be the voltage at *Int_V_L* divided by the voltage at node *L_Ch*, which is used to represent the channel inductance in units of nano-Henrys. The voltage at node *L_Ch* is generated by the source **B_L_Ch**. The output of this source may be defined as a constant or as some expression of the other parameters in the model. In the present implementation, the expression for the inductance of an isolated thin wire derived by Grover [36] is used:

$$L = 2d[ln(2d/r)\text{-}0.75] \text{ (nH)} \quad (6)$$

where *d* is the gap distance in cm derived from the user input distance parameter {D} and *r* is the channel radius as determined by the voltage at node *Ch_Rad*. The expression used to calculate the voltage of **B_L_Ch** incorporates limits in order to bound the calculation. The inductance must not be allowed to reach zero, as that would drive the source **B_Ind** to infinite output. The upper limit keeps the output of **B_L_Ch** finite for very small values of channel radius. Thus, when the gap breaks down in the simulation and the channel radius begins to increase from zero, the rate of change of the output of **B_L_Ch** is limited. This reduces the chance of simulation errors.

2.4 Implementation in PSPICE

While the fundamental operation of all SPICE programs is the same, various companies' implementations differ in certain elements and functions. Thus, transferring a model from one version to another may require non-trivial changes. This section provides an example and description of adapting the spark gap model to an implementation in

ORCAD PSPICE. The adapted model has been tested and shown to produce identical results to the LTspice version.

2.4.1 Component Differences

PSPICE does not include the behavioral sources that are available in LTspice. However, the EVALUE and GVALUE expression-controlled sources can be used in their place. On a schematic, these parts have input pins and output pins, but the input pins are unused and should be connected to ground. Figure 7 is an example of the implementation of the static breakdown voltage expression using the EVALUE part in PSIPCE.

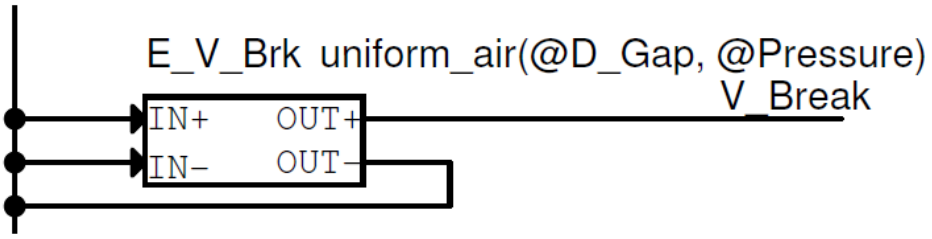

Figure 7 - PSPICE implementation of the static breakdown expression using the EVALUE part. Note that the syntax for passing parameters is the @ symbol instead of the curly braces used in LTspice.

2.4.2 Action Integral Difference

The majority of the expressions used in the LTspice implementation of the model are usable as-is in the PSPICE implementation. The notable exception is the Vlastos channel resistance expression, which includes the time integral of the channel current squared – also known as the action integral. The challenge in implementing this integral in the model is that it is desirable to reset the integral whenever the spark gap transitions from a conducting to a non-conducting state. This permits the model to simulate multiple sequential breakdowns in a single simulation run. In LTspice, this is easy to accomplish in the user defined functions because the LTspice integral function – idt() – includes the ability to reset the integral on the value of a Boolean variable. The PSPICE integral function, which is the same as the original SPICE integral function, does not include this functionality. Thus, for PSPICE, the action integral must be implemented in a circuit. The implementation of the action integral with circuit components is shown in Figure 8.

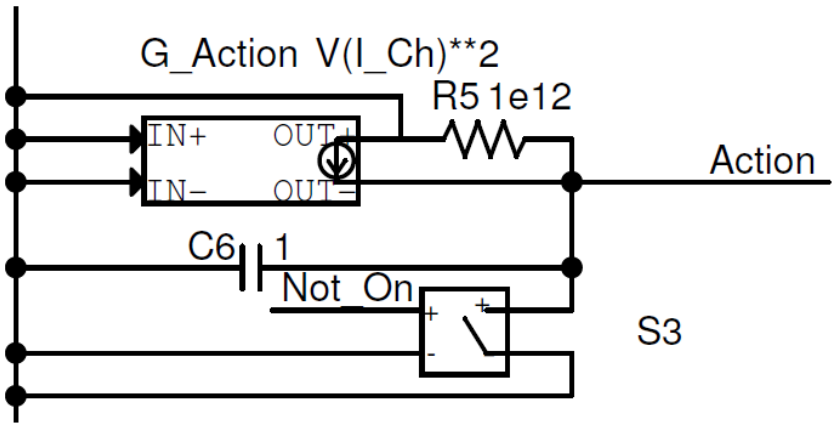

Figure 8 - PSPICE implementation of the calculation of the action integral.

The current source **G_Action** produces a current equal to the square of the channel current as defined by the voltage at node *I_Ch*. This current is integrated into the voltage at node *Action* by capacitor **C6**. Switch **S3**, controlled by the voltage at node *Not_On* dumps the charge from **C6** whenever the gap is in the non-conducting state. The resistor **R5** is necessary to prevent the output node of the current source from floating because PSPICE does not automatically include shunt resistance for current sources. A similar resistance is required across the output terminals of the current source that models the dynamic inductance in the main circuit as well as the current source that performs the integration of the inductor voltage to produce the voltage at node *Int_V_L*.

2.5 Using the Model

2.5.1 Challenges of Simulating Pulsed Power Circuits

As the primary goal of this work is to provide practitioners in the field of pulsed power with a spark gap model that can be used in the simulation of pulsed power circuits, it is necessary to point out some of the challenges that are inherent in the use of SPICE programs for such simulations. Most difficulties arise due to the very large rates of change of voltages and currents within a pulsed power system. Since SPICE programs were primarily developed for the simulation and design of relatively low voltage and

power systems, the convergence tolerances have been set to values that are consistent with those applications. These tolerances are often too small to permit convergence of the solution of a pulsed power circuit. Fortunately, most SPICE applications allow the user to change these tolerances to values more applicable to a pulsed power circuit. A second issue that often arises in the simulation of pulsed power systems is the fact that the impedances in these circuits are often highly reactive, which further exacerbates the issue of very high rates of change of currents and voltages. Furthermore, if one includes the various stray reactances that are common in such circuits in the model, numerous resonances will exist and can quickly overtax the simulation. This issue is compounded further by the perfect nature of the reactive components provided in SPICE software. Without the addition of suitable lossy elements (i.e. parasitic resistances) the oscillations of these resonances will be undamped and thus may grow without bound – leading to simulation failure.

2.5.2 Techniques to Prevent Simulation Failure

Successful simulations of pulsed power systems, like all simulations, require that the experimenter be sufficiently familiar with the physics of the problem as well as the limitations of the simulation tool. This will enable one to determine if the results of a simulation are unreasonable and thus take action to refine the model for more accurate results. In the case of simulating common pulsed power circuits, several techniques have been found to be helpful in obtaining useful results when using the present model. These techniques are discussed in the following sections in order of descending desirability.

2.5.2.1 Addition of Parasitic Elements

It is important to include realistic values for the lossy parasitics of the circuit under consideration. This includes capacitor and inductor series resistances. The addition of a large value shunt resistance on inductors can improve the simulation of circuits where the inductance dominates the load impedance.

2.5.2.2 Changes in Circuit Values

In some cases, simulation failures occur due to the interaction of the values of various circuit components. In these cases, small changes in the values of circuit components – on the order of 1% or less – have resulted in successful simulation convergence. Since the actual resistances, inductances, etc. of a pulsed power circuit are rarely known more accurately than 1%, this technique can often be applied with no real impact on the accuracy of the results.

2.5.2.3 Alternative Simulation Settings

Most SPICE programs allow the user to choose between certain settings of the simulation algorithm. In particular, most SPICE software includes various alternatives for the numerical integration technique used to transform the circuit differential equations into algebraic equations. In some cases, a simulation that fails with the default method will run successfully with an alternative technique. Often, the main sacrifice is in the speed of the simulation. LTspice includes an additional selection of an alternative matrix solver, which can improve simulation convergence by reducing internal rounding errors with some penalty in simulation speed [26].

2.5.2.4 Changing Simulation Tolerances

The final technique that may be used to get a simulation to run successfully is to relax some of the tolerances used by the software. This should only be done when the previously mentioned techniques have failed to yield results and changes should be made in a gradual and methodical manner.

There are four primary tolerances in all SPICE-based simulation software that may be useful in improving simulation convergence. The first is the relative tolerance – denoted RELTOL. This parameter, which generally defaults to 0.001, defines the tolerance for the estimated error of any given node voltage or branch current relative to the present value at each time step of the simulation. This can be thought of as a measure of the relative accuracy of the solution at each point. The next two tolerances

are the absolute current tolerance – denoted ABSTOL – and the voltage tolerance – denoted VOLTOL. These provide lower limits for the tolerance of the branch currents and node voltages, and are particularly important near zero-crossings where the relative tolerance approaches zero. These first three tolerances work together to determine how much estimated error is permitted in the solution at each time step. In general, increasing these tolerances can allow a failing simulation to run – at the expense of reduced accuracy and the increased risk of the appearance of simulation artifacts. The fourth tolerance is the general transient tolerance – denoted TRTOL. This parameter affects the dynamic adjustment of the simulation time step size with larger values permitting more truncation error in the numerical integration before the time step is reduced. Increasing this tolerance will generally permit larger time steps and can allow the simulation to step past a point that is causing convergence problems. However, this can lead to poor results and simulation artifacts. Conversely, reducing this tolerance can sometimes improve simulation success by forcing the algorithm into smaller time steps that improve tracking of the circuit behavior near discontinuities.

2.5.3 Tailoring the Model

The present model has been developed with the intent of providing practitioners in the field of pulsed power engineering with a useful tool for the simulation of pulsed power circuits in commonly available circuit simulation software. Since many of the physical processes at work in a spark gap are still actively under investigation, this model has been built to facilitate incorporation of new models for the various physical processes as new information becomes available. Once the user becomes familiar with the model, changes can be made easily by substituting the desired expression into the value parameter of the applicable behavioral source.

2.6 Experimental Validation 1 - Pulse Charged High Pressure Switch

2.6.1 Experimental Data Source

The first experimental device to be compared with this spark gap model was a high-pressure sub-millimeter gap switch that is pulse charged in under 5 ns. This represents a very high-performance switching application that would be applicable to a sophisticated modulator design. This experiment was conducted by ASR Corporation during a test series intended to explore the properties of various gasses as dielectric media in a compact spark gap switch.

2.6.1.1 Experimental Setup

The experimental setup consisted of a dual-polarity pulse generator (Figure 9) capable of applying a fast-rising pulse to the switch under test and a test cell (Figure 10) to house the switch and provide connection and monitoring. The generator consists of two sets of ceramic capacitors connected by a triggered spark gap switch. These capacitors are differentially charged with an external high voltage supply. When the switch is triggered, two pulses of opposite polarity are launched into the output coaxial cables, which transfer the pulses to the switch under test in the test cell. When the pulses arrive simultaneously at the test cell, a voltage equal to 4 times the initial capacitor charge voltage appears across the switch with a very fast rise time. The voltage at the test cell is monitored by D-dot probes attached to the coaxial cables where they enter the test cell. The waveforms are captured and then processed to yield a voltage measurement. The total voltage across the switch is taken as the difference between the two measured voltages. This setup is capable of applying up to 200 kV to the switch under test in a pulse with a rise time of less than 5 ns.

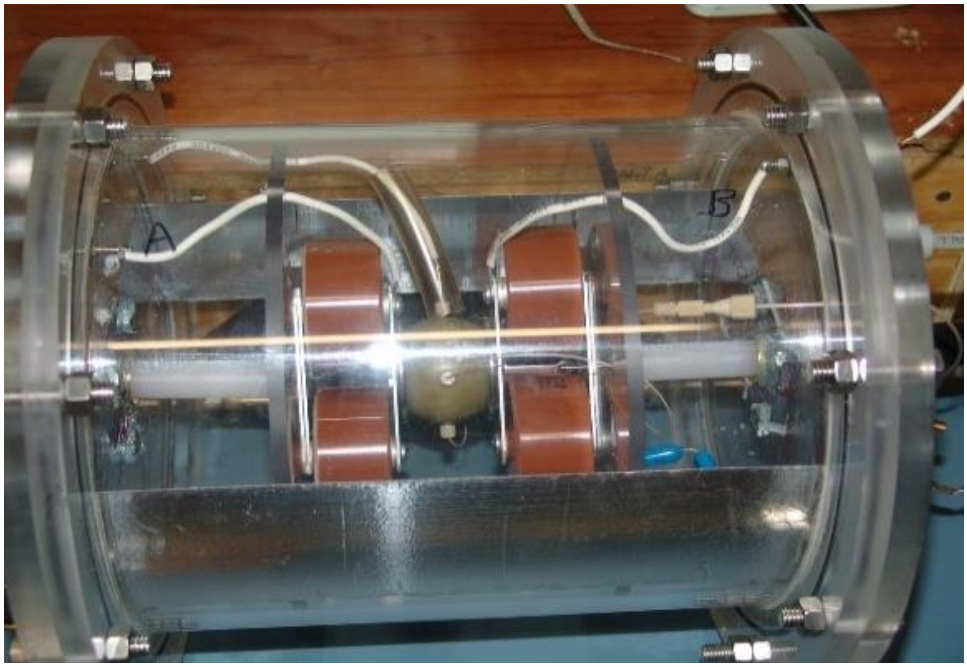

Figure 9 - Photo of pulse generator used in ASR experiment. Capacitors and triggered switch visible inside transparent pressure housing filled with SF6.

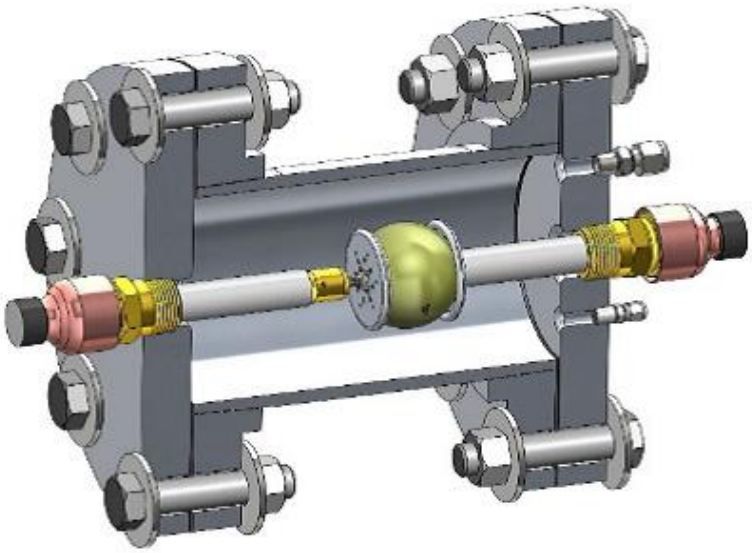

Figure 10 - Rendering of test cell used in ASR experiment. The switch under test is centered in the cylindrical pressure housing by the high voltage coaxial cable feeds. The pressure housing is filled with SF6 during testing, while the switch is filled with Ultra Zero air. D-dot sensors are located on the coaxial cables external to the test cell.

2.6.1.2 Experimental Parameters

The data used for comparison with the spark gap model was taken with the switch under test filled with high purity Ultra Zero air at four different pressures – 100, 600, 1200, and 1800 psig. The switch under test was set up with a gap of 0.64 mm. The Rogowski profile electrodes provide a very uniform field in the gap.

2.6.2 Simulation Model

In order to compare the present spark gap model with the results of these experiments, an accurate model of the experimental apparatus was necessary, as well as the appropriate configuration of the spark gap model.

2.6.2.1 Model of Experimental Apparatus

The experimental apparatus was modeled as shown in Figure 11. Capacitors C1 and C2 represent the ceramic capacitors in the pulse generator. Switches S1 and S2 represent the two halves of the triggered spark gap used to fire the pulse generator. These were used in order to simplify the model, since the details of that switch's operation were not of interest. The nodes V+ and V- are the charging points for the capacitors – they are set to an initial value at the start of the simulation. Resistors R1 and R2 serve as dc ground references for the capacitors. Inductors L1 and L2 represent the stray inductance of the pulse generator. These inductors determine the rise time of the output pulse and their values have been selected such that the rise time in the simulation matches the measured data. The lossy transmission lines O1 and O2 model the RG218 coaxial cables used to connect the pulse generator to the test cell. The nodes Pos_D-dot and Neg_D-dot represent the points at which the actual D-dot sensors are placed on the physical apparatus. The inductors L3 - L6 and capacitors C3 - C6 model the reactive impedance of the test cell assembly as a discrete element transmission line. Their values were derived from the geometry of the test cell. Each pair of elements represents approximately 5 cm of length.

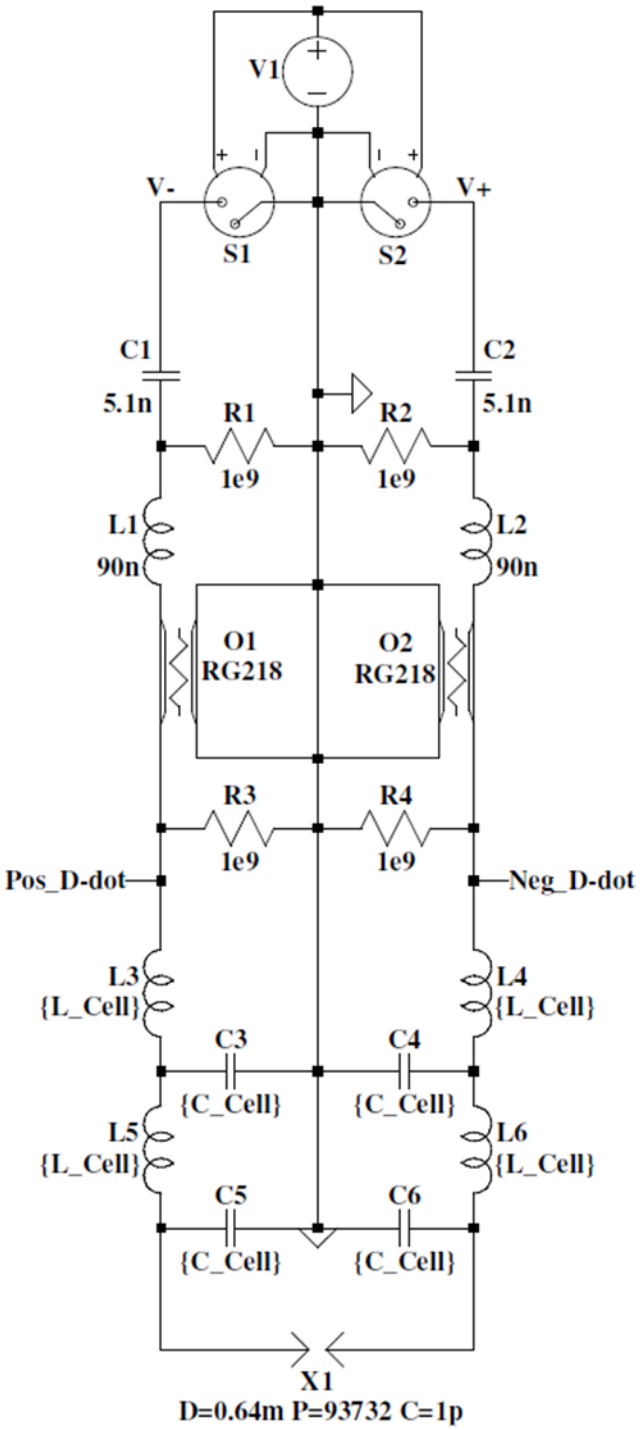

Figure 11 - LTspice simulation circuit for comparison of breakdown data for nanosecond pulse charged switch with spark gap simulation model. Pulse generator is at top of schematic and spark gap under test at bottom.

2.6.2.2 Spark Gap Model Configuration

The spark gap model as described previously was used to simulate the test switch in LTspice. The expression for the static breakdown voltage (3) was that of Skilling and Brenner [29]. The expression for the dynamic channel resistance (7) was that of Vlastos [31]:

$$R = \ c \times d \times r^{\frac{2}{5}} / (\int I^2 \, dt)^{\frac{3}{5}} \tag{7}$$

where *c* is a constant of proportionality given as 876 by Engel et al. [30], *d* is the gap distance, *r* is the channel radius calculated using the formula developed by Braginskii [34], and *I* is the channel current. The actual gap spacing and gas pressure from the experiments were provided as inputs to the model. The gap capacitance was calculated based on the known geometry of the gap electrodes.

2.6.2.3 SPICE Tolerances and Parameters

The SPICE tolerances in LTspice were left at the default values with the exception of the value of TRTOL which was set to 0.1. The solver was set to *Alternate* as this has proven to provide more stable simulations using the spark gap model with only a slight increase in simulation time.

2.6.3 Result Comparison

The comparisons of the simulation results with the measured data at each of the four test pressures are given in Figure 12 through Figure 15. In each figure, the red trace is the simulation data. The timing of the experimental data has been offset such that the upper part of the rising edges coincides with the simulation waveform. It can be seen that the simulation waveforms all fall within the spread of the experimental data and exhibit very similar waveform shape.

The only significant difference is the early “knee” in the experimental data that is absent from the simulation data. This feature could not be replicated through simulation in SPICE – so it was theorized that it must be an electromagnetic effect due to the physical size of the switch test fixture. This was investigated through the use of a

time domain full electromagnetic simulation of the test fixture in the CST Microwave Studio simulation package. Using this simulation, it was discovered that the rising edge of the pulse that feeds into the fixture is partially coupled as an electromagnetic wave through the fixture to the opposite input cable where it is picked up by the D-dot sensor on that side. Since the cross-coupled signals are of the opposite polarity of the main signal on each side, they inject a negative spike into each D-dot signal that leads to the step in the integrated voltage plot. The timing of the step corresponds to the time of flight across the fixture for the electromagnetic wave.

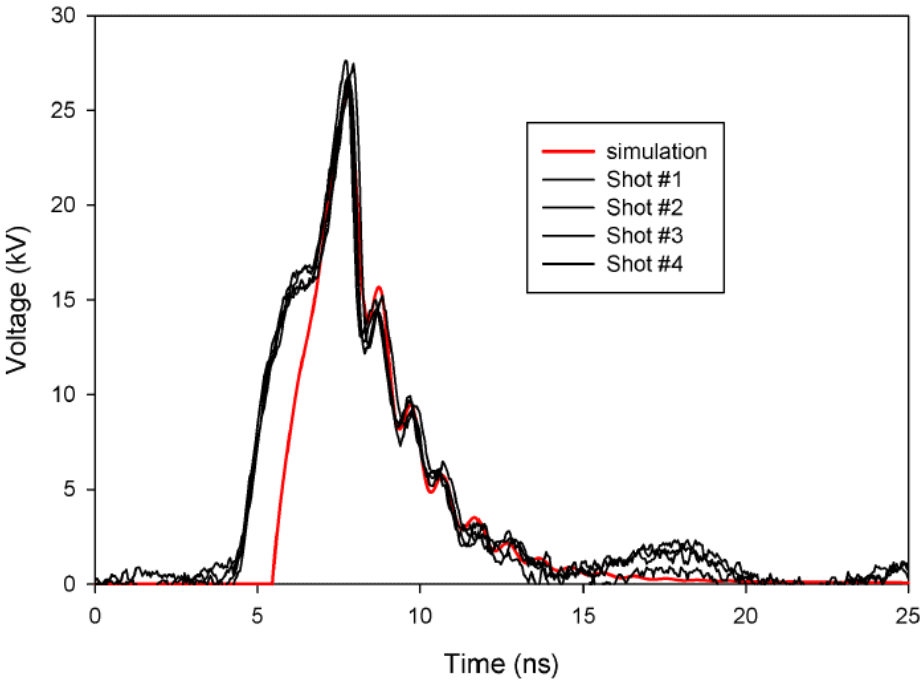

Figure 12 - Simulation vs. experimental data – spark gap pressure of 100 psig and a charge voltage of 10 kV. The red line is the simulated waveform. The black lines are representative experimental shots.

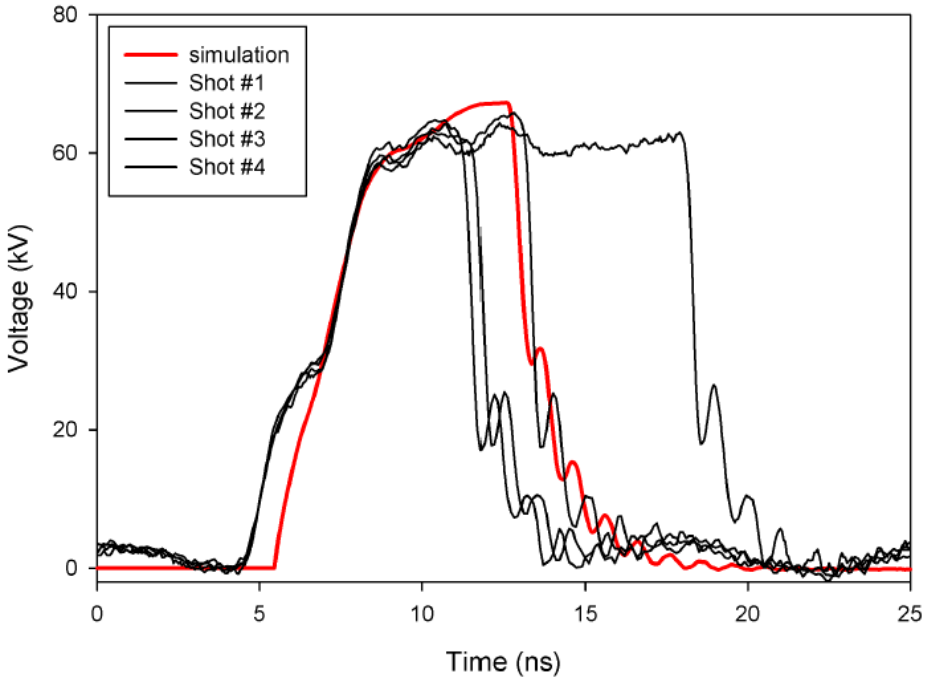

Figure 13 - Simulation vs. experimental data – spark gap pressure of 600 psig and a charge voltage of 17.5 kV. The red line is the simulated waveform. The black lines are representative experimental shots.

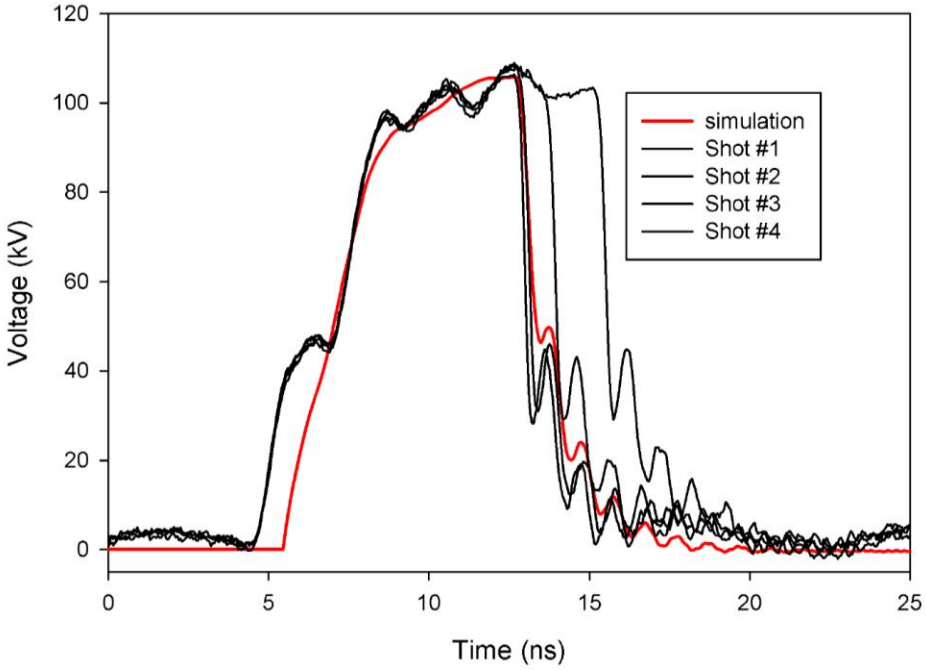

Figure 14 - Simulation vs. experimental data – spark gap pressure of 1200 psig and a charge voltage of 27.5 kV. The red line is the simulated waveform. The black lines are representative experimental shots.

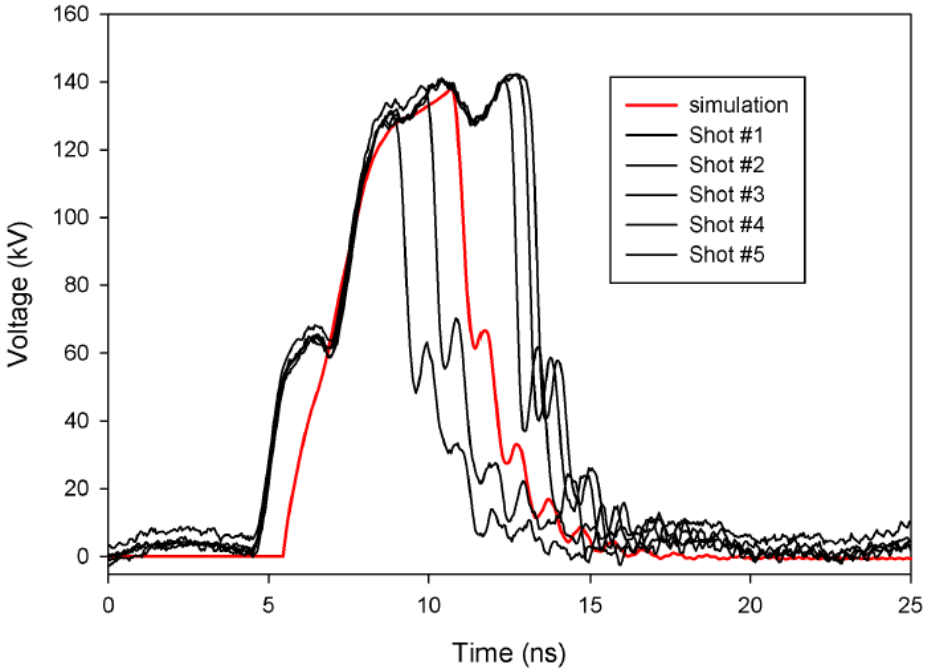

Figure 15 - Simulation vs. experimental data – spark gap pressure of 1800 psig and a charge voltage of 37.5 kV. The red line is the simulated waveform. The black lines are representative experimental shots.

2.7 Experimental Validation 2 - Marx Generator

2.7.1 Experimental Data Source

As a test of the ability of the spark gap model to provide useful simulations of a common pulsed power system, it was incorporated into a model of a reconfigurable Marx generator. This is a small, air-insulated Marx that will be used for breakdown studies. It has been designed to be easily reconfigurable to provide pulses over a wide range of voltage and energy. Figure 16 shows the Marx as configured when the data to be presented was obtained.

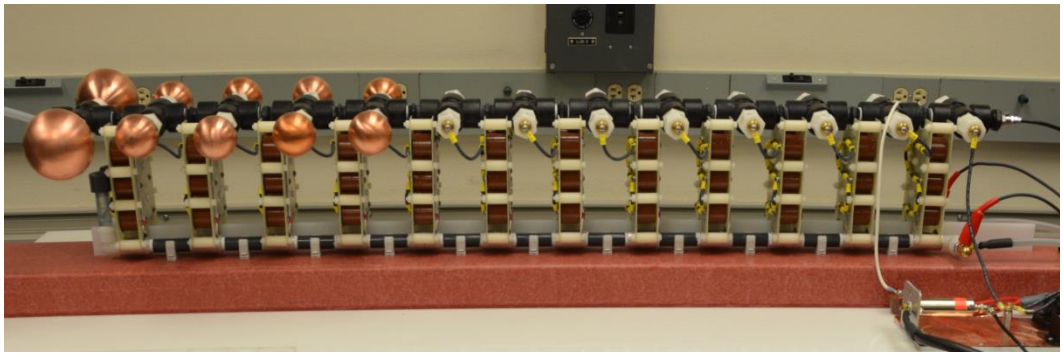

Figure 16 - Reconfigurable Marx generator. The vertical plates are stages – each containing six TDK ceramic capacitors. The grey tubes at the bottom are the charging resistor strings. The spark gaps are enclosed in the black fittings at the top of the stages. The copper spheres on the last five stages are for corona suppression.

2.7.1.1 Experimental Setup

The reconfigurable Marx generator consists of up to twelve stages of six TDK ceramic capacitors. The stages are charged through a string of aqueous solution resistors fabricated from rigid PVC and aluminum fittings. The resistive solution is a 1 g/L solution of sodium thiosulfate in deionized water – giving a resistance of 5 kΩ per section. The resistor assemblies also serve to provide support for the stage plates, which rest on the aluminum fittings. The Marx spark gaps are contained in an assembly constructed from thirteen polypropylene tee fittings. The spark gap electrodes are brass rods with hemispherical ends. The gap between stages one and two is a triggered gap with a 1.5 mm pin at the mid-plane between the main electrodes. The spark gap assembly is arranged such that the gaps are all on the same line of sight, with an unobstructed path for the UV light from one gap to illuminate the next.

The output of the Marx was connected to electrodes placed on top of a large container of dry silica sand. The electrodes are 25 cm by 2.5 cm strips of stainless steel embedded in the bottom of dielectric blocks. This setup is part of a series of breakdown tests that are to be conducted in the sand. For the purposes of this shot, the sand/electrode system can be modeled as a very high value resistance in parallel with a small capacitance. The current waveform of the output of the Marx was recorded to

verify that there was no breakdown through the sand. Figure 17 shows the electrodes and the sand as used in the experiment.

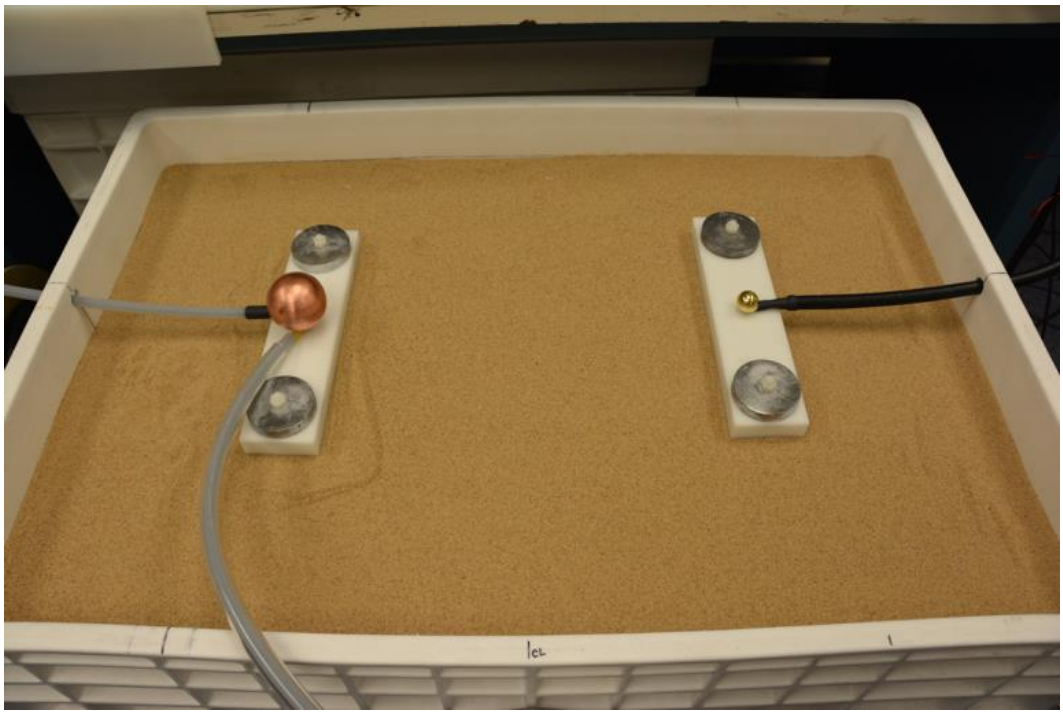

Figure 17 - Electrodes and sand container used in experimental shot. The electrode strips are embedded in the bottom of the white dielectric blocks. Electrical connection is via studs that pass through the blocks. The electrode spacing is 50 cm center-to-center.

The output voltage was measured using a North Star VD-200 high voltage probe for the open circuit shot presented here. Prior to conducting the open circuit shot, a short-circuit ring-down test was performed to estimate the total inductance of the Marx and connecting leads. The result was approximately 7 µH.

2.7.1.2 Experimental Parameters

For the experimental shots presented herein, the reconfigurable Marx generator was setup with twelve stages, each containing six TDK ceramic capacitors of 560 pF each. The charge voltage was set at 16.6 kV, giving a theoretical erected output voltage of approximately 200 kV. The spark gap distance is set at approximately 5 mm for the non-triggered gaps except for the first and last gaps, which are set to approximately 2.5 mm.

The triggered gap is set to approximately 6.5 mm to account for the presence of the trigger electrode. The spark gap pressure was set at 900 Torr.

2.7.2 Simulation Model

The simulation model of the reconfigurable Marx generator was created in order to test the spark gap model as well as to permit analysis of the results of the experiments for which the Marx was constructed.

2.7.2.1 Model of Experimental Apparatus

A model of the reconfigurable Marx was created in LTspice. The simulation circuit is quite complex due to the number of components in the Marx and the desire to model as many of the circuit parasitics as possible. Thus, it is impossible to show the model in its entirety. However, a good understanding of the circuit can be obtained from examining the circuit diagram of a single stage. Figure 18 shows the circuit schematic of a single stage from the LTspice model.

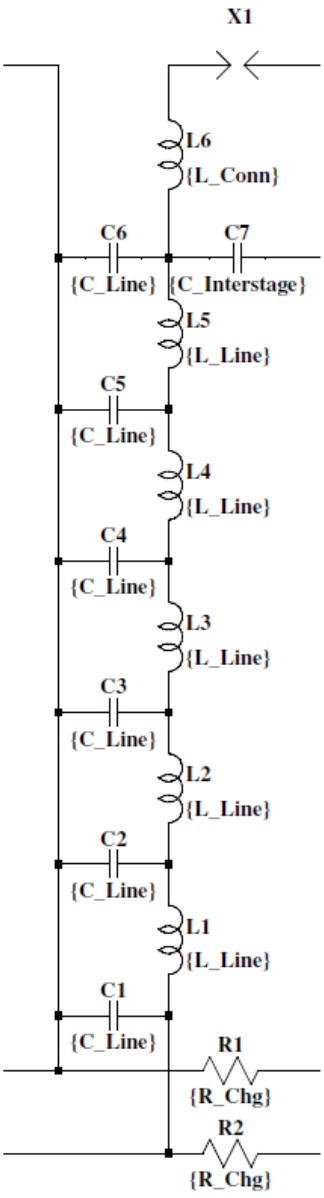

Figure 18 - LTspice schematic for one stage of the reconfigurable Marx generator. This circuit is repeated 12 times to make up the complete Marx simulation circuit.

In the single stage schematic shown, capacitors C1 - C6 represent the physical TDK capacitors that are part of each Marx stage. They are assigned a value via the parameter C_Line. The capacitor C7 represents the small parasitic capacitance that exists between stages and is defined by the parameter C_Interstage. The inductors L1 - L5 represent the inductance and resistance of the leads that connect the capacitors on the actual stage plates. These inductors have an inductance value defined by the parameter L_Line and a

series resistance defined by the parameter R_Ind. Inductor L6 models the inductance and resistance of the wires that connect the stage plate to the spark gap electrodes. Its inductance is defined by the parameter L_Conn. The component X1 is the spark gap model. Resistors R1 and R2 model the charging resistors with a value defined by parameter R_Chg.

The circuit described above is repeated 12 times in the simulation schematic for the complete Marx generator. To model the triggered spark gap on the first stage, two instances of the spark gap model are connected in series, with a connection to the simulation model of the trigger generator circuit connected to the common point. The gap of each of the two instances is then set to one-half the total gap distance less the thickness of the trigger electrode. This has proven to provide a relatively accurate simulation of the behavior of a mid-plane triggered gap using this model.

The output of the simulated Marx circuit was connected to a simple circuit to represent the impedance of the connecting leads, the sand, and the high voltage probe used in the experimental shot. This circuit is shown in Figure 19.

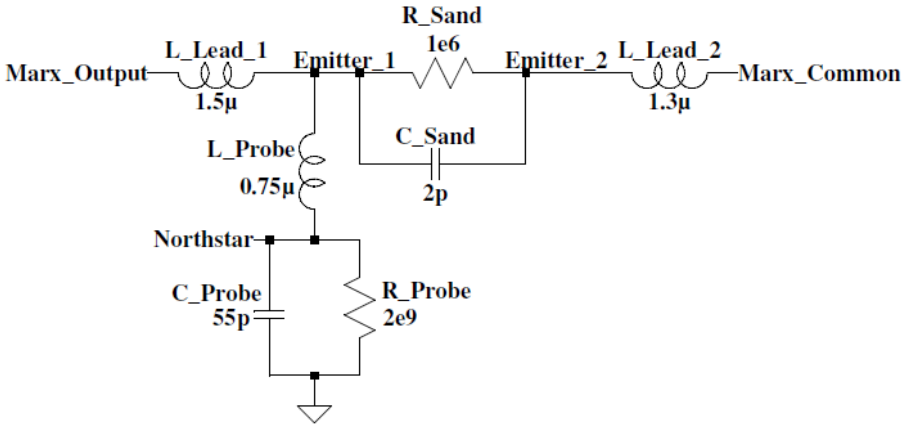

Figure 19 - LTspice schematic for the impedance of the components connected to the output of the Marx generator.

The nodes Emitter_1 and Emitter_2 represent the electrodes in contact with the sand. R_Sand and C_Sand model the resistance and capacitance between the electrodes due to the sand. The value of R_Sand has been chosen as 1 MΩ as an arbitrary high value. The value of C_Sand is based on the ringing frequency observed in the measured

current through the sand. The inductors L_Lead_1 and L_Lead_2 model the inductance and resistance of the lead wires between the Marx and the electrodes. Their values are based on the calculated inductance from the geometry of the leads. The components L_Probe, R_Probe, and C_Probe represent the impedance of the North Star VD-200 probe used in the experiment and the lead that connected it to the high voltage electrode. The resistance is as given in the North Star manual. The inductance was calculated from the lead geometry. The capacitance was calculated from the ringing frequency of the open circuit shot in conjunction with the inductance that had been previously calculated from the short circuit test. The value that produced the correct ringing frequency is approximately two times the stated capacitance of the probe. However, in this setup, the probe is located very close to the sand box thus making an increase in capacitance due to proximity effects likely.

2.7.2.2 Simulation Model Configuration and Parameters

The spark gap model used in the reconfigurable Marx simulations was configured as described in section 2.6.2.2 above with the exception of the expression used for the static breakdown voltage, which was the expression given in (2). The parameters used for the simulation are given in Table 1.

Table 1
Marx Simulation Circuit Parameters

Parameter	Description	Value
C_Line	Capacitance of a single capacitor in a stage	560 pF
C_Interstage	Stray inter-stage capacitance	2 pF
L_Line	Inductance of capacitor connections	25 nH
R_Ind	Resistance of capacitor connections	1 mΩ
L_Conn	Inductance of stage to gap connections	300 nH
R_Chg	Resistance of each charge resistor section	5 kΩ
V_Chg	Charge voltage	16.6 kV
Gap	Spark gap distance	5 mm
Press	Spark gap pressure	900 Torr

2.7.2.3 SPICE Tolerances and Parameters

The SPICE tolerances in LTspice were left at the default values with the exception of the value of TRTOL which was set to 0.1. The solver was set to *Alternate* as this has proven to provide more stable simulations using the spark gap model with only a slight increase in simulation time.

2.7.3 Result Comparison

The simulation was run and compared to the data collected from the test shots performed with the reconfigurable Marx. The results are shown in Figure 20 and Figure 21. In both figures, the red trace is the simulation data and the black trace is the experimental data. It can be seen that the simulation data follows the shape of the experimental data very well. It can be seen that the simulated voltage is a constant factor higher than the experimental data. There could be several reasons for this discrepancy, either in the experiment or in the simulation – or a combination of factors from both. Experimental error may be the result of measurement system errors. The probe has a stated accuracy of 3%, but this has not been confirmed for the particular probe used in this experiment. The charge voltage measurement has been calibrated to within 1% of the actual value, but due to the nature of the Marx circuit, errors in that measurement are multiplied by the number of stages. It is also possible that the simulation underestimates the losses present in the actual circuit. The primary source of this loss is the voltage drop across the resistance of the spark gaps.

Whatever the source of error, it results in only a 10% difference in voltage between the simulation and the experimental data. Figure 21 includes a plot with the experimental data scaled by a factor of 1.1. The excellent agreement of the simulation pulse shape with the scaled experimental data is encouraging. A further encouraging result is the fact that this simulation circuit was created prior to the construction of the actual hardware and served well in building the final system. While the actual values of some of the parasitic inductances and capacitances were determined from experiments,

the initial simulations before the experiments produced results that were very similar to the final performance of the Marx.

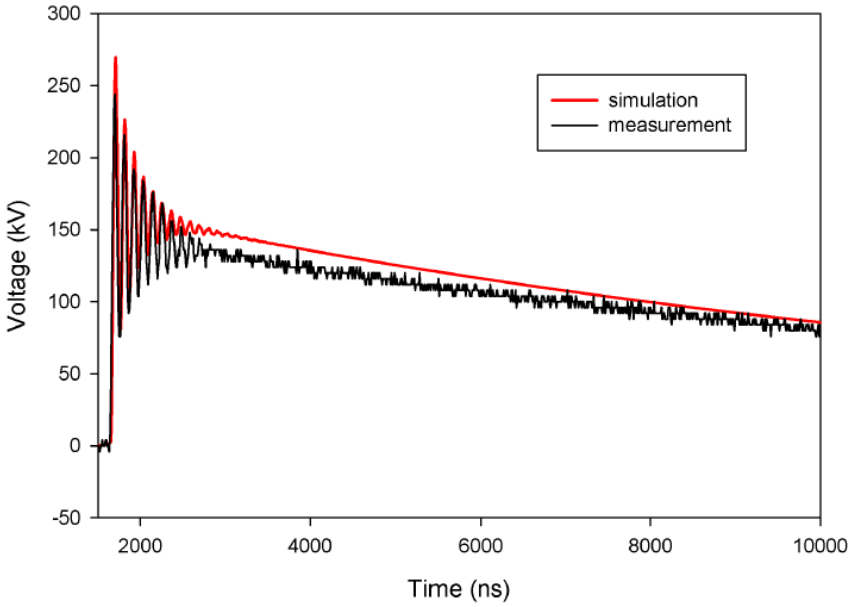

Figure 20 - Simulation vs. experimental data – reconfigurable Marx open circuit shot.

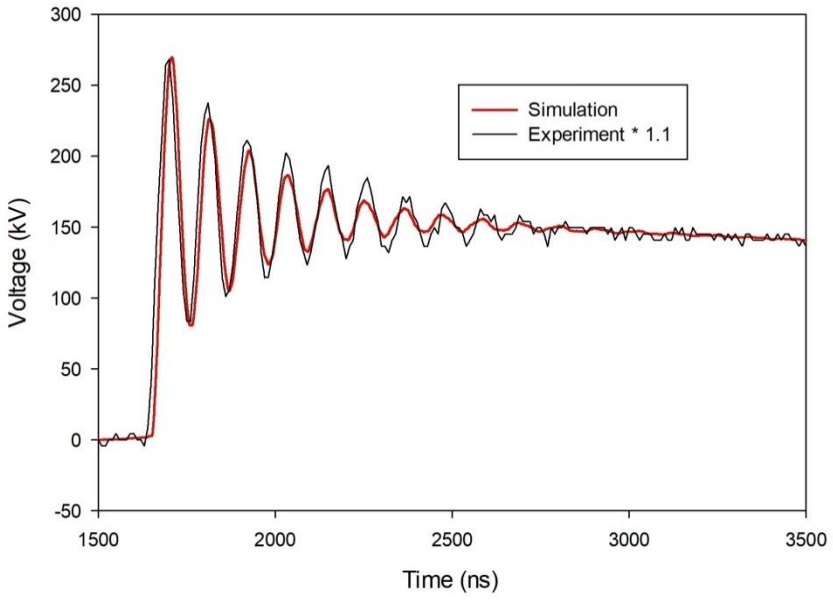

Figure 21 - Simulation vs. scaled experimental data – reconfigurable Marx open circuit shot. Close-up view of rising edge and ringing due to high voltage probe capacitance and Marx inductance. Note the excellent agreement in waveform shape – including the distortions of the ringing that appear as the oscillations decay.

It is also informative to compare the results of this model with the simulation of an identical Marx circuit with the spark gaps modeled as ideal switches that are forced to close at a particular time. Using ideal switches presents an initial challenge of selecting the resistance of the switches in the conducting state. As discussed in earlier sections, the actual conditions in the circuit during switch conduction have a very strong influence on spark channel resistance. However, an ideal switch in SPICE can only have one value of on resistance. The value chosen has a significant impact on the output of the Marx as shown in Figure 22. This significant difference exists even though the Marx is firing into an open circuit in this case – and as such it would be expected that the switch impedance would have minimal effect. Note that no prior knowledge of the spark resistance was necessary for the present model to achieve the agreement shown in Figure 21.

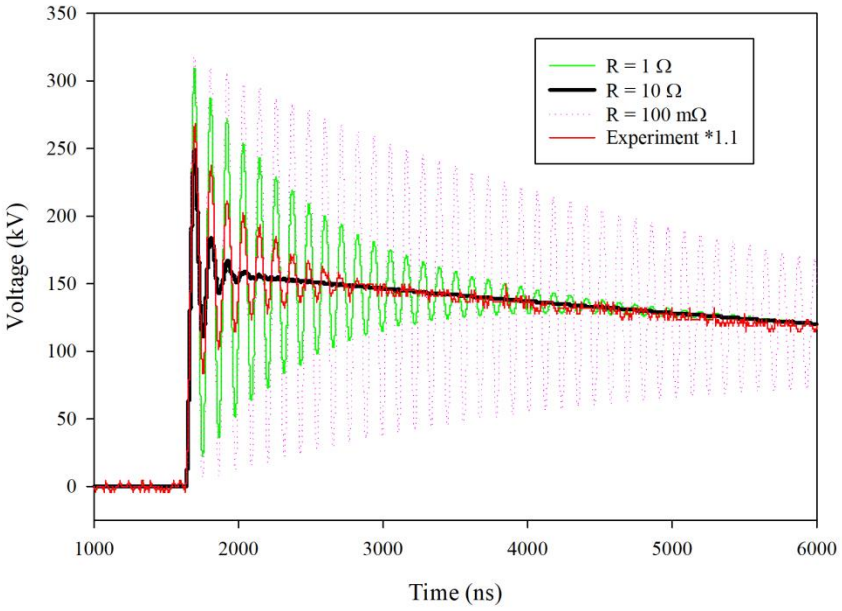

Figure 22 - Simulation of the Marx circuit with ideal switches that close simultaneously plotted for different values of switch resistance along with the scaled experimental data. Note that the Q of the ringing is strongly affected by the choice of resistance value – limiting the predictive capability of this method of simulation.

An additional advantage of using the present model to simulate the gaps in a Marx generator is the ability to uncover unexpected behaviors in the erection process of the Marx. This can be accomplished by monitoring the individual gaps to see when they break down during the erection process. In the case of the simulation of this Marx, it was shown that, after the triggered gap is fired, the last gap was the next to fire, followed by the first gap, and then the remaining intermediate gaps. This non-sequential firing of the gaps is not normally expected, but has been shown to be a consequence of the low stage-to-ground stray capacitance of this Marx generator as described in Chapter 3.

CHAPTER 3

ERECTION DYNAMICS OF COMPACT MARX GENERATORS[2]

3.1 Introduction

Compact Marx generators have become popular as sources of high voltage pulses for driving high power electromagnetic devices for numerous applications. They can provide a compact, low cost solution to achieving the voltage and current required to generate the relativistic electron beams necessary to drive high power microwave devices [37] [38] [39]. In addition, they can be designed to provide pulse rise times and voltages sufficient to generate ultra-wideband high-power radio-frequency pulses [40].

The seeming simplicity of the basic Marx circuit can lead to the misperception that a compact Marx will function in a predictable manner. However, those who attempt to build such devices almost invariably find that they do not function as intended [41] [42]. Furthermore, the behavior of these systems can seem counter-intuitive and mysterious even to those well-versed in the design of high voltage systems.

Often, the researcher can produce acceptable results from a particular Marx design through trial and error. However, because the load is usually the component of interest to the researcher, a deeper understanding of why the Marx didn't work in the first place is not pursued and whatever adjustments were used to get the system working may be dismissed as idiosyncrasies of that device. This leads to a situation where fundamental design practices must be re-learned for each new device – a situation that increases design risk and impedes the adoption of pulsed power technology.

The goal of this chapter is to investigate the operation of non-ideal Marx generator circuits to determine the sources of the problems that often plague the operation of compact devices and to detail some solutions that can be incorporated into the design of compact Marx generators. The chapter begins with a computational analysis of

[2] Sections 3.1 and 3.2 © 2019 IEEE. Reprinted, with permission, from: J. C. Pouncey, J. M. Lehr and D. V. Giri, "Erection of compact Marx generators," IEEE Trans. Plasma Sci., vol. 47, no. 6, pp. 2902-2909, 2019. DOI: 10.1109/TPS.2019.2915034

fundamental Marx operation, taking into account the various stray capacitances that exist in a typical Marx generator. This analysis shows that the conventional view of Marx operation is incomplete and explains the often noted, non-sequential firing of the final spark gap. It is shown that proper consideration of the stray capacitances is necessary for the development of Marx generators to produce reliable triggered operation. Because compact, low energy Marx generators often exhibit very large values of stray capacitance, this is even more true for this class of pulsed power devices. This analysis is followed by a survey of common compact Marx generator implementations with a focus on the typical design choices that can exacerbate the issues uncovered by the analysis.

3.1.1 Basic Description of a Marx Generator

The Marx generator is one of the fundamental circuits used for energy storage and high voltage pulse generation in the field of pulsed power. While Marx generators may be constructed using various switching technologies [43], the most common is still the gas switch or spark gap. The basic operation of a Marx generator is dependent on the proper closing of all of the spark gap switches over a time period that is on the order of tens of nanoseconds to a few microseconds in a process known as erection of the Marx. One or more of the spark gap switches will be triggered by some external means and the remaining switches are closed by the overvoltage (defined as the applied voltage in excess of the static breakdown voltage of each switch) created by the closing of the previous switches. In an ideal case, this would result in sequential closing of the switches and the Marx would perform as expected.

Figure 23 shows the basic circuit of a four-stage Marx generator. The Marx capacitors, labeled C_{m1} through $C_{m4,}$ are the energy storage elements of the circuit and are assumed to have the same capacitance, thus $C_M = C_{m1} = C_{m2} = C_{m3} = C_{m4}$. The Marx resistors R_{m1} through R_{m6} provide a path for the charging current while providing isolation during the erection process and are assumed to have the same resistance, thus $R_M = R_{m1} = R_{m2} = R_{m3} \ldots = R_{m6}$. The charging resistor R_{ch} provides isolation of the power supply during erection and is often the same magnitude as one of the Marx resistors.

The spark gap switches are labeled S_1 through S_4 and are assumed to be identical except for the command triggering capability of switch S_1. Finally, the load resistance is denoted R_L. Note that any of the resistances in this circuit may be replaced with more complex impedances, but the initial analysis will address the purely resistive case. This analysis will make use of the node labels A through H shown in Figure 23 when referring to circuit voltages. The charge voltage V_0 is chosen to be some fraction of the breakdown voltage of the Marx switches, V_{SB}, so that the switches do not break down before the command trigger is initiated. This fraction is generally between 70 and 90 percent.

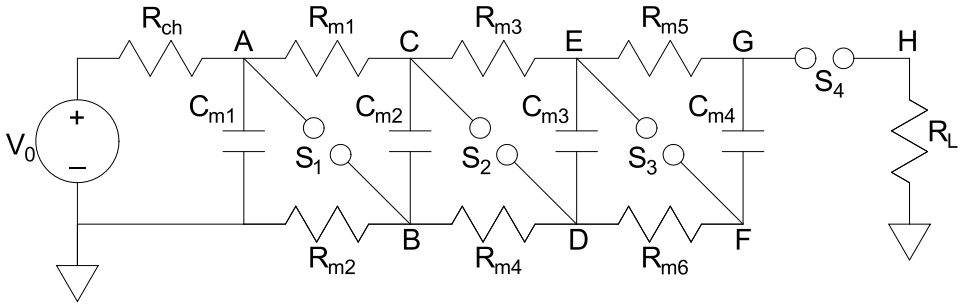

Figure 23 - Four-stage basic Marx generator circuit.

3.1.2 Prevailing Explanation of Marx Operation

The conventional description of the erection process for this basic Marx circuit is as follows. At the end of the charging process, each of the points A, C, E, and G are at potential V_0 and the points B, D, F, and H are at ground potential. Switch S_1 is closed by some external triggering means to initiate the erection process. This connects points A and B. Capacitor C_{m2} holds the potential difference between points B and C at V_0 while R_{m4} provides isolation between points B and D. This leads to a voltage of $2V_0$ appearing across switch S_2 which decays with a time constant:

$$\tau_M = C_M R_M \tag{8}$$

During this time, S_2 is overvolted by an amount:

$$V_{over} = 2V_0 - V_{SB} \tag{9}$$

For this basic Marx circuit to erect properly, V_{SB} can be no more than $2V_0$ and the time τ_m must be long enough to guarantee the closing of switch S_2. The time factor is important because of the statistical and formative delays associated with the gas breakdown process [44]. Once switch S_2 closes, it applies the potential at C (approximately $2V_0$) to point D and the process is supposed to repeat for each subsequent switch until all of the switches have closed.

3.1.3 Marx Operation Without Stray Capacitance

In the case of a Marx with no stray capacitance, the sequence described in the previous section cannot occur. The problem lies in the assumption that point D stays at ground potential when S_1 closes, yet there is no reason it must do so. Without anything to hold the potential at point D to ground, the closing of S_1 increases the potential of the entire network between points B and G by a factor of V_0. Thus, the full $2V_0$ appears across switch S_4 since point H is held at ground potential by the load. All of the remaining open switches remain charged to V_0, which, by definition is less than the breakdown voltage of the switches. Thus, S_4 is the only switch which can close next. Once that occurs, the load and the Marx resistors form a voltage divider that divides the total $2V_0$ overvoltage across the remaining switches and the load according to their relative values. After the first and last switches have closed, at any point in time when 'n' switches have closed in an 'N' stage Marx with no stray capacitance, the normalized voltage on each switch will be:

$$\frac{V_S}{V_0} \approx \left[1 + \frac{n}{N-n}\left(1 - \frac{R_L}{R_L + 0.5(N-n)R_M}\right)\right] \times \exp\left(-\frac{t}{R_M C_M}\right) \tag{10}$$

If this voltage is greater than the breakdown voltage of these switches, and if it does not decay away faster than their delay times, then these switches can now close. As each remaining switch closes, the voltage that was across it gets divided evenly among the remaining open switches and the load, thus increasing their overvoltage and introducing a relatively slow rising stepped pre-pulse at the load. This first gap – last gap – middle gaps sequence has been observed in a 4-stage Marx constructed by the author and

outfitted with optical diagnostics on each of the spark gaps. The validity of (9) can be verified through SPICE simulation as shown in Figure 24.

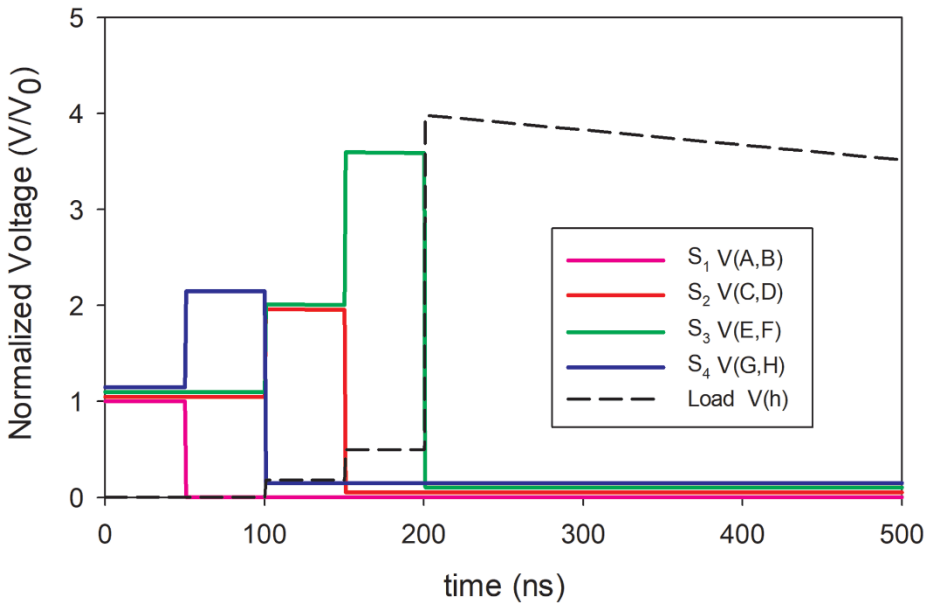

Figure 24 - Plots of the circuit simulation of a zero-stray capacitance 4-stage Marx with $V_0 = 1$, $C_M = 10$ nF, $R_M = 10$ kΩ, and $R_L = 1$ kΩ. Switch S_1 closes at time t = 50 ns, then S_4 closes at 100 ns, followed by S_2 at 150 ns, and S_3 at 200 ns.

3.1.4 Stray Capacitance

Very few Marx generators will operate as described in section 3.1.3, due to the numerous stray capacitances that impact the operation of the Marx. These stray capacitances can be either beneficial or detrimental to the erection process. Figure 25 shows the four types of stray capacitances that affect the operation of a Marx. They are the gap capacitance C_g, the stage-to-ground capacitance C_s, the inter-stage capacitance C_i, and the load capacitance C_L. The relative magnitude, and the resulting impact, of these stray capacitances is determined by the physical arrangement and materials of the Marx as well as its environment.

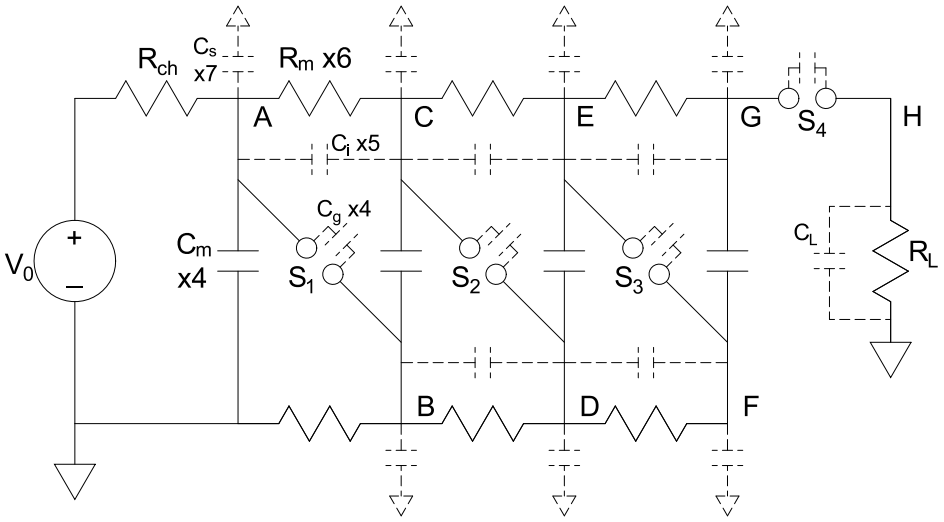

Figure 25 - Four-stage Marx circuit with stray capacitances C_g, C_s, C_i, and C_L shown in dashed lines. Note that there may be other strays and that some of these strays may be the parallel/series combination of the stray capacitance between various Marx structures – including interconnects. For simplicity, C_i is only shown between adjacent stages, but in practical devices, there is some coupling from every stage to every other stage.

3.2 Non-Ideal Marx Behavior

In compact Marx generators, the stray capacitances that affect the erection process are primarily the gap capacitance C_g, the inter-stage stray capacitance C_i, and the stage-to-ground stray capacitance C_s as shown in Figure 25. To examine how these capacitances affect the erection process, simulations have been performed to examine the effect of various combinations of Marx component and stray values on the voltages produced at the various points in the circuit after the closure of the first switch. Of particular interest is the magnitude and duration of the voltage across each of the open switches. Previous investigators have studied this problem [45] [46] but did so without the benefit of the fast and accurate circuit simulation software available today.

3.2.1 Effect of Gap Capacitance C_g

First consider the effect of the gap capacitance, C_g, on an otherwise ideal Marx generator circuit. For simplicity, consider the circuit for short time scales ($t << C_m R_m$) where the Marx resistor network (and the exponential term in (9)) can be neglected.

Figure 26 shows what remains of the prototypical four-stage Marx after making these simplifications.

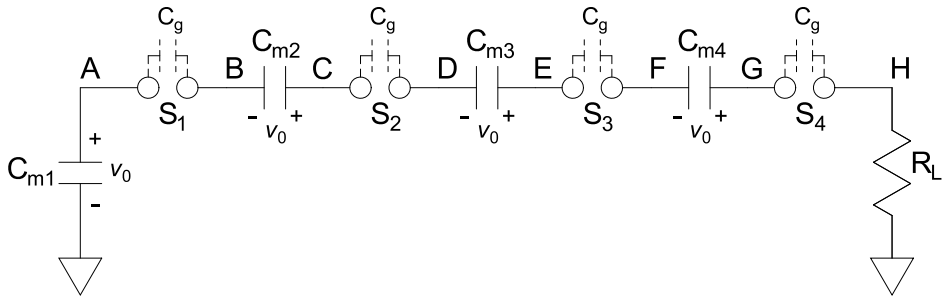

Figure 26 - Four-stage Marx equivalent circuit for short time scales with only the gap stray capacitance C_g being considered. Note that the node label lettering corresponds to the circuits in Figure 23 and Figure 25.

The operation of this circuit begins as it is shown, with the Marx capacitors charged to V_0 and the switches open. When switch S_1 is triggered into conduction at time $t = 0$, node B, which had been held at ground potential by the Marx resistor network, is pulled up to V_0 by capacitor C_{m1}. This voltage change is applied to the series string of the remaining Marx capacitors, the gap capacitances, and the load. This forms a capacitive voltage divider being charged through load resistance. Since any useful Marx must have $C_m >> C_g$, the gap capacitors dominate the voltage divider. The normalized voltage on each switch can be calculated as:

$$\frac{V_s}{V_0} \approx 1 + \frac{1}{N-1}\left(1 - exp\left(-\frac{t}{R_L\frac{C_g}{N-1}}\right)\right) \quad t \ll C_M R_M \tag{11}$$

while the normalized load voltage is:

$$\frac{V_L}{V_0} \approx exp\left(-\frac{t}{R_L\frac{C_g}{N-1}}\right) \quad t \ll C_M R_M \tag{12}$$

Thus, for this arrangement, the gaps are charged up above the charge voltage by a factor equal to the charge voltage divided by the number of open gaps. Also, there is a pulse of magnitude V_0 applied to the load which decays as the gaps charge up. This contrasts with the zero-stray case in which all of the overvoltage is dropped across the

final gap when the first switch closes. However, this state only exists temporarily because of the contribution of the Marx resistor network. On a slightly longer time scale, on the order of $t = R_m C_g$, the Marx resistor network (not shown in Figure 26) provides a current path that permits the gap capacitances of the intermediate stage switches to transfer charge to the final gap, which, as in the zero-stray case, is still the only switch with a direct path to ground through the load. Thus, the final gap, S_4, charges up to a voltage given by:

$$\frac{V_{S4}}{V_0} \approx 2 - exp\left(-\frac{t}{R_M C_g}\right) \quad t \sim C_g R_M \tag{13}$$

At the same time, the voltage on the intermediate gaps decays back to V_0 at the rate given by the exponential term in (13). Thus, the end state of switch voltages after the closing of the first switch is the same as the zero-stray case. However, due to the relatively large value of $R_m C_g$, the switches spend significant time between the state described by (11) and that described by (13). The voltages on the four gaps and the load as simulated in a SPICE program are shown in Figure 27.

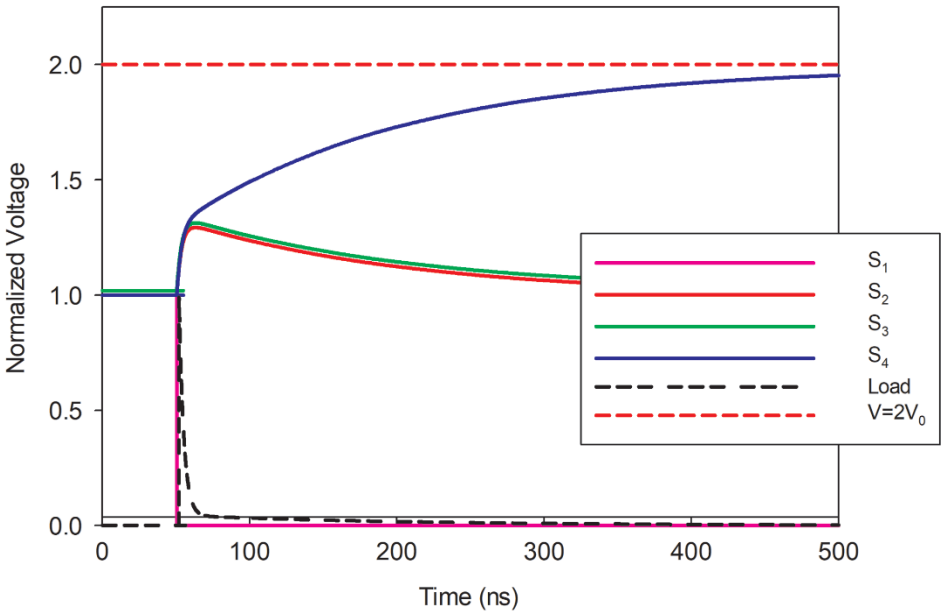

Figure 27 - Plots of the circuit simulation of the example Marx with V_0 = 1, C_m = 10 nF, C_g = 10 pF, R_m = 10 kΩ, and R_L = 1 kΩ. Switch S_1 closes at time t = 50 ns.

If the final gap closes after the first gap due to the rising voltage described by (12), then the voltage on the remaining open switches will charge with a time constant of approximately $0.5C_gR_L$ to the voltage described by (9) and this will continue to be the case after the closing of additional switches. If one of the intermediate switches closes during the brief overvoltage described by (10) before the final switch, then its voltage gets discharged into the series string of the remaining open switches and the load, in the same manner as when the first switch closed. This can be described by (10) with the denominator of the second term replaced with N-2.

An interesting consequence of these results is that C_g, while generally considered as a negative on the operation of a Marx, provides the possibility of sequential operation of the Marx since some overvoltage is imposed on S_2 immediately after the closing of S_1, unlike the case described for the Marx without gap capacitance. For this to happen, the voltage described by (10) must create an overvoltage on S_2. The N-1 term in the denominator of (10) makes this difficult for devices with many stages.

3.2.2 Effect of Stage-to-Ground Capacitance C_s

The stage-to-ground capacitance, C_s, is the second type of stray capacitance that has significant effects on the operation of the Marx circuit. Figure 28 shows the short-time-scale schematic of the prototypical four-stage Marx with both C_g and C_s included. Note that while there is certainly some stray capacitance from node A to ground, it is in parallel with C_{m1}, which is much larger. Also, the stray capacitance from node H to ground is effectively a load capacitance since it is in parallel with R_L.

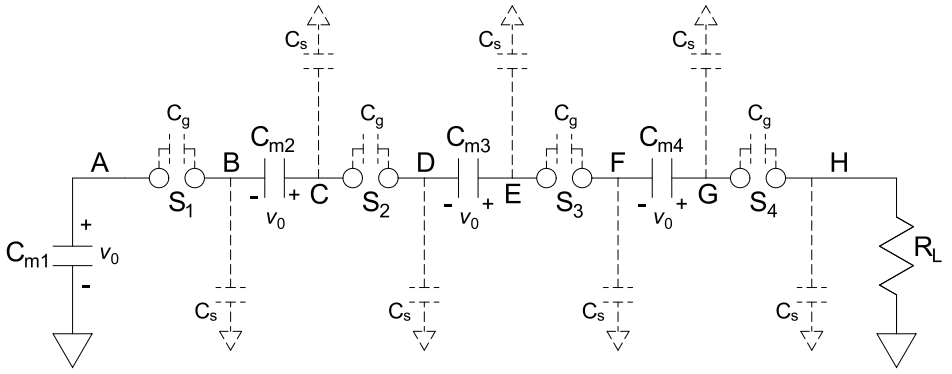

Figure 28 - Four-stage Marx equivalent circuit for short time scales with the gap stray capacitance C_g and the stage-to-ground stray capacitance C_s shown in dashed lines.

The primary effect of C_s is that it lowers the transient impedance from each node in the circuit to ground. This can be very beneficial to the erection process because it provides a means for individual switches to charge without dividing the voltage between the remaining open switches. It also provides a charging path for the switches that is independent of the load. For the theoretical case with C_s as the only stray, after S_1 closes, voltage V_0 is applied to node B in our prototypical Marx and C_{m1} must charge the C_s at B up to V_0. If $C_{m1} >> C_s$ and the impedance of the closed S_1 is low, this happens very fast and with little loss. The increase in voltage is applied across the series string of C_{m2} and the C_s at node C. Since $C_{m2} >> C_s$ and C_{m2} was already charged to V_0, the voltage at C rises instantly to approximately $2V_0$. Up to this point, the erection process is the same as that described for a Marx without stray capacitance. However, in this case node D is held down to ground potential by the stray capacitance to ground. Thus, a voltage of

$2V_0$ appears across S_2. The capacitance from node D to ground can only be charged by either S_2 closing (the desired outcome) or through the Marx resistor network (not shown in Figure 28). If S_2 does not close, then the charge stored in the capacitance to ground from node C will discharge through the Marx resistor network, into the remaining capacitance to ground until it finally ends up, as in all the previous cases, producing a voltage of $2V_0$ across the final switch S_4. The voltage across S_2 after S_1 closes is thus:

$$\frac{V_{S2}}{V_0} \approx 1 + exp\left(-\frac{t}{R_M C_s}\right) \quad t \sim C_s R_M \tag{14}$$

A simulation of this process is shown in Figure 29. Note that, as the voltage on S_2 decreases, the voltage on S_3 briefly increases and then decays, while the voltage on S_4 increases monotonically. This is due to the voltage dividing effects of the Marx resistor network and the distribution of C_s along the circuit.

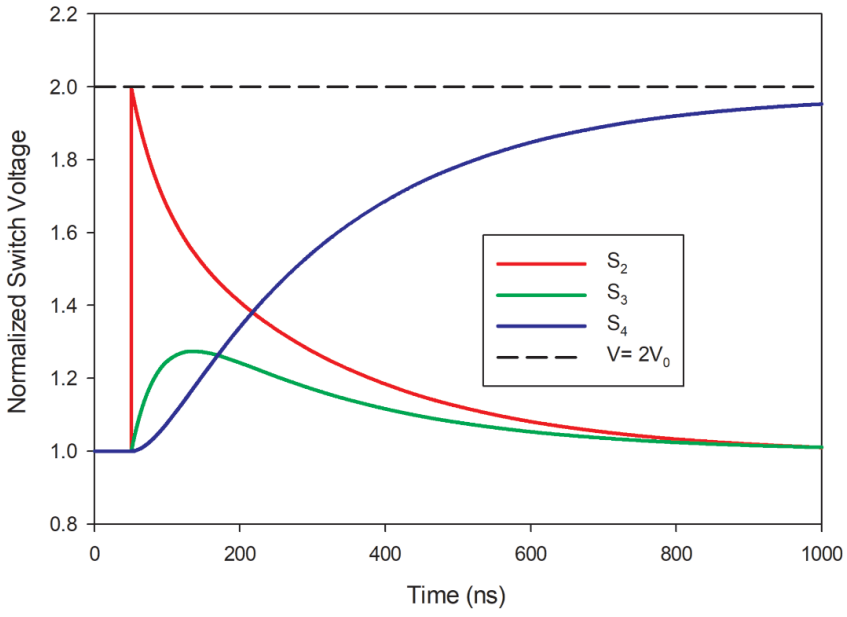

Figure 29 - Plots of the circuit simulation of the example Marx with V_0 = 1, C_M = 10 nF, C_s = 10 pF, R_M = 10 kΩ, and R_L = 1 kΩ. Switch S_1 closes at time t = 50 ns.

If switch S_2 does not close during the transient overvoltage described by (14), then it is most likely that switch S_4 will close as its voltage slowly rises. In this case a pulse of

magnitude equal to the voltage that was across S_4 will be applied to the load. This voltage decays away as the C_s capacitance discharges through the load and the circuit assumes the conditions described by (10). Since node F is closer to the load and discharges faster than node E, the voltage across S_3 increases above that given by (10) briefly during this time.

Since the scenario described in the previous paragraph is slow and introduces a pre-pulse at the load, it is not the desirable operating mode. If switch S_2 does close during the voltage transient described by (14) at time T_1, then the voltage on switch S_3 is increased to approximately $3V_0$ by the same process that occurred at S_2 when S_1 closed. This much larger voltage will most likely lead to S_3 closing rapidly, and thus applying $4V_0$ across S_4. This process is shown in a simplified simulation as Figure 30. The sequential operation of the gaps of a Marx driven by ever-increasing voltages due to intentional capacitance to ground has been termed wave-erection [46] [47] and is usually a desirable operating mode for a compact Marx generator because of its predictability and speed.

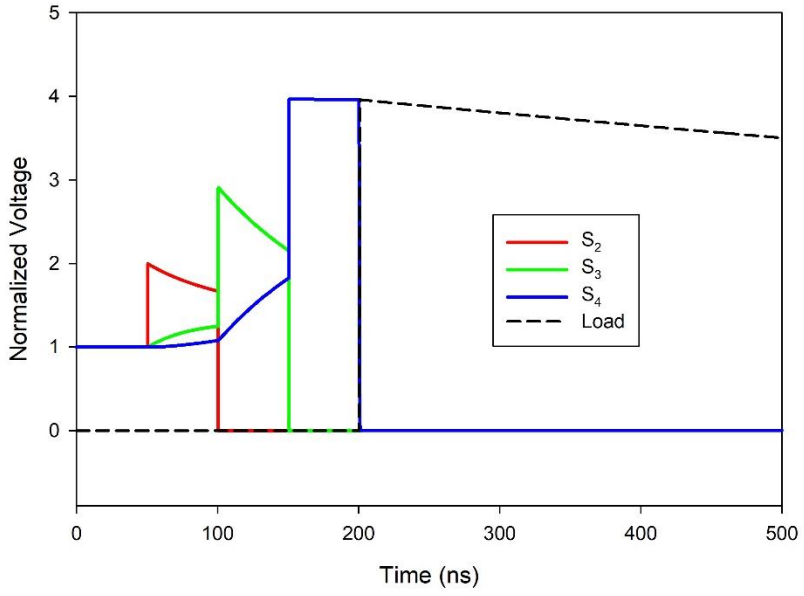

Figure 30 - Plots of the circuit simulation showing how the sequential operation of the switches can proceed in a Marx with only C_s.

The previous analysis assumed that C_s was finite while C_g was zero. A Marx like this is not realizable in practice. When both C_s and C_g are greater than zero, the process described above is changed slightly because the C_g of S_2 provides a path from node C to charge the C_s at node D. This forms a capacitive voltage divider, and thus the voltage across S_2 depends on the ratio of C_s/C_g. Plots of the voltage across S_2 for different ratios from 0.01 to 10 are provided in Figure 31.

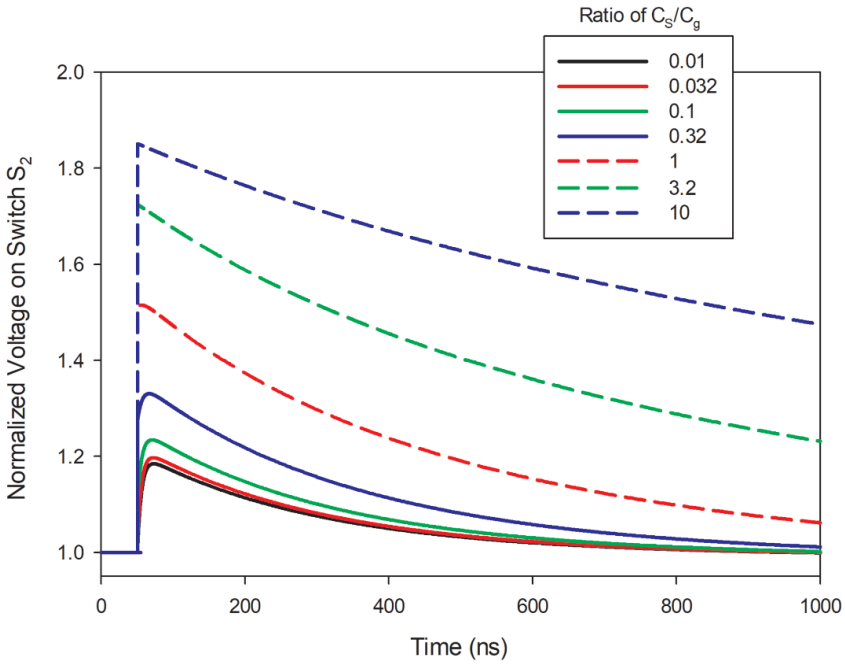

Figure 31 - Plots of the voltage on switch S_2 with S_1 closing at t = 50 ns for different values of C_s/C_g.

The presence of C_s has the additional effect of creating significant differences in the output waveform of a compact Marx generator. That effect is well described by Buchenauer [48] and is addressed in section 3.4.3.

3.2.3 Effect of Inter-Stage Capacitance C_i

The inter-stage capacitance may be the most complex of the stray capacitances present in a Marx generator because in a physical device, each of the stages has some capacitance to every other stage. Furthermore, since each stage consists of at least one Marx capacitor and one switch, there are at least three nodes per stage that may be

coupled to the nodes of any other stage via some capacitance. Fortunately, this situation can usually be simplified in practice by determining (or designing) the dominant C_i. In many cases, the largest magnitude C_i is effectively in parallel with C_g. For example, in the case of a Marx generator constructed using oil-filled capacitors arranged in a row, the capacitance between the bodies of the capacitors forms a large inter-stage capacitance as shown in Figure 32. Note that this is true even of plastic-case capacitors since the outermost layer of the windings are connected to one of the terminals and thus are an extension of that node that can capacitively couple to the adjacent capacitor. Figure 32 shows the most common case where the ground side of the capacitors are connected to the outer case (or outer winding).

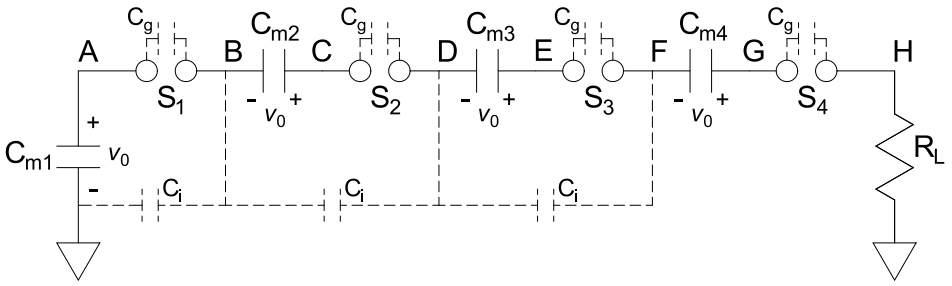

Figure 32 - Four-stage Marx equivalent circuit for short time scales with C_g and the inter-stage stray capacitance C_i shown in dashed lines. This configuration of inter-stage capacitance is typical of Marx generators using oil-filled capacitors.

In this configuration with C_i as the only non-zero stray capacitance, the effect on the voltages in the circuit when S_1 closes is the same as in the zero-stray case. The reason for this is that, when S_1 closes, the first inter-stage capacitance is charged from C_{m1} through the very low resistance of the closed switch. If $C_{m1} >> C_i$ this is accomplished quickly and with little loss of voltage. As node B is charged up to V_0, the remaining inter-stage capacitances are all connected between nodes that are increasing in voltage at the same time thus no current flows through these capacitances. This results in switch S_4 charging to $2V_0$ as before. If S_4 closes, then the result is slightly changed from the zero-stray case. The inter-stage capacitances of the intermediate stages will discharge

through C_{m4} and S_4 into the load, producing a fast-rising pre-pulse that decays according to:

$$\frac{V_L}{V_0} \approx 2\left(exp\left(-\frac{t}{R_L\frac{C_i}{N-2}}\right)\right) \quad t \sim C_i R_L \tag{15}$$

As this pulse decays, the switch voltages rise to the values given by (10) and the remaining switches either close or the voltage decays through the Marx resistor network.

In the more realistic case where both C_i and C_g are significant, increases in C_i relative to C_g tend to drive the switch voltage behavior back toward the zero-stray case by providing a low-impedance shunt path around the switch capacitances to charge the last gap. This results in the voltage across the intermediate switches being reduced from the voltage when there is only C_g. The amount of reduction is related to the ratio of C_i to C_g. Plots of the voltage across S_2 for different ratios from 0.01 to 10 are provided in Figure 33.

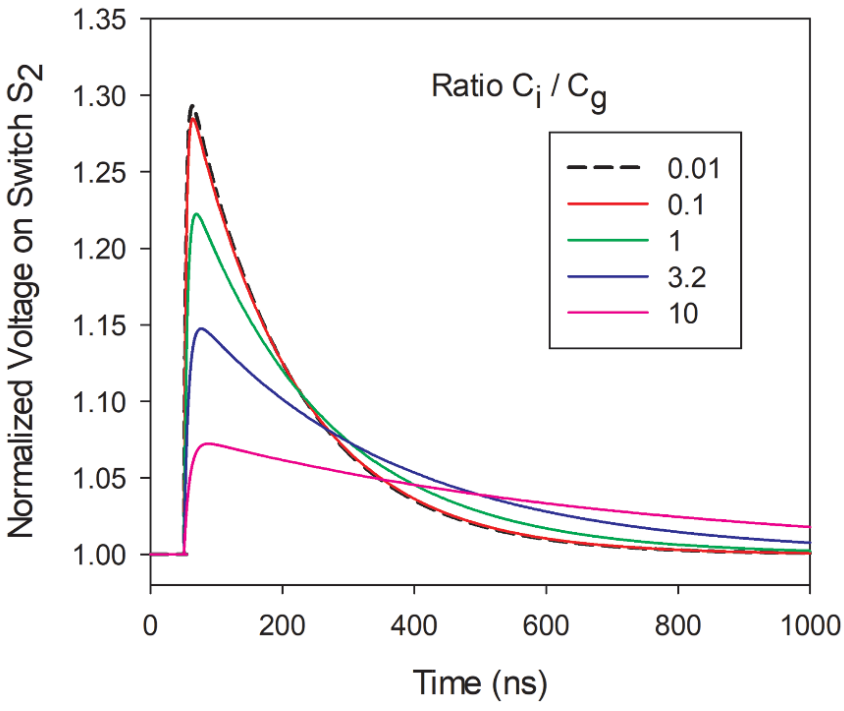

Figure 33 - Plots of the voltage on switch S_2 for different values of C_i/C_g

Another form of inter-stage capacitance is possible if the Marx is arranged such that the dominant coupling is between non-adjacent stages in the Marx circuit. This can take the form of every-other-stage coupling or more complex arrangements. Figure 34 shows the schematic of an every-other-stage coupling arrangement, which is labeled C_a to distinguish it from the previous C_i. The pattern may not be apparent for only four stages, but if the Marx continued, there would be another C_a capacitor from node D to node H, one from node F to node J, and so on. This arrangement can be achieved in practice by a zig-zag placement of oil-filled capacitors. It is more difficult with ceramic capacitor devices due to the need to swap the polarity at each stage. This configuration may also be created through the incorporation of physical coupling capacitors [49].

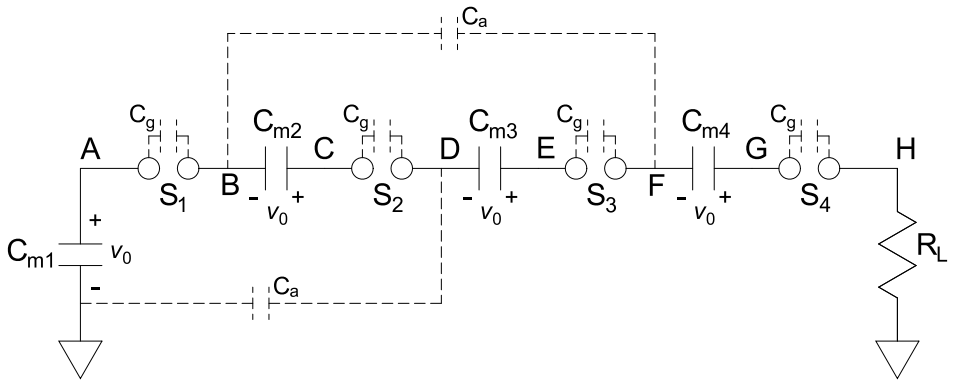

Figure 34 - Four-stage Marx equivalent circuit for short time scales with C_g and C_a shown in dashed lines.

Figure 35 shows a simulation of this circuit with $C_g = 0$. This configuration exhibits a unique behavior in that the voltage across switch S_2 immediately rises to $2V_0$, as does the voltage across switch S_4, while the voltage on switch S_3 drops to zero. The explanation of this behavior has two parts. First, the inter-stage capacitance between node D and ground serves to hold D at ground potential just as a C_s did. This allows the full $2V_0$ at node C to drop across S_2. The second effect is that the inter-stage capacitance between nodes B and F allows the rising voltage at B to increase the voltage at F to V_0, as F has no low-impedance path to ground. Since the voltage at node E is held at V_0 by C_{m3} and the C_a between node D and ground, the voltage at both ends of S_3 becomes

equal until the Marx resistor network is able to discharge C_a on the timescale of R_mC_a. Once again, if S_2 does not close, then the entire $2V_0$ ends up across the last switch, S_4, as the stray capacitances discharge through the Marx resistor network.

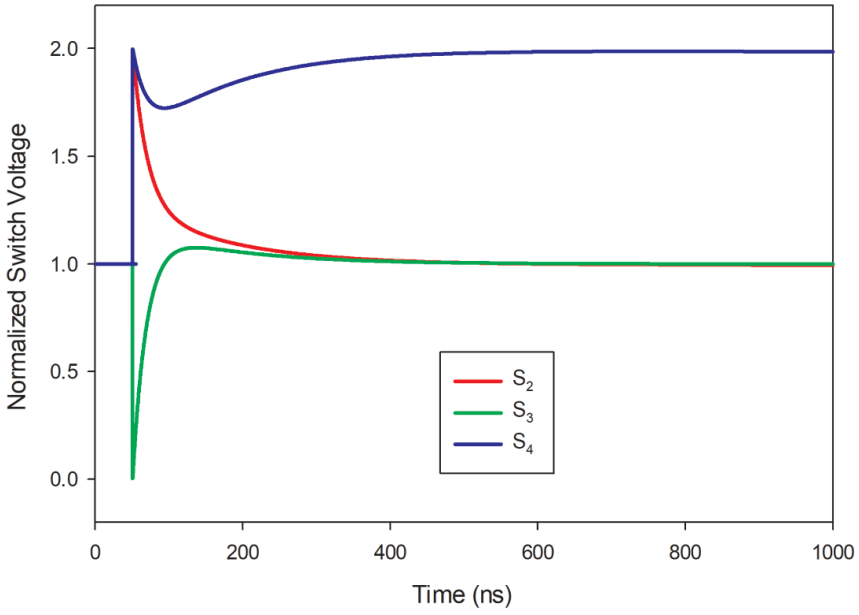

Figure 35 - Plots of the circuit simulation of the example Marx with V_0 = 1, C_M = 10 nF, C_s = 10 pF, R_M = 10 kΩ, and R_L = 1 kΩ. Switch S_1 closes at time t = 50 ns.

If S_2 does close during the initial transient, then voltage $2V_0$ will be applied to node D. The capacitance from D to ground will be quickly charged by C_{m1} and C_{m2} and the voltage at E will rise to $3V_0$ due to the voltage across C_{m3}. The C_a between nodes B and F maintains F at V_0, so that a voltage of $2V_0$ now appears across S_3. In a Marx with more stages, this process would repeat such that when an odd numbered switch closes, the voltage becomes greater than V_0 on the even numbered switches, and vice-versa. The voltage is highest – approximately $2V_0$ – on the switch closest to the one that just closed, and decreases at greater distances due to capacitive voltage dividing in the chain of inter-stage capacitances. Note that, while this scheme does provide for somewhat sequential operation of the Marx, it does not force it in the same way that large C_s does. The overvoltage also does not increase as more switches close, thus limiting the speed of erection. Once again, the previous analysis was based on a Marx with zero gap

capacitance. For a realistic case with gap capacitance greater than zero, the behavior is again dependent on the ratio of C_a to C_g, with larger ratios providing higher voltages due to the reduced effect of capacitive voltage dividing as shown in Figure 36.

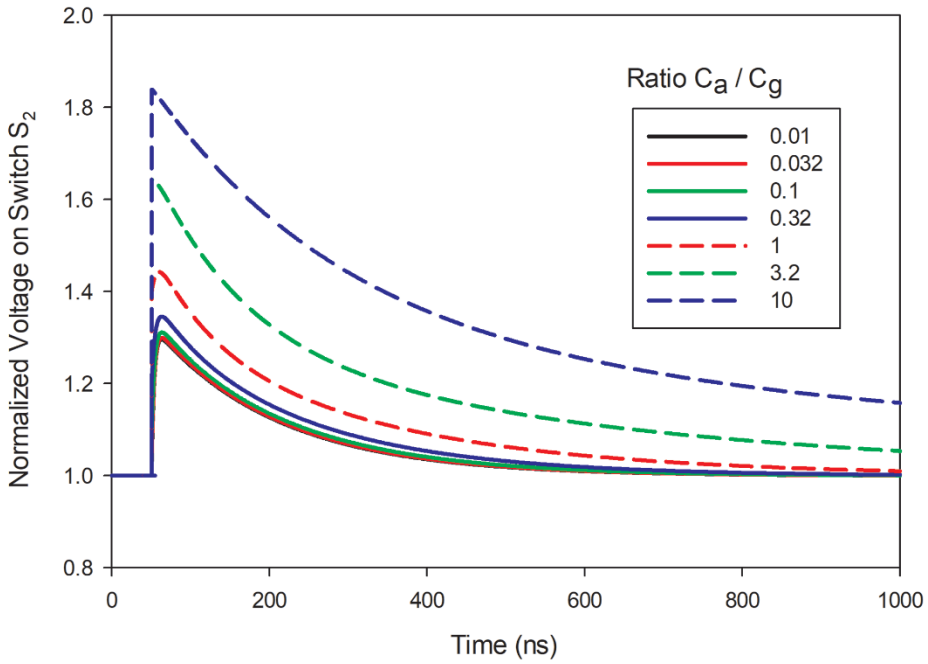

Figure 36 - Plots of the voltage on switch S_2 with S_1 closing at t = 50 ns for different values of C_a/C_g.

3.2.4 Effect of Capacitive Loads

Very few loads used for compact Marx generators are purely resistive. Many types of loads – including electrically short transmission lines, high power microwave tubes (before the start of cathode emission), and peaking capacitors – present a capacitive load to the output of the Marx. As the previous analysis has shown, the load has a significant effect on the voltages across the open switches during the erection process. A capacitive load presents a low impedance transient path to ground that can speed up the charging of the gap capacitances. For example, in equations (11) and (12) where R_L appears in the denominator of the exponential terms, a capacitive load would significantly reduce the effective value of R_L on the timescales of interest, thus speeding up the increase in V_S and the decay of the load pre-pulse. For this to be effective, the load capacitance must be much greater than the gap capacitance.

3.3 Common Compact Marx Configurations

A great deal of diversity is encountered in examining the design choices made by engineers and researchers that have developed compact Marx generators for various applications. However, in the majority of cases, the basic configuration can be traced to one of the following fundamental designs.

3.3.1 The Platts Marx

David Platts of Los Alamos National Laboratory was a pioneer in the design and use of compact, low energy Marx generators to drive loads directly [50]. The majority of current designs owe some of their design influences to the work of Platts. There are two defining features of the Platts Marx design. The first is the use of a close-fitting metallic outer housing – usually cylindrical – that serves as the current return path and pressure vessel for the device. The second is the use of pressurized gas as a shared insulating medium for the Marx and the switching medium for the gaps. These design features enable the construction of very compact low-impedance pulsed voltage sources. Additional common design features are the use of ceramic high voltage capacitors – particularly the ubiquitous TDK “doorknob” capacitors – and the alignment of the spark gaps with the intent of providing optical coupling for UV pre-ionization. The Platts Marx basic design has been used to generate open-circuit voltages from 100 kV to 1 MV and energies from 1 J to 1 kJ [51] [52] [53]. Figure 37 is a sectioned rendering of a typical construction used in a compact Platts Marx.

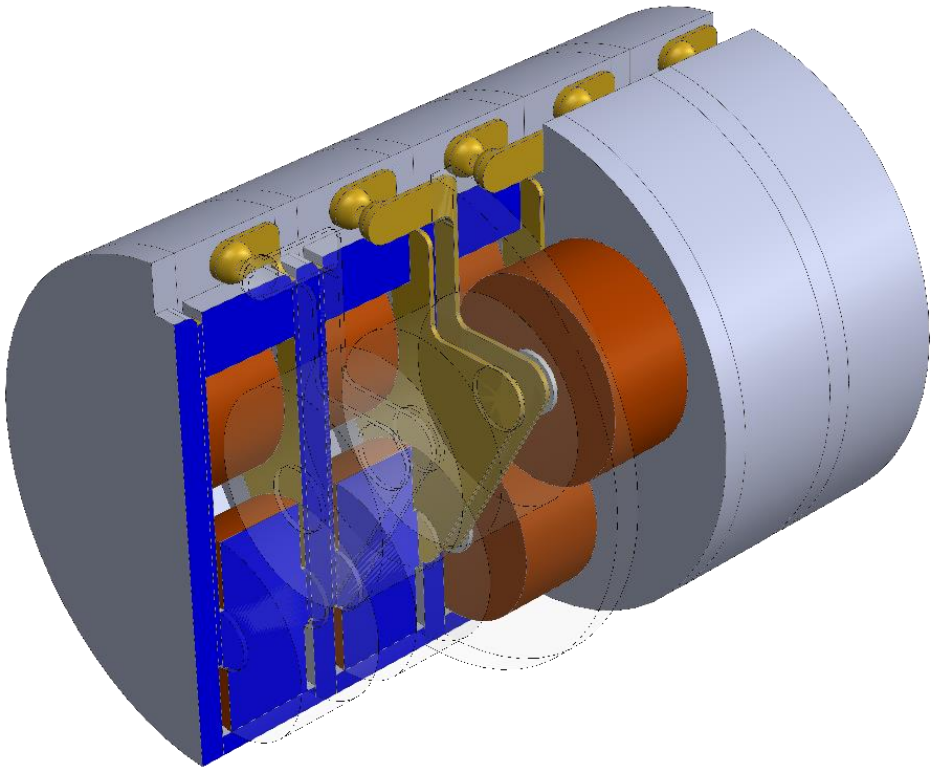

Figure 37 - Partially-sectioned rendering of a simplified Platts-style compact Marx generator with the outer housing removed. Note that the stage buses are connected to the gaps and form a capacitance in parallel with the gap capacitance.

3.3.2 The Pulse Forming Network Marx

One of the principal applications for compact Marx generators is driving relativistic electron beams for the generation of high-power microwave (HPM) pulses [54]. The interactions through which the electron beam generates microwaves are sensitive to the kinetic energy of the electrons and thus the drive voltage of the diode. Due to this, it is generally desirable for the drive voltage to be constant during the pulse. Since the output pulse of a conventional Marx generator driving a constant impedance load is a double-exponential pulse, some form of pulse shaping is necessary to produce the desired square pulse. Traditionally, this was done by employing a pulse forming line (PFL) that was charged by a Marx and discharged into the load [54]. This is an inefficient use of space since the PFL must be sized to store the same energy as the Marx, but it provides no voltage gain.

The pulse forming network (PFN) Marx is one solution to providing the desired output pulse without the size penalty of a separate PFL [55] [56] [39]. In a PFN Marx, each stage is constructed as a lumped-element PFN designed to provide the required pulse shape at 1/N times the voltage and impedance required by the load where N is the total number of stages in the Marx. The stages are typically constructed as Rayleigh type lumped-element transmission lines with discrete capacitors and the inductance distributed in the capacitor interconnects. This construction leads to relatively long, narrow conductor plates sandwiching a row of capacitors as illustrated in Figure 38. In some cases, these lines will be curved into a circular arc for easier incorporation into a cylindrical housing [57] [58].

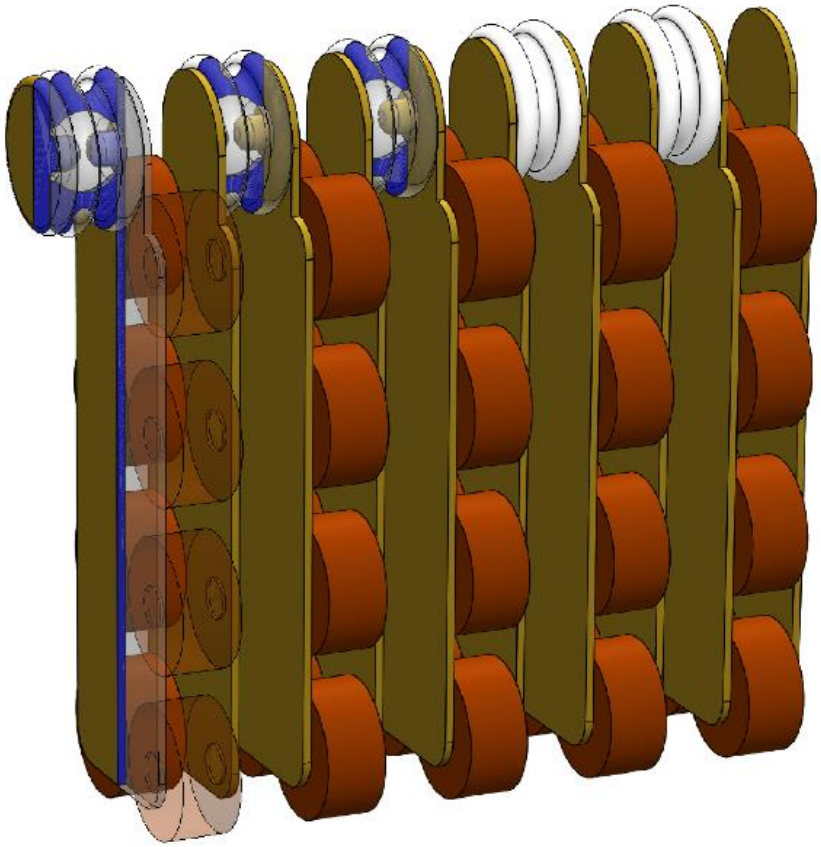

Figure 38 - Partially-sectioned rendering of a simplified compact PFN Marx generator. Note the similarities with the Platts-style Marx and the increased area of the plates that leads to higher inter-stage capacitance.

3.4 Design Techniques for Improved Erection Performance

Increasing the stage-to-ground stray capacitance, C_s, of a Marx generator is a known method of improving erection performance [47]. The previous section demonstrated that the ratio of C_s to the gap stray capacitance, C_g, is the actual quantity one should seek to maximize. This can be accomplished through multiple design choices – each of which requiring certain engineering tradeoffs.

3.4.1 Improving C_s/C_g Ratio Through Geometry

Increasing the distributed C_s that exists from each stage to ground is the most commonly employed technique for attempting to improve the erection performance of a compact Marx generator. That was one of the primary benefits espoused by Platts for the use of a close-fitting metallic housing for the small devices that he developed [59]. Since then, many others have stated that this technique can provide significant improvements in Marx operation [47] [51] [53]. However, when one strives to make a compact, energy-dense design, the stray capacitances scale in such a way that the ratio C_s/C_g is generally quite low – even with a close-fitting grounded housing.

The impact of geometry on stray capacitance relationships has been explored using electrostatic simulations of simplified compact Marx geometries in CST. One of these simulations explored the stray capacitance of a simplified three-stage Platts Marx with each stage containing six ceramic capacitors connected by circular plates as shown in Figure 39. The outer tube and endcap of the tube are modeled as grounded perfect electric conductors (PEC). The internal structure of the ceramic capacitors is modeled as shown in Figure 40. A dielectric tube fills the radial gap between the capacitors and the outer PEC tube. The axial gap between the stages and the radial gap between the capacitors and the outer tube were parameterized to allow varying these values automatically in the simulation. Each side of each of the stages is set to a fixed potential so that the solver can calculate the various lumped-equivalent stray capacitances.

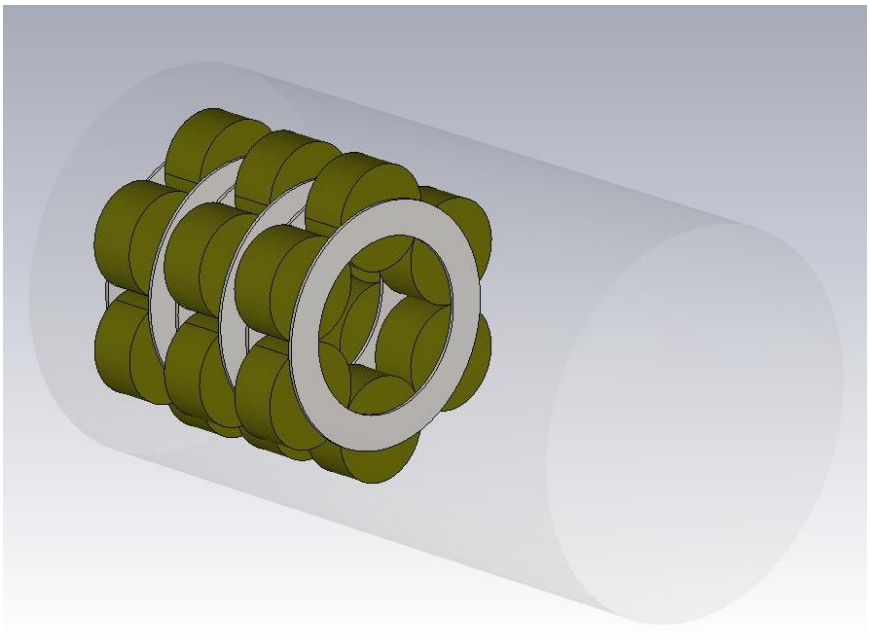

Figure 39 - CST simulation model of three six-capacitor stages in a grounded metallic cylinder housing.

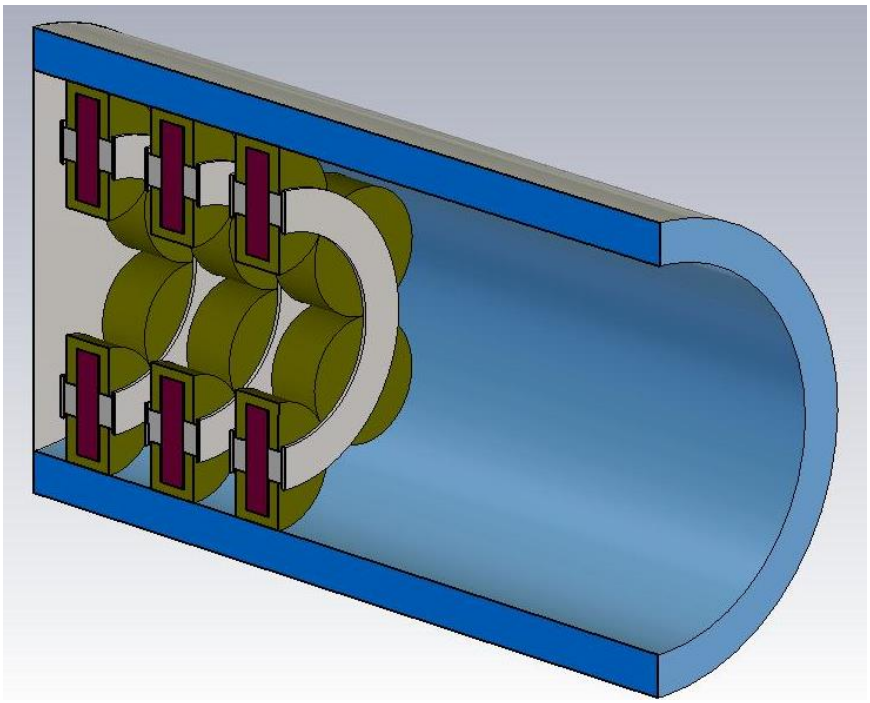

Figure 40 - Sectioned view of the CST model showing the internal structure of the capacitors and the dielectric tube. The extra space at the near end of the tube is intended to make the tube appear infinite in the axial direction away from the stages being analyzed.

For the this simulation, the relative permittivity of the tube was set to 1 and the inter-stage and radial gaps were swept from 1 to 5 cm in 1 cm increments. This gives a set of 25 data points as plotted in Figure 41.

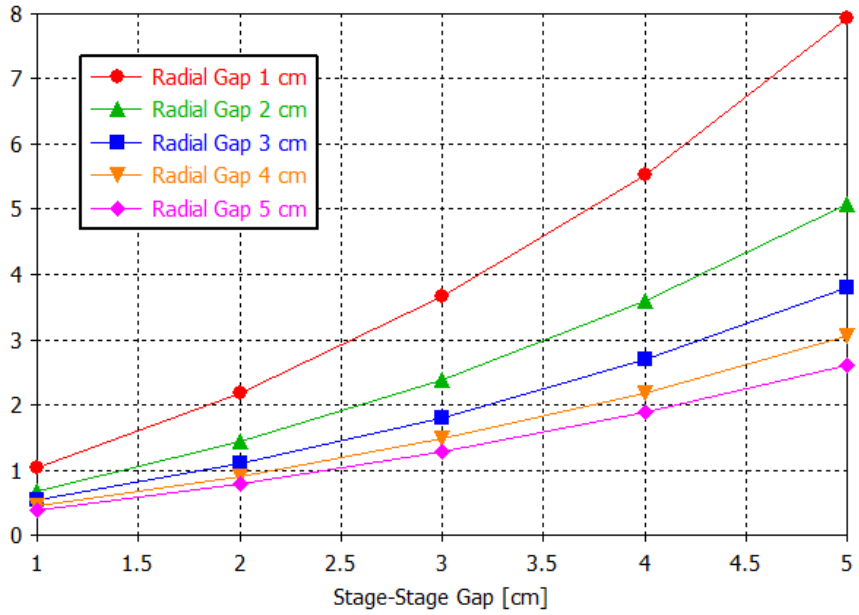

Figure 41 - Plots of the C_s/C_g ratio vs. the inter-stage separation at different values of radial gap for the case where the dielectric tube has a relative permittivity of 1. This is the case where the stages are insulated by the same material as the tube.

The general trends of this data are as expected – smaller radial gaps and larger inter-stage gaps give higher (better) ratios of C_s/C_g. Since the relative permittivity of the dielectric tube was set at 1, this simulation represents a compact Marx with the same dielectric separating the stages as separates the stages from the tube. In this case, it would be reasonable to assume that the radial gap would have to be greater than the inter-stage gap since the inter-stage voltage is never higher than the charge voltage, while the stage-to-ground voltage is the full Marx output voltage during erection. This leads to a geometry – larger radial gap, smaller inter-stage gap – that results in low values of C_s/C_g. To achieve higher values, the stages can be spaced further than the gap dictated by voltage breakdown considerations. However, this reduces energy density, which is often at odds with the system design goals.

3.4.2 Addition of Discrete Stage-to-Ground Capacitance

In some cases, it will be impossible to add sufficient capacitance to ground through the geometry of the Marx construction alone. In these cases, it may be necessary to add actual physical capacitors to couple some of the Marx stages to ground. Since the stage-to-ground coupling capacitor of the n^{th} stage will be subjected to a potential of nV_0 as the Marx erects, this technique is usually limited to the first few stages of a practical design by capacitor voltage ratings. The capacitors are chosen to have a value significantly higher than the stray gap capacitance. This will result in the stages that have coupling capacitors erecting sequentially after the first stage is triggered. This builds up the overvoltage applied to the downstream switches without coupling capacitors so that they will break down quickly despite the lack of a true wave-erection process.

The number of stages that must be fitted with coupling capacitors is dependent of the total number of Marx stages as well as the ratio of C_s/C_g for the stages that do not have coupling capacitors. Marx generators with more numerous stages and lower C_s/C_g will require more ground-coupled stages to ensure adequate erection performance. The following examples demonstrate how this technique has been implemented in previous successful designs.

3.4.2.1 25-Stage Platts Marx

This technique was employed by Platts in the design of a compact 25-stage Marx generator by incorporating a small 180 pF capacitor from the second stage back to ground as shown in Figure 42. This capacitor ensures that the second stage sees nearly the full $2V_0$ overvoltage when the first gap is triggered electrically. This, together with the increased C_s provided by the grounded metal outer housing, provides reliable erection to approximately 85% of self-break as shown in Figure 43.

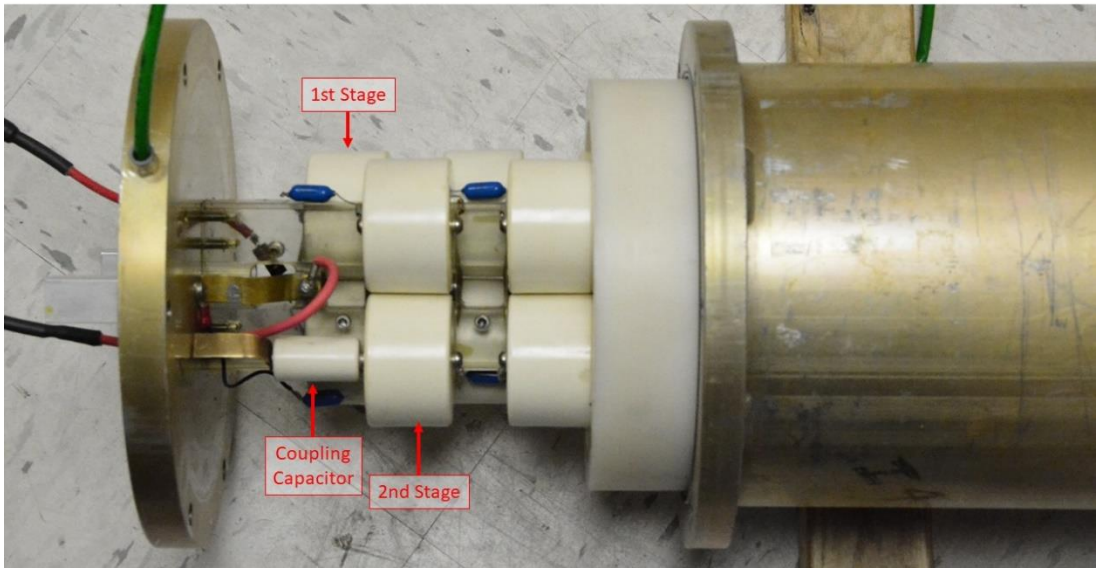

Figure 42 - Photograph of second-stage ground coupling capacitor in 25-stage Platts Marx. The brass strap connects the coupling capacitor back to the grounded endcap of the Marx.

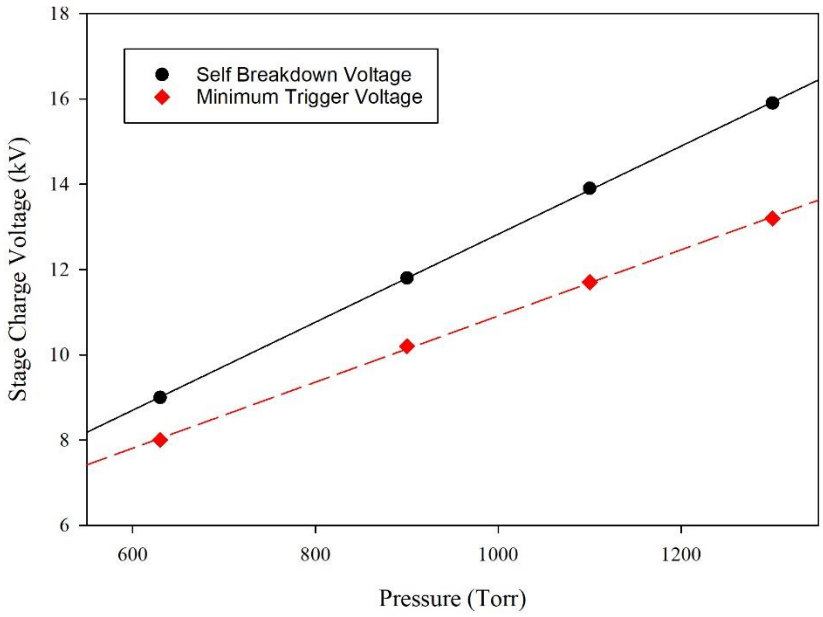

Figure 43 - Plot of self-break voltage and minimum reliable erection voltage as a function of pressure for the 25-stage Platts Marx.

In a nearly identical Marx constructed by Peterkin et al. [52] according to the design provided by Platts, the omission of the metallic outer housing required the coupling of the second through the fourth stages back to ground with discrete capacitors. The

second stage was coupled to ground with a 440 pF 40 kV capacitor, while the third stage was coupled with two of these same capacitors in series, and the fourth stage with three in series. Stacking capacitors in series provides a means to compensate for the increased voltage at each subsequent stage. Since the overvoltage applied to the gaps increases with stage number, the smaller equivalent capacitance of these series strings becomes less of a factor. This arrangement resulted in reliable erection down to approximately 75% of self-break as shown in Figure 44.

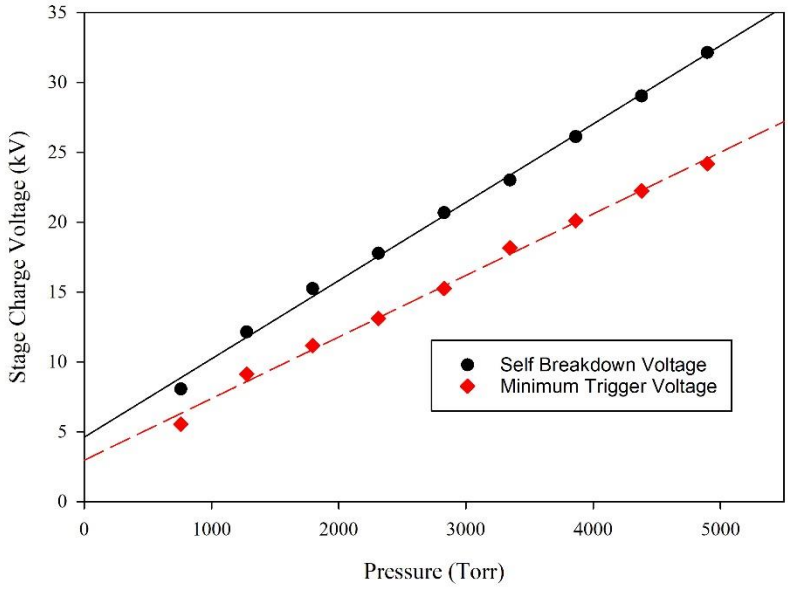

Figure 44 - Plot of self-break voltage and minimum reliable erection voltage as a function of pressure for the 25-stage Platts Marx constructed by Peterkin et al. Reconstructed from data in [52].

3.4.2.2 12-Stage Compact Marx

A third example of the benefits of adding discrete stage-to-ground coupling capacitance is provided by a 12-stage compact Marx built to resemble a design first proposed by Kekez [51]. A sectioned rendering of this Marx is shown in Figure 45. Initially, this design incorporated a metallic housing to act as a pressure vessel, increase C_s, and shield the surrounding equipment from the electrical noise generated by the spark gaps. However, issues with electrical breakdown to the housing necessitated replacing the metal tube with a dielectric plastic tube. This change led to a situation where the Marx would not

erect when the first gap was triggered at any voltage below self-break. The design was modified with the second stage back-coupling capacitor as shown in Figure 45. This resulted in the performance shown in Figure 46. The unusual situation where the minimum trigger voltage decreased slightly as the pressure was increased is not understood.

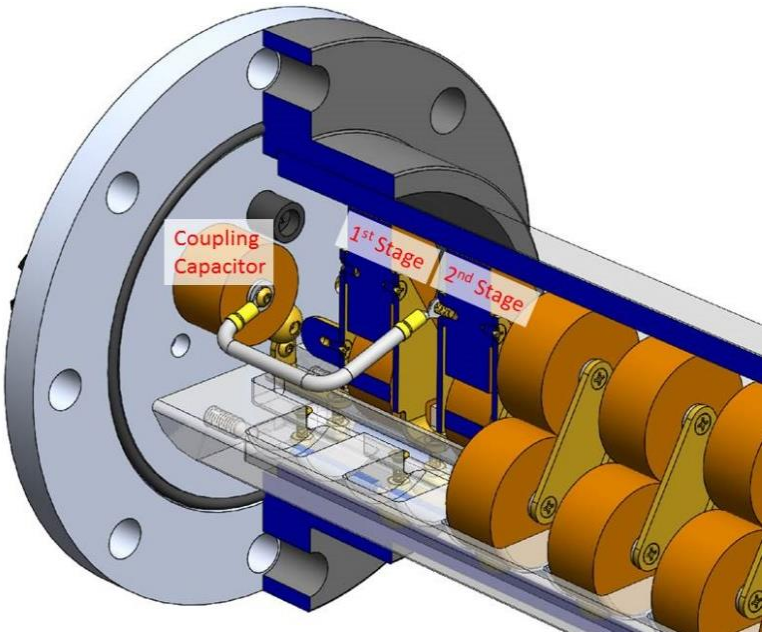

Figure 45 - Sectioned rendering of the 12-stage compact Marx generator. Each stage consists of three 2 nF ceramic capacitors. The spark gaps are located on the underside of the tray in close proximity to the tube in order to increase the stray capacitance to ground in the original design. The second stage ground coupling capacitor was a late addition to the design.

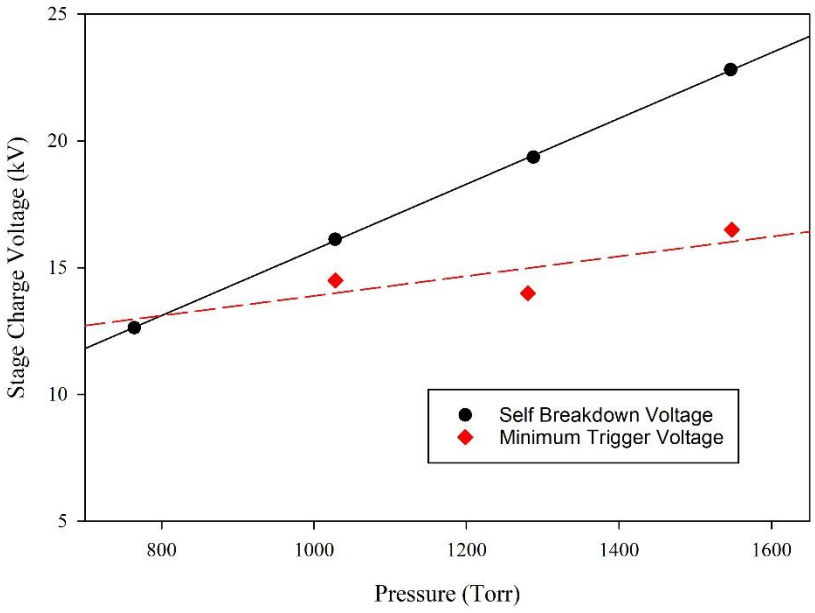

Figure 46 - Plot of self-break voltage and minimum reliable erection voltage as a function of pressure for the 12-stage compact Marx generator with the plastic housing and second-stage ground coupling capacitor.

Since an accurate 3D CAD model of this Marx was available, it was possible to analyze the magnitude of the various stray capacitances using the electrostatic solver in the CST Studio electromagnetic simulation package. The model was simplified to the first three stages as shown in Figure 47.

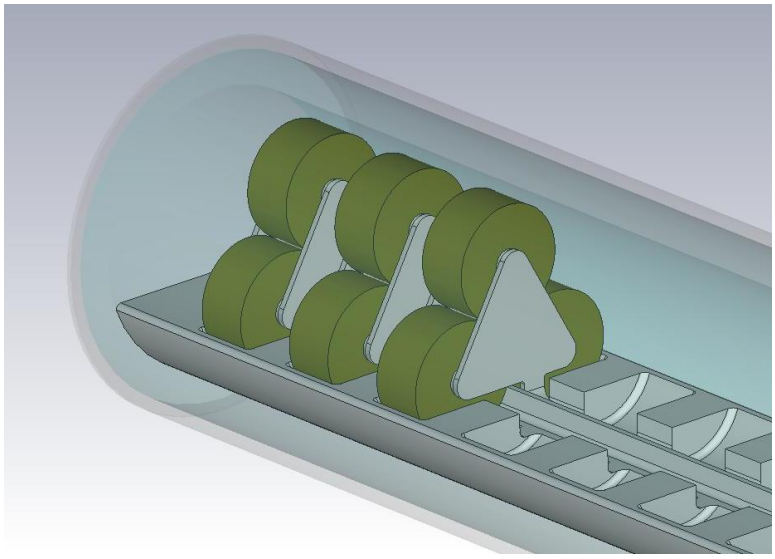

Figure 47 - 3D CAD model used for the electrostatic simulation to determine the stray capacitances of the 12-stage compact Marx. The outer housing and dielectric tube have been made translucent to show the internal components.

Three cases were simulated for this model. In the first, the grounded outer tube was included, as was the third stage. The capacitance between the first and second stages and the second stage and ground were extracted from the simulation. This provides the important values of C_g and C_s for the second gap after the first gap has been triggered externally. The simulation returned values of C_g = 3.9 pF and C_s = 11.6 pF, a C_s/C_g ratio of 3. Referring to Figure 31, this should produce a peak voltage of approximately $1.7V_0$ across the second gap in this configuration. While minimal testing was done in this configuration due to breakdown problems, the Marx did erect reliably.

The second simulation substituted a charge-free open boundary condition for the grounded metal tube. In this configuration the stray capacitance values are C_g = 5.7 pF and C_s = 1.9 pF, a C_s/C_g ratio of 0.33. This would give a peak voltage of $1.2V_0$ across the second gap according to Figure 31. Also, the decay time constant would be 6 times faster than it was for the case with the grounded housing if the charging resistor values are the same. This provides a clear picture of why this Marx performed poorly without the tube. With the 1000 pF discrete second stage back coupling capacitor, the value of

C_s/C_g is 175. This ensures that the second gap peak voltage reaches $2V_0$ and that the overvoltage persists for a relatively long time.

One may question the reason for including the third stage in the simulation since the stray capacitance of that stage was not of interest in the simulation. The reason for including it is that it partially shields the second stage from the grounded housing. This can be an important effect – especially in a very compact design. A third simulation was conducted to quantify this effect by removing the third stage from the model and re-running the simulation with the grounded housing in place. In this case, the value of C_s increased from 11.6 to 13.8 pF – a 19% increase. The value of C_g between stage 1 and stage 2 was unaffected. Thus, the calculated ratio C_s/C_g would have been over-estimated by 19% if the third stage was not included in the simulation.

3.4.3 Negative Consequences of Increased C_s

Increasing C_s to improve the C_s/C_g ratio has benefits for the erection performance of a Marx generator as described above. However, this stray capacitance to ground can have negative impacts on the output of the Marx. The most apparent impact is the reduction in Marx voltage efficiency – or the ratio of actual output voltage to NV_0. This occurs due to the energy required to charge all of the C_s as the Marx erects. It is particularly significant for very small, low-energy Marx generators where C_s may be a significant fraction of the Marx stage capacitance. This effect can be estimated by analyzing the voltage division between C_m and C_s in a stage-by-stage fashion to develop a general expression for the voltage loss. The first three iterations of this process are shown schematically in Figure 48 and as equations (16) through (18).

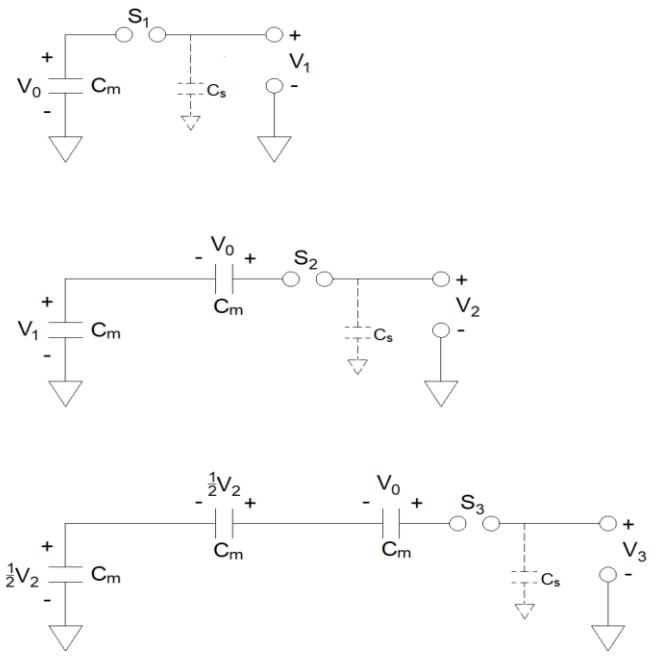

Figure 48 - Schematics used in the first three iterations of the voltage division calculation.

$$V_1 = V_0\left[\frac{C_m}{(C_m+C_s)}\right] \tag{16}$$

$$V_2 = V_0\left[\frac{C_m^2}{(C_m+C_s)(C_m+2C_s)} + \frac{C_m}{(C_m+2C_s)}\right] \tag{17}$$

$$V_3 = V_0\left[\frac{C_m^3}{(C_m+C_s)(C_m+2C_s)(C_m+3C_s)} + \frac{C_m^2}{(C_m+2C_s)(C_m+3C_s)} + \frac{C_m}{(C_m+3C_s)}\right] \tag{18}$$

This sequence of equations is extended until the total number of stages in the Marx is reached. This sequence can be shown to be equivalent to the expression:

$$V_n = V_0\frac{\sum_{j=0}^{n-1}\left[\prod_{k=0}^{j}(1+kx)\right]}{\prod_{k=0}^{n}(1+kx)} \quad x = \frac{C_s}{C_m} \tag{19}$$

As an example, the value of V_n/V_0 has been plotted as a function of C_s/C_m in Figure 49 for the case of N = 4 (i.e. a four-stage Marx). As expected, the output is $4V_0$ for the case where $C_s = 0$. The rapid decrease in voltage with increasing C_s/C_m shows that low energy Marx generators will suffer from poor output voltage efficiency if C_s is made too large. This must be considered in the design of compact Marx generators or inadequate performance will result.

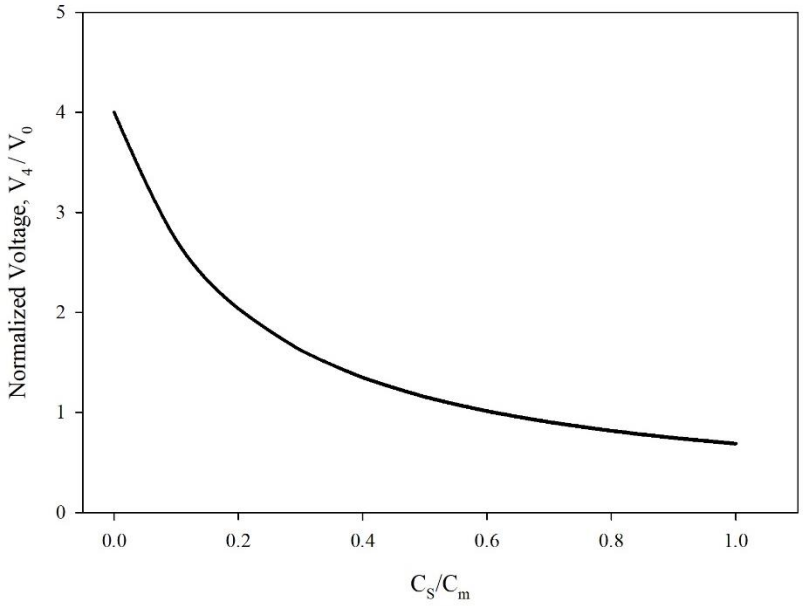

Figure 49 - Plot of normalized output voltage, V_4/V_0, as a function of C_s/C_m for the case of a four-stage Marx generator.

An example of the significant reduction in output due to increasing the stray capacitance to ground can be seen in the results of measurements taken with the 25-stage Platts Marx described in section 3.4.2.1. This Marx was fired into an open circuit at the same charge voltage (9 kV) both with and without the grounded metal outer tube. The output was measured with a North Star VM series high voltage probe. The resulting waveforms are shown in Figure 50.

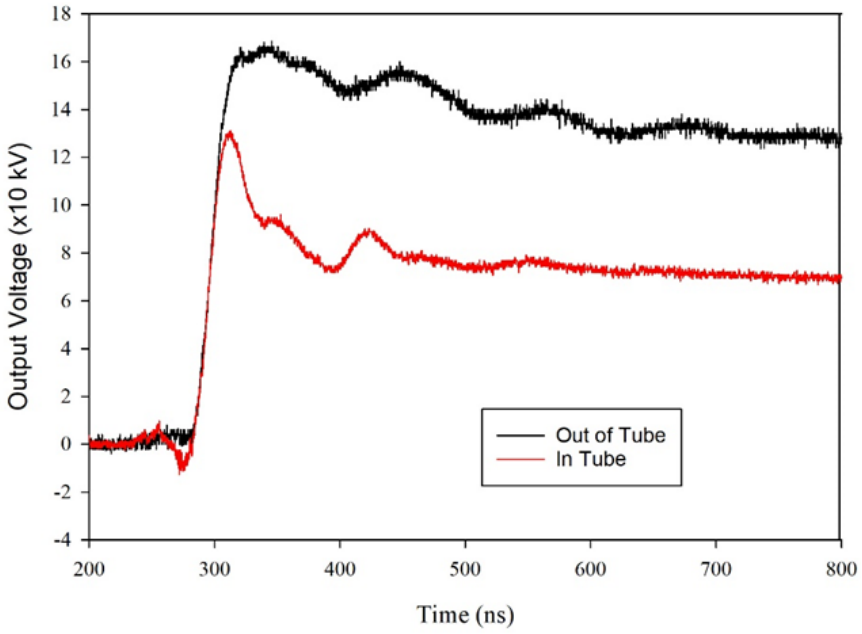

Figure 50 - Plot of open-circuit output of the 25-stage Platts Marx with and without the grounded outer tube. Note the significant (~20%) reduction in peak output voltage due to the increased stray capacitance to ground caused by the tube.

Equation (19) can also be rearranged to represent the voltage added by each additional stage when the loss due to the stray to ground is considered:

$$V_n = (V_{n-1} + V_0) \cdot \left[\frac{C_m}{C_m + nC_s}\right] \tag{20}$$

Note that the voltage added by an additional stage is inversely proportional to the total number of stages due to the nC_s term in the denominator. This leads to the conclusion that maximum voltage efficiency is realized by minimizing the number of stages for a given output voltage. This can be achieved by using the highest possible stage voltage, which makes insulation more difficult. Bipolar charging is one technique that could be employed to reduce insulation stress for a given stage voltage.

CHAPTER 4
MICRO-LASER TRIGGERED GAS SWITCHES

4.1 Introduction

The discovery of the technique of Q-switching a laser to generate very intense short pulses of laser energy was first described by McClung and Hellwarth in early 1963 [60]. Within the same year, the ability of these pulses to directly ionize gasses was discovered [61] and this process was very quickly applied to the triggering of spark gap switches, and found to have significant benefits over electrical triggering [62] [63] [64] [65]. However, it was approximately 20 years before laser triggered switches were incorporated into a major pulsed power system [66].

The long delay between the discovery of laser triggering and its practical application was due in large part to two factors. The first was the time needed for the maturation of laser technology, since early laser triggering experiments took place with very rudimentary laser systems. The second was that the significant size, complexity, and cost of the necessary laser system meant that its use as a trigger was only practical for very large pulsed power systems with demanding performance requirements. This factor led laser triggered switches to be associated with large and complex pulsed power systems. With recent significant advances in compact high-power pulsed laser technology driven by the manufacturing, medical, and remote sensing fields, laser triggered switches can be considered for highly compact pulsed power systems.

One interesting development in laser technology that holds promise for application in compact pulsed power is the passively Q-switched diode-pumped solid-state (DPSS) micro-laser. DPSS lasers are a class of lasers in which the laser gain medium is a crystalline or glass substrate doped with an element that exhibits a useful laser transition. This gain medium is pumped by a semiconductor diode laser tuned to the peak absorption of the gain medium. This is done instead of directly using the output of the diode laser because the beam quality of high power diode lasers is intrinsically poor – thus limiting the ability to focus the beam to a very small spot [67]. By efficiently

pumping the solid-state gain medium with the diode laser light, a high-quality output beam is achieved, allowing for tight focusing and the high-power density at the focus. Q-switching is a technique of optical power compression in which energy is stored in the gain medium over a long period of time and then released in a short large-amplitude pulse. This is accomplished by inhibiting resonance in the laser resonator during pumping until the maximum amount of energy has been absorbed and then quickly removing this inhibition. Passive Q-switching implements this inhibitory mechanism through the use of a saturable absorber material placed in the laser cavity. The key to implementing this technique in small, robust lasers was the discovery of chromium+4 doped crystalline saturable absorbers [68].

One application of the passively Q-switched DPSS laser is in the generation of high-power nanosecond pulses of infrared light for use in range determination and LIDAR applications. The requirements for the lasers for these systems – high peak power, short pulse width, repetitive operation, and eye-safe wavelength – give them potential as laser triggering sources for compact pulsed power. The requirement for eye-safety drives these devices toward the 1500 nm range of wavelengths where water is strongly absorbing. This results in the interocular fluid preventing the laser energy from reaching the retina – thus significantly reducing the potential for eye damage. Erbium-doped glass lases at 1535 nm and has a long upper-state lifetime, which permits good energy storage in the gain medium at low pump power [69]. This has made Er:glass DPSS lasers very popular for these applications.

While laser triggering of spark gap switches has been demonstrated using near infrared light at 1064 nm [70] [71], no research on the use of wavelengths in the 1500 nm range was found in the literature. Thus, the first goal was to determine if triggering is even possible using one of the readily available Er:glass passively Q-switched DPSS lasers.

4.2 Experimental System

The experimental setup used to obtain the data described in this chapter is shown in Figure 51 and the major components are described in the following sections. This setup was modified for some of the experiments. Those modifications will be described in the relevant sections.

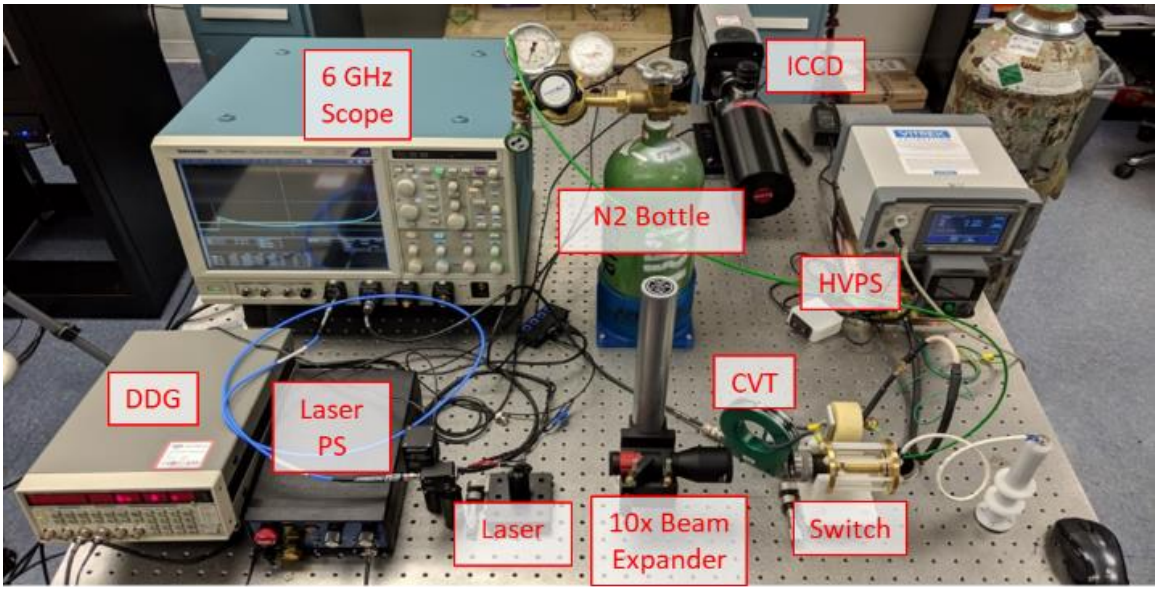

Figure 51 - Labeled photograph of the complete experimental system.

4.2.1 Laser

The laser used for these experiments is an Er:glass passively Q-switched DPSS laser that is integrated into a cylindrical package 9 mm in diameter by 28 mm long. It is a commercially available device manufactured by MegaWatt Lasers Inc. as part number ER902. This laser was developed for use in laser rangefinder applications. A photograph of this type of laser is shown in Figure 52. A list of important performance parameters is given in Table 2.

Figure 52 - Photograph of laser used for experiments with U.S. dime for size reference. The cylindrical package shown includes the pump diode and complete solid-state laser resonator assembly.

Table 2
ER902 Laser Manufacturer's Specifications

Parameter	**Nominal Value**
Wavelength	1535 nm
Average pulse energy	244 µJ*
Pulse energy 1σ SD	4.7 µJ*
Pulse width	4 ns FWHM
Maximum pulse rep rate	10 Hz
Beam quality M^2	≤1.3
Resonator mode	TEM_{00}
Beam divergence	7 mRad
ANSI Classification	Class 1

* Manufacturer measured values at 10 Hz rep rate over 10,000 shots for the actual unit used

4.2.2 Optical System and Switch

The optical system through which the laser beam is delivered from the laser to the target electrode consists of three optical elements. The first is a 10x beam expander that is mounted on an optical post between the laser and the switch assembly. This expander has an adjustable focus and the optics are anti-reflection (AR) coated for the 1050 to 1650 nm wavelength range. The purpose of the beam expander is to collimate and expand the diverging beam that exits the laser before it is focused on the electrode. The final focused spot size is inversely proportional to the focusing lens input beam diameter – thus a larger beam can be focused to a higher intensity on the electrode. The beam exiting the expander is well collimated and approximately 10 mm in diameter.

This beam enters the focusing lens, which is mounted in a focus adjusting tube screwed into the back of the first electrode of the switch. The focus tube allows the focusing lens axial position to be varied over a range of approximately 4 mm. The lens is a 40 mm focal length best-form spherical lens. This type of lens has two spherical surfaces of differing radii to produce the least spherical aberration possible without resorting to complex aspheric shapes. The lens is AR coated for the 1050 to 1700 nm range. Before entering the switch housing through the laser entrance hole, the converging beam passes through a fused silica window that provides the barrier for the pressurized gas in the switch. This window is sealed to the electrode with an o-ring and is AR coated on both surfaces. The total loss due to reflection at the optical interfaces is estimated at less than 1% for the complete optical system based on manufacturer's data.

The switch consists of two machined brass electrodes that fit into a 1.5-inch inner diameter, 0.25-inch wall thickness acrylic tube. The electrodes seal to the tube with o-rings and are secured together with threaded nylon rods. The first electrode, through which the laser enters the switch, is fitted with a threaded bore in the back to permit the installation of the window and focusing optics. A hole is provided through the axis of the electrode for the beam to pass. The second electrode, which includes the laser target insert, extends across the majority of the length of the switch. This permits the use of a shorter focal length lens and thus a smaller spot size. The switch is held rigidly in place concentric with the laser beam by a stereolithography printed dielectric stand. An illustration of the cross-section of the switch and integrated optical elements is shown in Figure 53.

The laser target is a 0.25-inch diameter 0.05-inch thick replaceable insert onto which the laser is focused. This insert was fabricated from commercial graphite of grade B325. The choice to use graphite was informed by previous experiments [70] [71] as well as the ease with which it could be machined into suitable inserts. Each time a new insert was installed into the electrode, the insert and surrounding electrode shoulder were wet sanded and polished with fine sandpaper and jeweler's rouge polishing compound to produce a smooth surface finish.

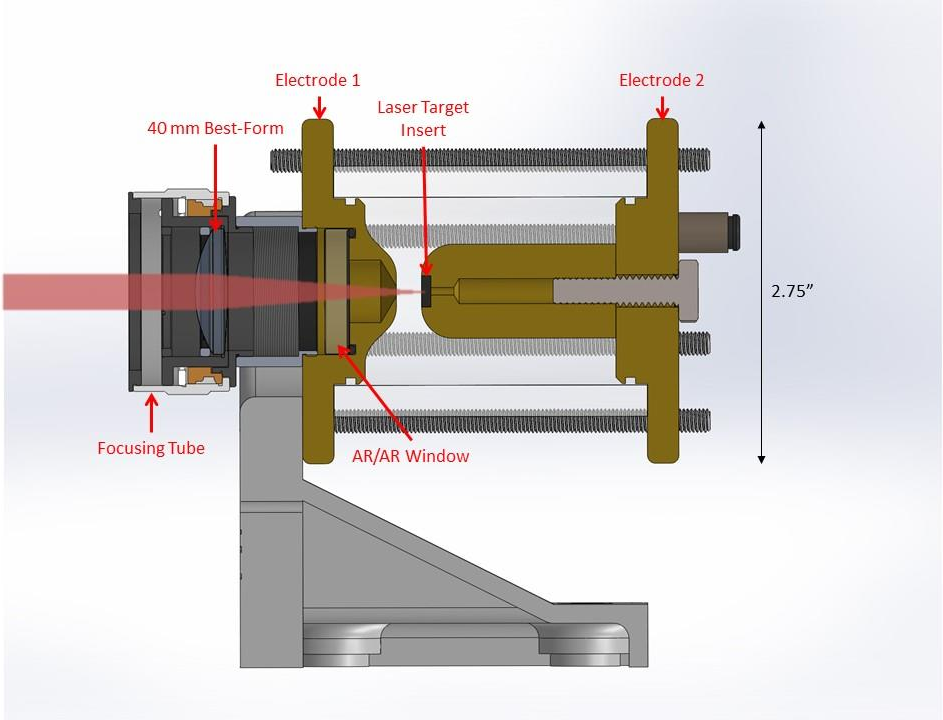

Figure 53 - Labeled and cross-sectioned rendering of the pressurized gas switch used for experiments.

4.2.3 High Voltage Power Supply

The experimental switch is configured to discharge a high voltage ceramic capacitor through a fixed load resistor. The capacitor is charged by a Glassman MK series high voltage power supply. Two supplies are available – one of each polarity – thus permitting the exploration of polarity-dependent effects on the laser triggering performance. Only one supply is connected to the experiment at a time. The voltage and current output of the supply is controlled manually. The supply is isolated from the discharge capacitor via a 1 MΩ high voltage resistor.

4.2.4 Diagnostics

Diagnostics for the experiment consisted of both electrical and electro-optical measurements. Data was primarily collected on a Tektronix 6 GHz digitizing oscilloscope. Inputs to the scope consisted of an InGaAs photo-diode detector and a Pearson wideband current monitor. The photo-diode detector has a bandwidth of 5 GHz and is sensitive to wavelengths from 800 to 1700 nm. It was mounted such that it could detect

the small amount (approximately 0.1%) of energy reflected from the first lens in the beam expander. This is sufficient to produce a signal of tens of mV which is easily detectible by the oscilloscope. The oscilloscope capture is triggered from the photo-diode signal. The wideband current monitor has a bandwidth of 250 MHz and can measure pulsed currents up to 500 A. The current monitor was mounted to measure the discharge current that occurs when the switch gap breaks down. An additional high voltage voltmeter was used to measure the charge voltage on the switch to better than 0.1% accuracy.

4.2.5 Laser Irradiance and Fluence Estimation

The intensity of the laser at the focused beam spot on the target insert is an important parameter for scaling this experiment relative to previous research and understanding the potential processes that can be occurring in the interaction between the beam and the surface [72]. The intensity can be stated in terms of irradiance (W/m^2) or fluence (J/m^2), which are functions of laser power (or energy) and spot size. Energy is easily measured using a pyroelectric sensor. Power is easily calculated from the measured energy per pulse and the pulse shape. Unfortunately, it is very difficult to directly measure the spot size for such an intense laser pulse. However, enough information is available to calculate an estimate of the spot size. This can be compared to the measured size of the hole left in the target insert by the laser to validate the estimate.

The minimum possible spot size for a given set of laser parameters is given by:

$$r_{min} = \frac{M^2 f \lambda}{\pi r_o} \tag{21}$$

where M^2 is the beam quality factor, f is the lens focal length, λ is the laser wavelength, and r_0 is the beam radius at the focusing lens. In this case, r_0 is the beam radius out of the expander, which is approximately 5 mm. The values for M^2 and λ (1.4 and 1535 nm respectively) are found in Table 2 and the lens focal length (40 mm) is found in section 4.2.2. These parameters give a diffraction limited spot radius of 5.5 µm. This yields a spot area of 9.5×10^{-11} m^2. It is very unlikely that the actual spot size is this small, due to

imperfections and aberrations in the optical system such as imperfect focusing and spherical aberration. However, care has been taken to minimize these to the extent that the spot area is most likely on the order of 10^{-10} m^2. This is supported by the measured laser ablation hole sizes described in section 4.7.

The temporal shape of the laser pulse can be approximated by a Gaussian function with full width at half-maximum (FWHM) of 4 ns, as illustrated in Figure 54:

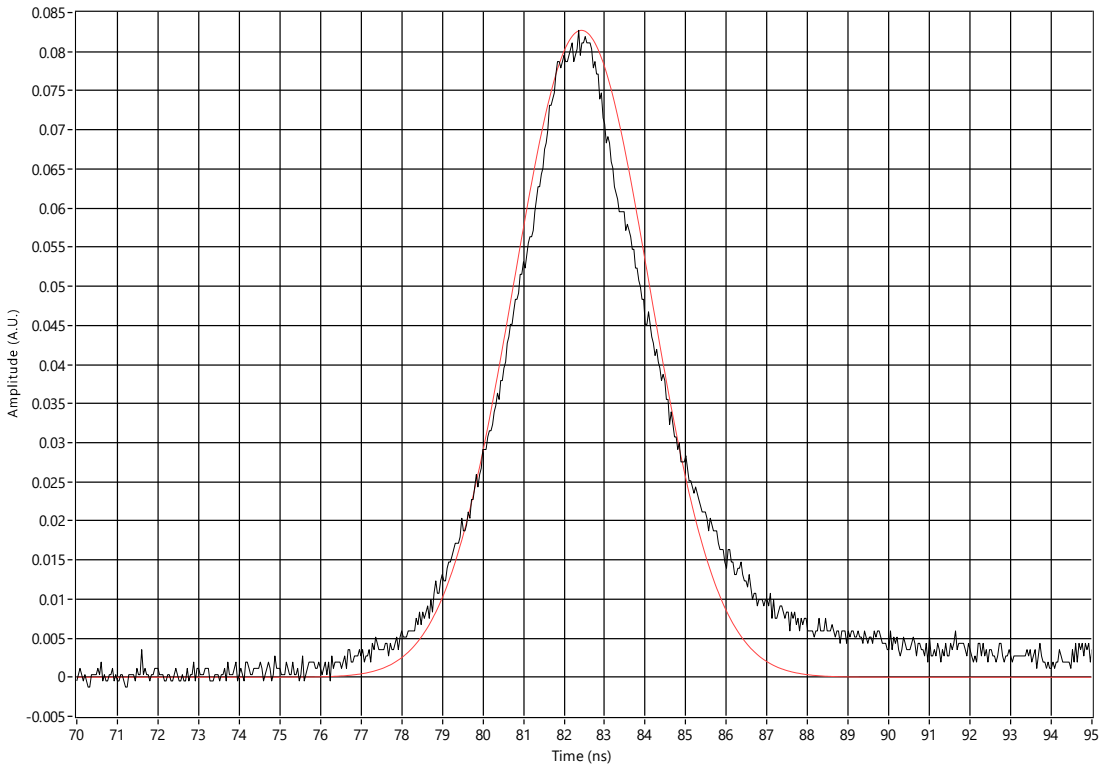

Figure 54 - Fitting of a Gaussian function to the laser pulse envelope as measured by the photo-diode detector. The FWHM of the Gaussian fit is 4 ns. The mean absolute error in the fit is approximately 1% of the peak.

The peak power in a Gaussian pulse is equal to:

$$P_{peak} = 0.94 \frac{W_{pulse}}{t_{FWHM}} \tag{22}$$

While the manufacturer's measured pulse energy for this unit was 244 µJ at 10 Hz, measurements at the low repetition rate used in these experiments generally gave an average energy in the range of 220 µJ due to the impact of reduced temperature on resonator alignment. Using this energy, the peak power calculated for these

experiments was approximately 52 kW. This yields an estimated irradiance on the order of 10^{14} W/m^2 and fluence on the order of 10^6 J/m^2. These values are within the range of those used for laser induced breakdown spectroscopy (LIBS) and should produce a plasma plume with a significant population of free electrons (between 10^{21} and 10^{24} m^{-3}) [72]. The laser plasma is a bright white plume at the surface of the target insert that is easily visible to the naked eye and is estimated to be 100 µm in diameter, as shown in Figure 55.

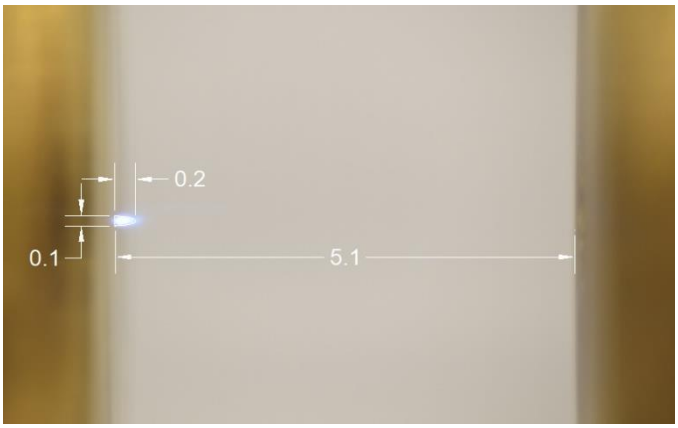

Figure 55 - Open-shutter photograph of the laser plasma plume taken using a long-distance microscope. The dimensions are in millimeters. The imaging focal plane is at the location of the plume – the small depth of focus produces the blurring of the electrodes' edges.

Based on the photograph shown in Figure 55, the volume of the plasma plume is estimated as 10^{-12} m^3. This gives an estimated electron population of between 10^9 and 10^{12}.

4.3 Methodology

This section describes the basic procedure used to collect the data presented in this chapter. This procedure consisted of three steps conducted whenever a new set of experimental parameters was to be tested. Additions and modifications of this procedure will be described in the relevant sub-sections.

4.3.1 Setup and Self-Break

First, if the switch has been left de-pressurized for longer than a few minutes, the gas in the switch is purged by filling the switch to at least 20 psig and emptying it a minimum of three times. Then, a pressure set point is selected for the experiment and the switch pressure is adjusted accordingly. The power supply is enabled and the charge voltage is increased until the switch self-breaks. The charge current is adjusted to achieve repetitive self-break at a rate of 2 to 3 Hz. The switch is permitted to repetitively self-break for approximately one minute at this rate for conditioning.

The self-break voltage of the switch at the set pressure is determined by slowly increasing the charge voltage while observing the measured voltage on the high voltage voltmeter. The voltage at which the gap breaks down is noted and rounded to the nearest 0.1 kV. The process is repeated until the voltage becomes repeatable to within 0.1 kV for at least 5 shots in a row. This value is recorded as the self-break voltage and then used to calculate the test voltages at the desired increments of self-break.

4.3.2 Laser Focusing and Minimum Trigger

After the self-break voltage has been determined for a particular pressure, the laser focus is adjusted to minimize the charge voltage necessary for triggering. With the charge voltage set at zero, the laser is set to run at one pulse per second. The charge voltage is slowly increased until the switch reliably triggers on each laser pulse. Then the voltage is decreased until the switch stops triggering. With the laser still pulsing, the focus is slowly adjusted in one direction and then the other for up to one full turn (0.5 mm). If the switch starts firing reliably at a new position of the focus, then this is taken as a better focus point. This process is repeated until the switch can no longer be made to trigger reliably. The lowest voltage at which the switch will trigger reliably is recorded as the minimum trigger voltage.

4.3.3 Data Collection and Analysis

Data for a given set of experimental parameters is collected in 100 shot runs at a low repetition rate (either 0.5 or 1 Hz). The waveforms for all 100 shots in a run are collected

by the oscilloscope and are saved as ASCII files. An example oscilloscope capture screenshot is shown in Figure 56.

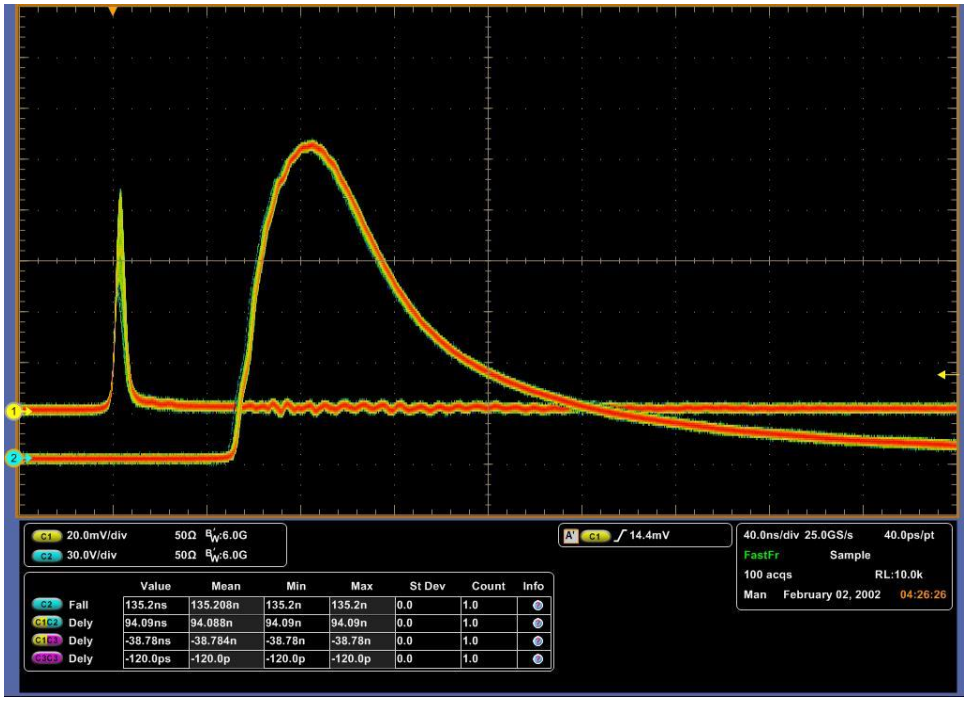

Figure 56 - Screen capture showing an overlay of the 100 shots of waveforms captured at 40 psia, 80% of self-break in the negative (cathode target) polarity. The laser signal pulse is the sharp spike in the channel 1 trace. The channel 2 trace is the current waveform.

Post-processing is performed with a LabVIEW application to derive the run time and jitter values. Run time is defined as the time from the 50% level of the rising edge of the laser pulse to the 10% level of the rising edge of the current pulse. Shots that did not result in breakdown of the gap are discarded. The jitter is defined as the 1-σ standard deviation of the run time from the mean run time – both of which are calculated assuming a normal distribution.

4.4 Initial Proof of Concept Experiments

4.4.1 Motivation

Since no published experiments could be found for triggering spark gap switches with a laser operating in the 1500 nm range of wavelengths, initial experimentation was focused on determining if it was feasible to do so and the effects of basic parameters like charge voltage, charge polarity, gas pressure, and laser target material. Because the energy of the laser was at the very low end of published results for other wavelengths, it was initially assumed that if it worked, it would be marginal at best.

Run time and the jitter (1-σ standard deviation of run time) were chosen as measurements that could be accurately recorded and should reveal the effects of varying parameters. This choice is supported by a long history of research showing that increases in run time and jitter generally accompany degradation of a switch prior to failure. Minimal jitter in particular is often used as the principal figure of merit for triggered switches in pulsed power systems. This is due to the need to synchronize fast diagnostics in experiments driven by a pulsed power system or by the desire to synchronize multiple switches in a large multi-module system. While these requirements are not necessarily present in the applications of compact pulsed power systems, the measurement of jitter still provides insight into the performance of the switch.

Another figure of merit that is applicable to compact pulsed power systems is triggering range – defined as the ratio of self-break voltage to the minimum charge voltage that gives 100% reliable triggering. This is an important performance measure because the statistical nature of breakdown forces the operation of a triggered switch at some fraction of self-break to reduce the probability of pre-fire. The necessary margin is determined by the tendency of the switch in question to pre-fire as well as the system tolerance to pre-fire. Since recovery of voltage holdoff is a process that proceeds over a finite period of time [73], during repetitive operation the full static self-break voltage may not be obtained between shots. Thus, the dynamic self-break voltage is lower and

increasing the trigger range enables increased repetition rate while maintaining freedom from pre-fire.

4.4.2 Setup

The setup used for the experiments described in this section was the basic setup described in section 4.2.

4.4.3 Run Time and Jitter Measurements for Both Polarities

The data presented below was collected for both charge polarities over a pressure range of 20 to 40 pounds per square inch absolute (psia). Table 3 lists the self-break and minimum trigger voltages at the pressures tested.

Table 3
Baseline Self-Break and Minimum Trigger Voltages

Cathode Target Polarity			
Pressure (psia)	Self-Break (kV)	Minimum Trigger (kV)	Minimum Trigger (%SB)
20	14.6	5.4	37%
25	17.8	7.6	43%
30	21.1	8.2	39%
35	24.0	9.7	40%
40	27.0	11.5	43%
Anode Target Polarity			
Pressure (psia)	Self-Break (kV)	Minimum Trigger (kV)	Minimum Trigger (%SB)
20	14.6	9.4	64%
25	17.8	12.8	72%
30	21.0	14.5	69%
35	23.8	17.2	72%
40	27.0	19.2	71%

The self-break voltages are essentially identical for the two polarities, which is to be expected given the uniformity of the electric field in the gap. However, there is a distinct difference in the minimum trigger voltage, with the cathode laser target configuration producing significantly lower minimum trigger voltages. The cathode target

configuration also shows shorter run times and significantly lower jitter than the anode target configuration, as shown in Figure 57 through Figure 60. An interesting observation is that the dependency of run time and jitter on pressure is much larger in the anode target configuration than in the cathode target case. These observations may be indicative of significantly different phenomena occurring for the two cases. Early work in laser triggering by Guenther [63] using a ruby laser at 694 nm also showed a polarity dependence – but he noted that the anode target configuration provided the best performance. This result was also observed by Lehr and others [70] [74] when using an Nd:YAG laser at 1064 nm. Further investigation is required to determine the source of this asymmetry and the differences between the present results and the previous work.

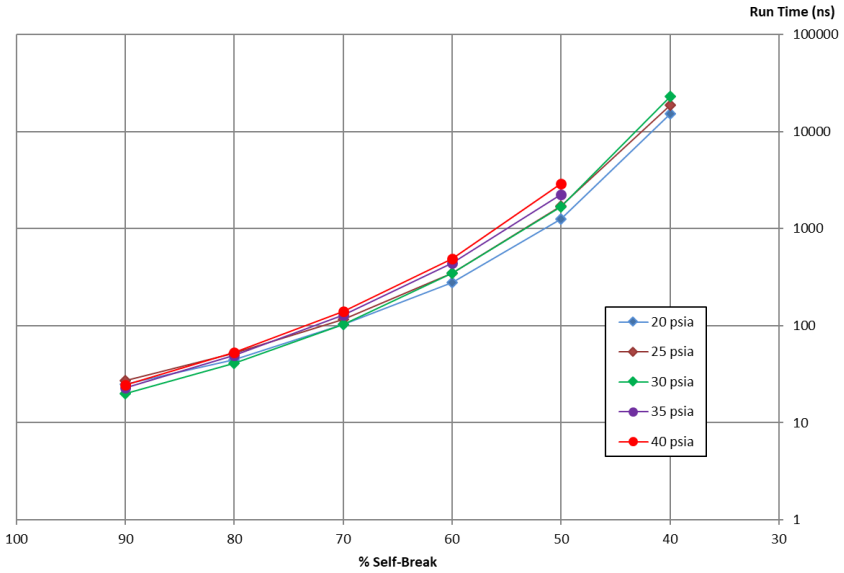

Figure 57 - Plot of the run times of the switch as a function of percent of self-break voltage. Laser focused on cathode. Run time is a strong function of charge voltage and a weak function of pressure with higher pressures generally leading to longer run time.

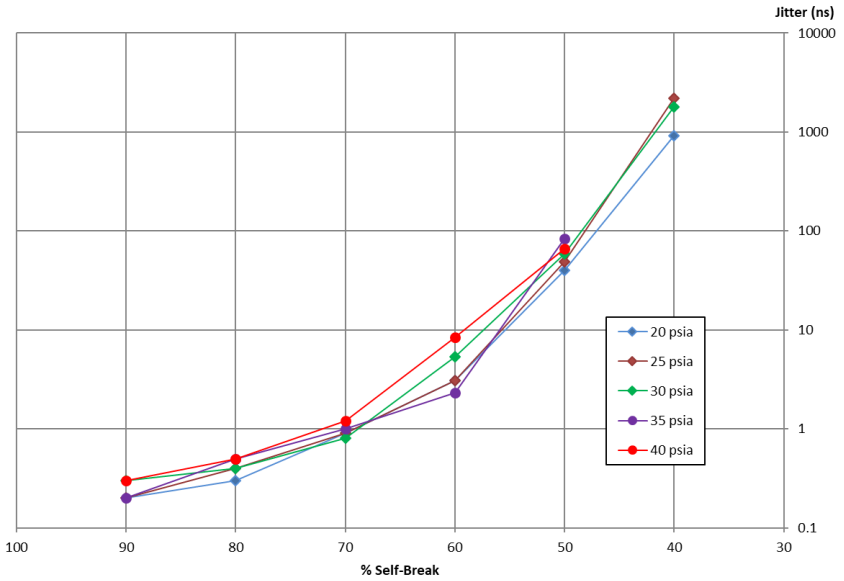

Figure 58 - Plot of the 1-σ jitter of the run times of the switch as a function of percent of self-break voltage. Laser focused on cathode. Jitter follows the same trends as the run times.

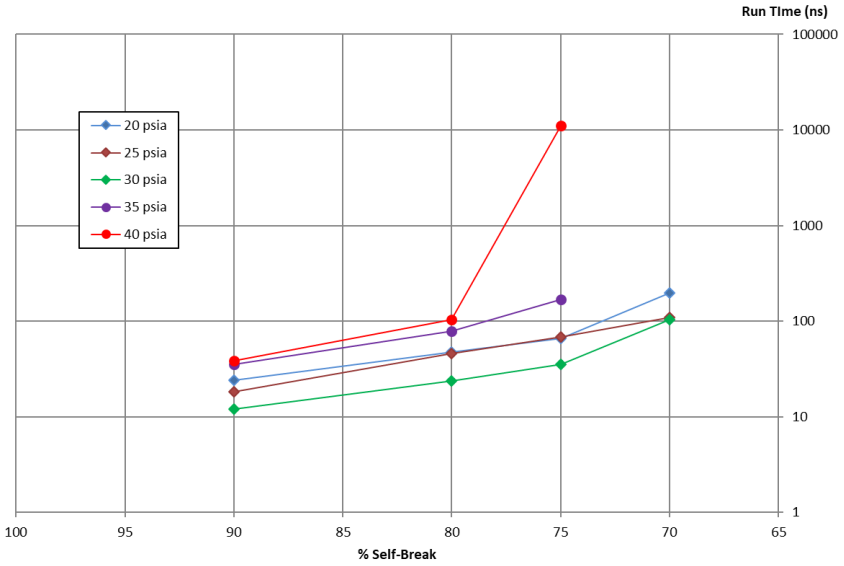

Figure 59 - Plot of the run times of the switch as a function of percent of self-break voltage. Laser focused on anode. Compared to the cathode target case, the run times are longer, and the effect of pressure is more pronounced. Also, the minimum percentage of self-break for triggering is much higher.

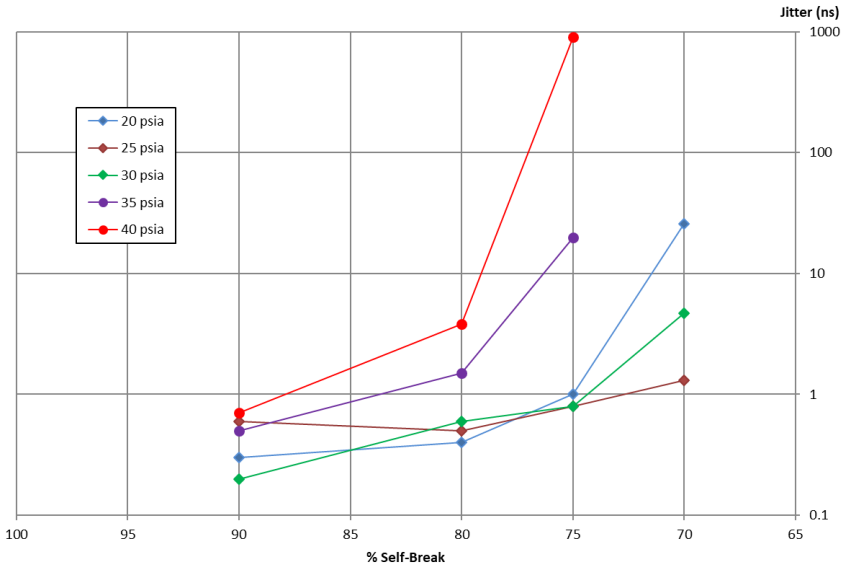

Figure 60 - Plot of the 1-σ jitter of the run times of the switch as a function of percent of self-break voltage. Laser focused on anode. Jitter follows the same trends as the run times and is significantly worse than the cathode target configuration.

4.4.4 Effect of Charged vs. Grounded Target Electrode

Since the applied charge is unipolar in the present experimental configuration, an additional experiment was conducted to verify that the observed polarity effect depended only on the applied field and not which electrode was at ground potential. This was accomplished by grounding the target electrode and applying the high voltage to the laser entrance electrode. The test procedure was then repeated at a pressure of 25 psia. The resulting data is presented in Figure 61 and Figure 62. The behavior of the switch was found to be dependent on the direction of the applied field and not on which electrode was grounded. While this would be expected given the electric field uniformity in the gap, previous researchers had found slightly better performance when the charged electrode was used as the target [74].

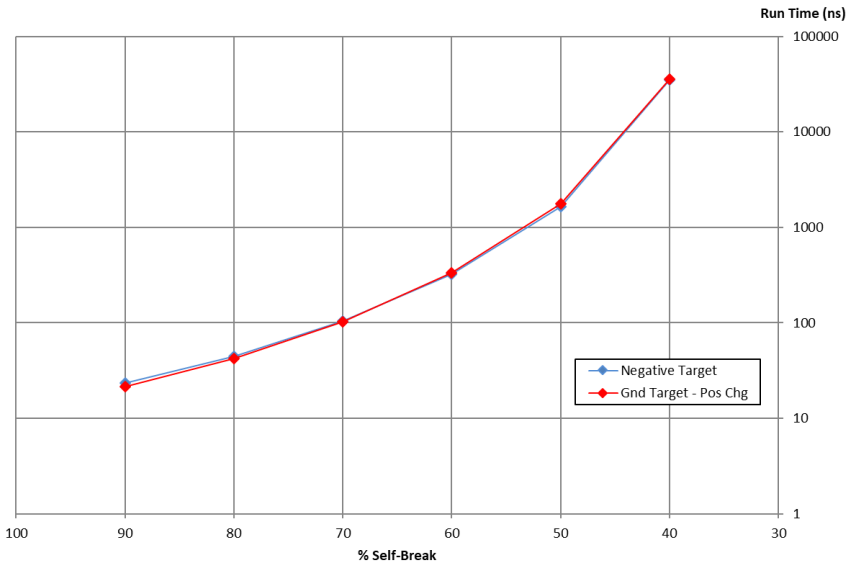

Figure 61 - Plot of the run times of the switch as a function of percent of self-break voltage for two cases. The blue trace is a control where the cathode is the target and the charged electrode. The red trace is the case where the cathode is the target, but it is grounded (i.e. the entrance electrode is charged positive). Note that the traces are almost identical.

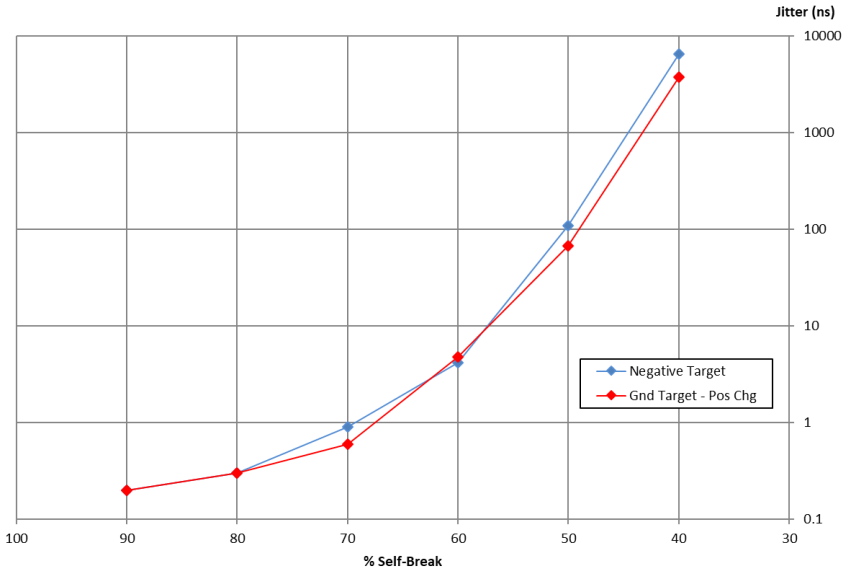

Figure 62 - Plot of the 1-σ jitter of the run times of the switch as a function of percent of self-break voltage for the same two cases as Figure 61. The differences between the two traces are less than the uncertainty of the measurement.

4.4.5 Effect of Laser Target Material

Previous experiments have been conducted on the effect of using different materials for the laser target in electrode-focused laser triggered switches [71] [75]. However, since the absorption properties of materials at 1500 nm can differ significantly from shorter wavelengths, it was decided that experimental verification was necessary. As described in section 4.2.2, the initial experiments were conducted using graphite. Graphite can be a good spark gap electrode material with long lifetime and consistent breakdown properties if the appropriate grade is used [76]. However, it is also popular to fashion spark gap electrodes from refractory metals and their alloys to reduce the erosion rate. A very common electrode material is tungsten-copper (W-Cu). This material is not an alloy of the two metals but is best described as a tungsten matrix impregnated with copper [77]. This material is readily available with tungsten percentages between 50% and 90%. The tungsten provides resistance to spark erosion due to its extremely high melting and vaporization temperatures, while the copper increases electrical and thermal conductivity as well as improving machinability. Common grades for use as spark gap electrodes are generally between 60% and 80% tungsten. For these experiments, a 68% tungsten grade was chosen.

Plots comparing the run time and jitter for runs conducted with each of the materials are shown in Figure 63 through Figure 66. In the case where the target was the cathode, the data is very consistent and there is no apparent difference between the W-Cu insert data and the graphite insert data. The data for the anode target case shows significantly more spread, but no general dependency on insert material is apparent. The spread of the anode target data is consistent with other experiments conducted in this setup. The anode target configuration seems to be very sensitive and often shows significant spread from one test to the next. The similarity between the two materials extended to the self-break and minimum trigger voltage measurements. One observation made during these experiments was that the W-Cu target seemed to suffer less damage from both the discharge and laser, which led to its use as the preferred target material for most of the remaining experiments described in this chapter.

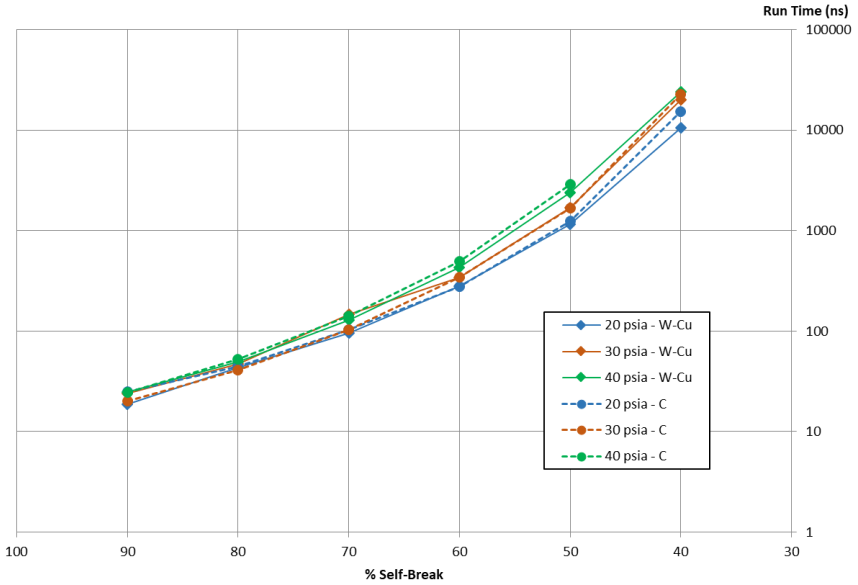

Figure 63 - Plot comparing the run times for the W-Cu laser target insert with the graphite target insert for the cathode target polarity. The results overlap to such an extent that no dependence on target material can be determined.

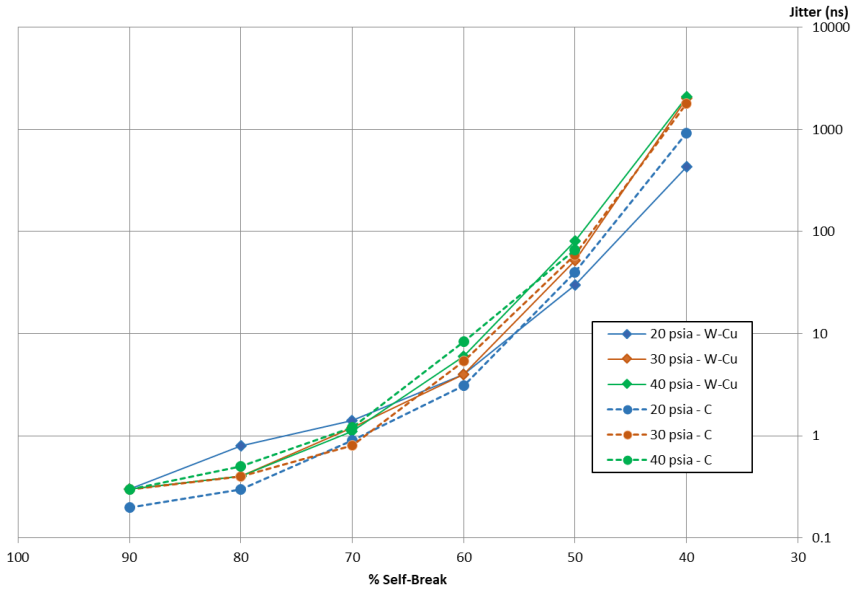

Figure 64 - Plot comparing the run time jitter for the W-Cu laser target insert with the graphite target insert for the cathode target polarity. No dependence on material is apparent.

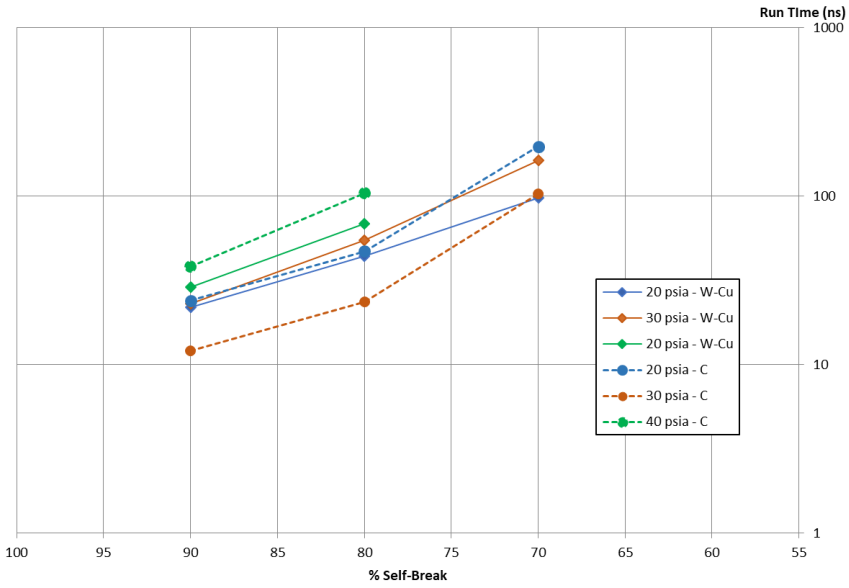

Figure 65 - Plot comparing the run times for the W-Cu laser target insert with the graphite target insert for the anode target polarity. There is much more spread to the data than for the cathode target case, but there appears to be no consistent material dependence.

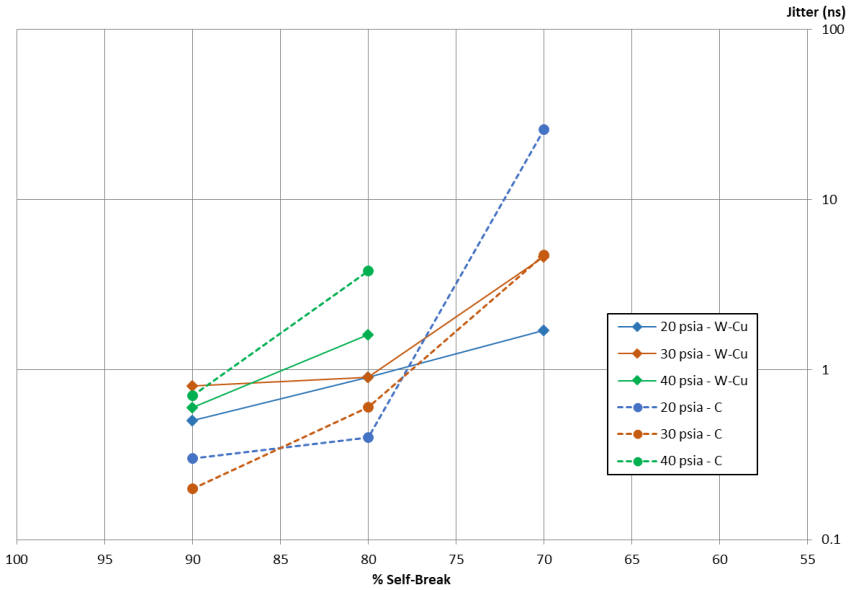

Figure 66 - Plot comparing the run time jitter for the W-Cu laser target insert with the graphite target insert for the anode target polarity. This data also shows a random spread that does not imply any material dependence.

4.5 Determining Minimum Necessary Laser Energy

4.5.1 Motivation

Initially, it was thought that the output of the ER-902 laser, approximately 250 μJ, would be barely sufficient to initiate switching in a pressurized gas switch since previous experiments generally used at least an order of magnitude more laser energy [74] [78]. However, the excellent preliminary results described above encouraged investigation into the effect of reducing the laser energy, with the goal of finding the minimum necessary laser energy and the performance trade-offs of operating at lower energy. Reducing the laser energy required to trigger a switch would have multiple benefits in the employment of this technology in a compact pulsed power system. Lower energy lasers are generally less expensive and more compact. Lower energy requirements per switch increase the number of switches that can be triggered with a single laser of a given energy level. If the laser energy can be reduced to a low enough level, it opens the possibility of transporting the beam from the laser to the switch using optical fibers with commensurate benefits in system design flexibility [79] [80].

4.5.2 Setup Modifications

The basic setup from the initial experiments described in section 4.2 was retained for this set of experiments with the addition of a holder for the neutral density (ND) filters that were used to attenuate the laser energy. These were placed between the beam expander and the switch as shown in Figure 67. The switch was fitted with a W-Cu laser target insert. Nitrogen at 30 psia was used as the switch fill gas for all experiments. A single pressure was used to reduce the total number of shots. The gap distance was maintained at 3.4 +/- 0.1 mm for these experiments.

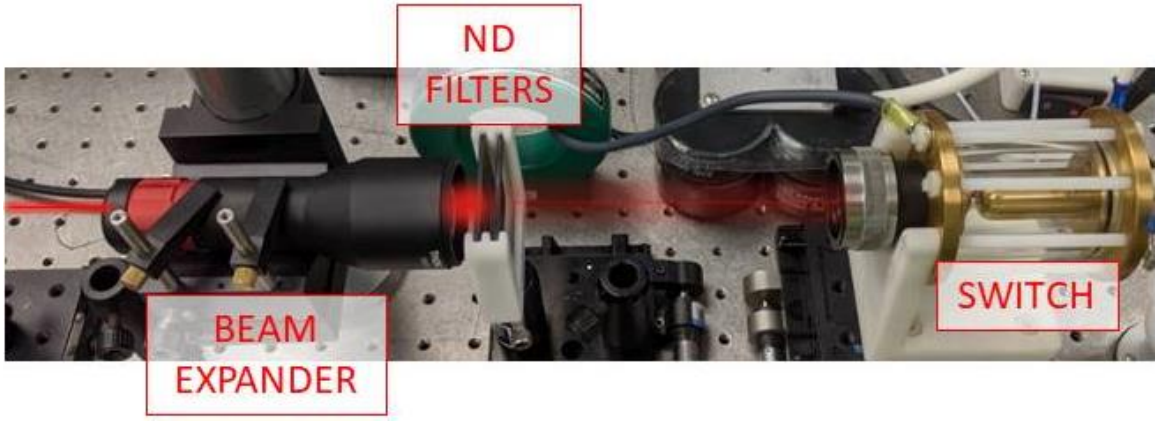

Figure 67 - Labeled photograph of the reduced laser energy experiment optical system with an overlaid illustration of the laser beam path.

4.5.3 Calibration of ND Filters

The ND filters employed to attenuate the laser pulse for this series of experiments are nominally calibrated in the visible spectrum and this calibration is not valid at the experimental wavelength of 1535 nm. The actual transmitted energy at 1535 nm was measured for each filter using a pyroelectric laser energy sensor – Ophir Photonics model PE25-C. An average of the transmitted energy for 100 shots was calculated for each filter (or combination of filters) that was used in the experiment. The measured average energy and variance is given in Table 4. The deviations are primarily attributed to the noise level of the sensor. The no filter case has higher deviation because those shots had to be recorded on the 2 mJ range of the sensor, instead of the 200 µJ range used for the remaining shots. The sensor has a stated calibration error range of +/- 3%. Reliably attenuating and measuring the laser below the 8.28 µJ level proved impossible with the equipment on hand.

Table 4
ND Filter Calibration Data

Filter	Average Energy (μJ)	Standard Dev. (μJ)
No Filter	228	2
ND 0.1	198	1
ND 0.2	118	1
ND 0.3	99.9	0.4
ND 0.5	78.8	0.4
ND 0.6	50.0	0.4
ND 0.7	40.7	0.3
ND 0.7+0.2	20.6	0.3
ND 0.9+0.5	12.4	0.3
ND 1.0+0.6	8.28	0.30

4.5.4 Results from Reduced Laser Energy Sweeps

The experiments conducted with reduced laser energy produced surprising results. As shown in Table 5, the minimum trigger voltage increases with decreasing laser energy for both polarities. In the anode target polarity, the switch could be triggered with 100% reliability with as little as 78.8 μJ of laser energy. At 50 μJ, triggering was still possible, but was not 100% reliable at 90% of self-break. As with previous experiments, the cathode target polarity showed greater range than the anode target polarity. The ability to trigger with only 8.28 μJ of laser energy was unexpected. Below approximately 50 μJ the laser plasma is no longer visible on the target insert. However, if the laser spot is on the order of 10^{-10} m^2 as was estimated in section 4.2.5, then the irradiance is still on the order of 10^{13} W/m^2, which is well above the threshold for nanosecond laser induced plasma formation as described by Rai and Thakur in [72].

Table 5
Reduced Laser Energy Minimum Trigger Voltage

Average Laser Energy (μJ)	Anode Target Minimum Trigger (kV)	Anode Target Minimum Trigger (%SB)	Cathode Target Minimum Trigger (kV)	Cathode Target Minimum Trigger (%SB)
228	14.5	66%	8.5	38%
198	15.0	68%	8.7	39%
118	16.0	72%	9.2	42%
99.9	16.6	75%	10.0	45%
78.8	17.6	80%	10.6	48%
50.0	N/A	N/A	11.1	50%
40.7	N/A	N/A	12.7	57%
20.6	N/A	N/A	12.8	58%
12.4	N/A	N/A	13.0	59%
8.28	N/A	N/A	17.0	77%

4.5.4.1 Anode Target Reduced Energy Runs

Run time and jitter data was recorded as a function of charge voltage for each of the laser energy levels down to 50 μJ for the anode target case. These results have been plotted as a function of charge voltage expressed in percent self-break in Figure 68 and Figure 69. The results show that the run time and jitter are weakly dependent on the laser energy when the charge voltage is much higher than the minimum trigger voltage, but that the run time and the jitter diverge significantly once the charge voltage approaches the minimum trigger for each laser energy. It is interesting to note that the threshold for run time in this polarity is approximately 100 ns. This is a consistent result for this polarity across all of the tests except for the test in nitrogen and a 1.3 mm gap, where the threshold was around 10 ns. This is in contrast to the cathode target polarity, which shows no distinct run time threshold. The results for the anode target polarity were also analyzed and plotted as a function of laser energy as shown in Figure 70 and Figure 71. This more clearly shows that the effect on run time of reducing the laser energy only appears to be significant near the lower limits of operation. It is also clear that the jitter is more strongly dependent on laser energy than run time.

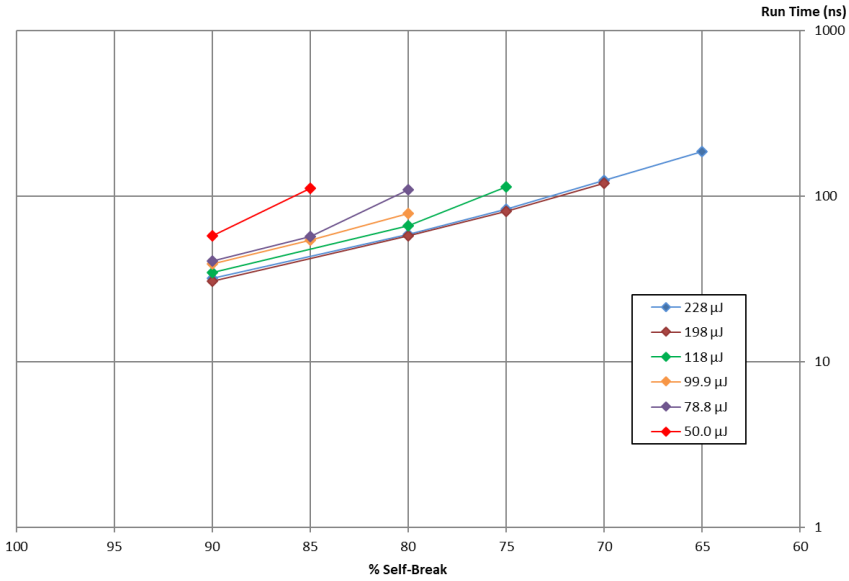

Figure 68 - Plot of the switch run time vs. percent of self-break voltage at various values of average laser pulse energy in the anode target polarity. Note that there is not a large change in run time over a factor of three in laser energy. The 50 µJ case represents a threshold case where triggering was not 100% reliable.

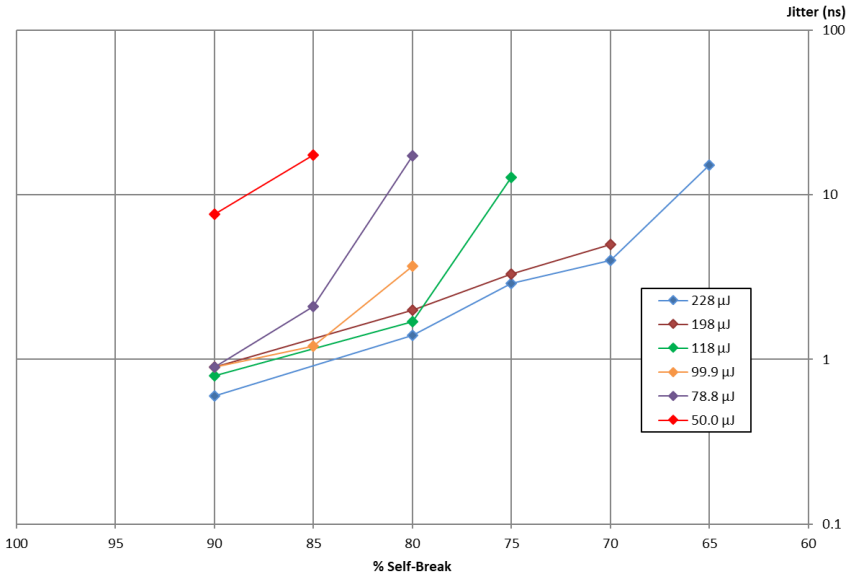

Figure 69 - Plot of the switch run time 1-σ jitter vs. percent of self-break voltage at various values of average laser pulse energy in the anode target polarity.

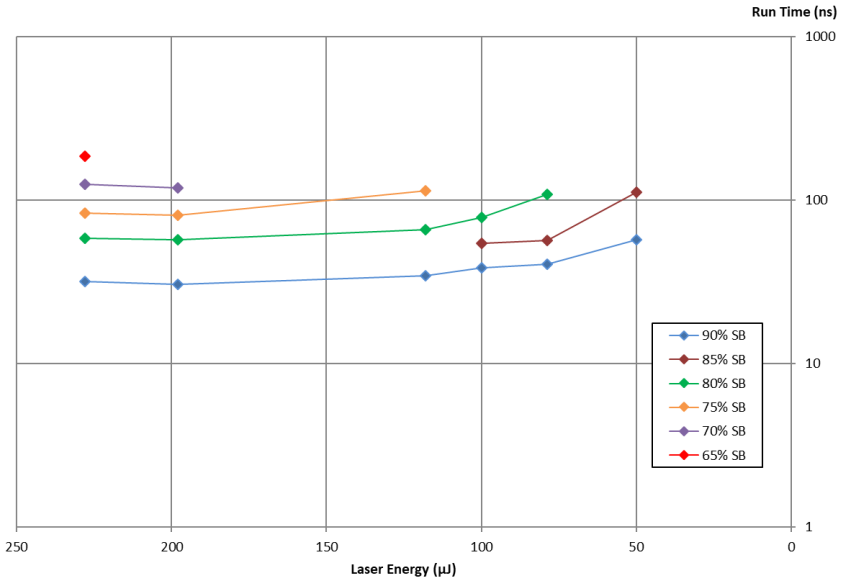

Figure 70 - Plot of the switch run time vs. laser pulse energy for different values of self-break percentage in the anode target polarity. This plot shows that there is little dependence on laser energy until the lowest energies are reached, and then the run time increases slightly with decreasing energy.

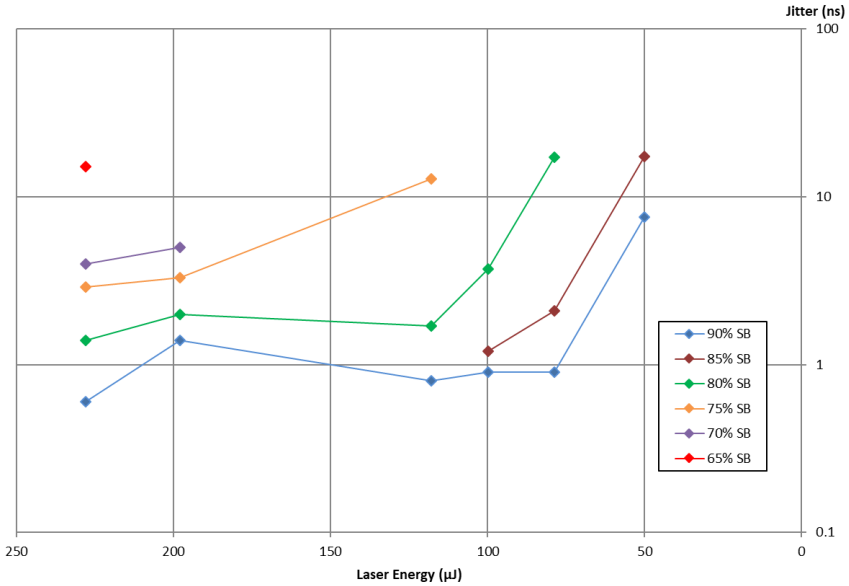

Figure 71 - Plot of the switch run time jitter vs. laser pulse energy for different values of self-break percentage in the anode target polarity. Note the distinct increase in jitter for the lowest laser energy settings at the higher percentages of self-break.

4.5.4.2 Cathode Target Reduced Energy Runs

Run time and jitter data was recorded as a function of charge voltage for all of the available laser energy levels for the cathode target polarity. Figure 72 and Figure 73 provide plots of this data as a function of charge voltage expressed in percentage of self-break voltage. As with the anode target polarity, there is a weak dependence of both run time and jitter on laser energy and some evidence of increasing dependence when the charge voltage approaches the minimum trigger voltage. However, this increase is not as severe for the cathode target polarity. This is consistent with the other experiments conducted in this polarity where the operation of the switch seems to be robust even as the run times become very large. Plotting the run time and jitter as a function of laser energy for the cathode target polarity results in Figure 74 and Figure 75 produces almost horizontal lines – illustrating the very small dependence on laser energy.

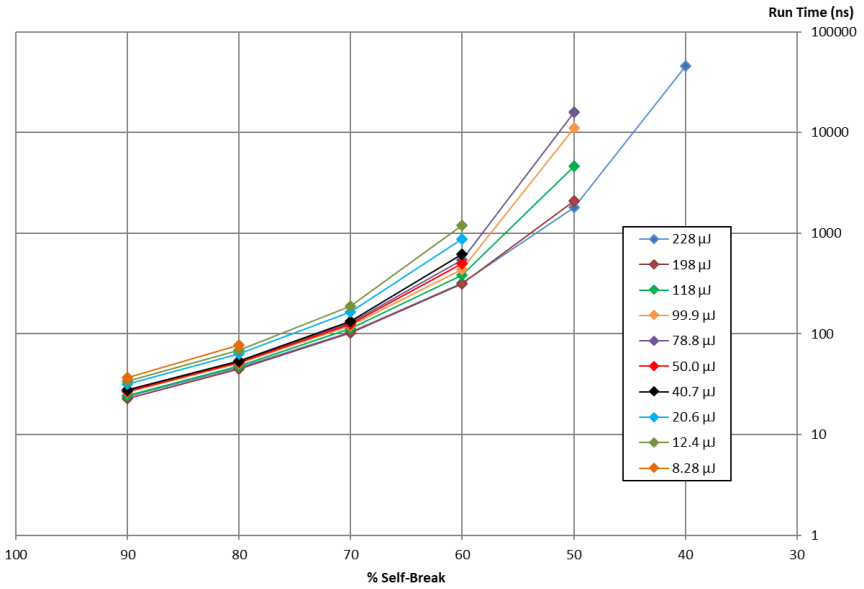

Figure 72 - Plot of the switch run time vs. percent of self-break voltage at various values of average laser pulse energy in the cathode target polarity. Laser energy has little effect on run time, but at lower laser energies the minimum percentage of self-break for reliable triggering increases.

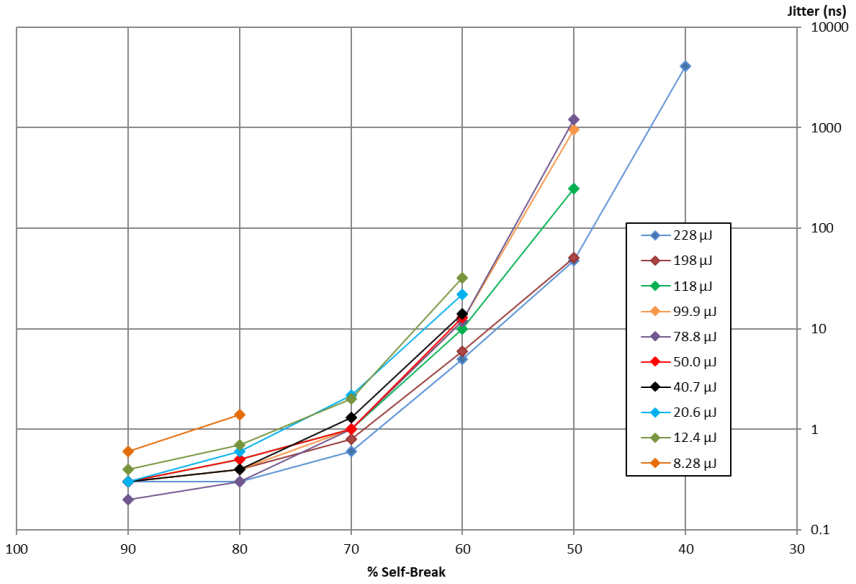

Figure 73 - Plot of the switch run time 1-σ jitter vs. percent of self-break voltage at various values of average laser pulse energy in the cathode target polarity. Jitter follows the same trends as run time.

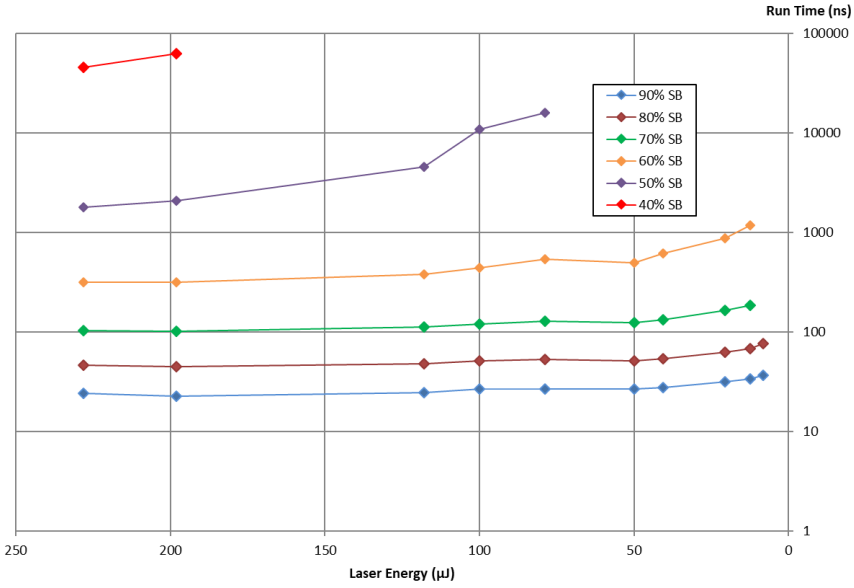

Figure 74 - Plot of the switch run time vs. laser pulse energy for different values of charge in the cathode target polarity. There is little dependence on laser energy until the lowest energies are reached, and then the run time increases slightly with decreasing energy.

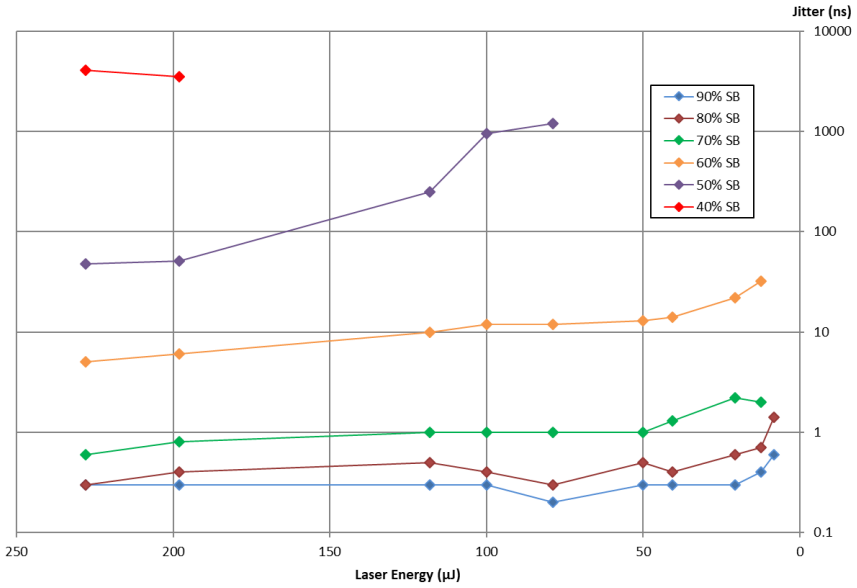

Figure 75 - Plot of the switch run time jitter vs. laser pulse energy for different values of self-break percentage in the cathode target polarity. Jitter shows slightly more dependence on energy compared to run time.

4.6 Experiments in Gasses Other Than Nitrogen

4.6.1 Motivation

Nitrogen was used for the majority of the experiments in this chapter since it was readily available and is a commonly used gas for the switching medium in pressurized spark gaps. However, other gasses are sometimes preferred for a variety of reasons. While the dielectric strength of air is approximately the same as pure nitrogen, some practitioners prefer it due to the slightly different properties imparted by the presence of oxygen, which is significantly more electronegative than nitrogen and has a lower first molecular ionization potential [81]. In cases where the highest dielectric strength is needed, sulfur hexafluoride (SF6) is a popular gas despite its higher cost.

Research in the field of laser induced breakdown spectroscopy revealed that differences in background gas can have significant effects on the properties of the plasma produced by laser interaction with a solid surface [72]. Since this plasma is thought to be an important part of the triggering process in the switch under

investigation, experiments were conducted using the aforementioned gasses to ascertain any differences in switch behavior.

4.6.2 Setup Modifications

Aside from the gas used to fill the switch, the experimental setup was the same as described in section 4.2 with the exception that W-Cu laser target inserts were used instead of graphite.

4.6.3 Synthetic Air Experiments

The ready availability of air and the large body of research on its electrical breakdown properties makes it a gas commonly used in spark gap switches. The use of air in spark gaps is generally preferred by some pulsed power engineers either due to familiarity or due to the electronegative properties of oxygen which make corona stabilization possible [82]. Atmospheric air is widely used – often with some attempt made at filtering and drying when it is compressed. This is due to the detrimental effects of moisture and hydrocarbon impurities on the electrical properties [83] and the longevity of the switch components. One way to avoid the uncertainty of the composition of atmospheric air is to use synthetic air, which is a mixture of nitrogen and oxygen obtained by the fractional distillation of liquified atmospheric air. One common grade is Ultra Zero (UZ) air, which is a mixture of 20 to 22% oxygen with the balance of nitrogen and is specified to contain less than 2 ppm water and 0.1 ppm hydrocarbons [84].

The experiments conducted with the micro-laser made use of UZ air and a spark gap length of 3.6 mm. Measurements of self-break voltage, minimum trigger voltage, run time, and jitter were made at three pressures in both the anode target polarity and cathode target polarity. Control tests were also performed using nitrogen gas with the same gap and at the same pressures. Self-break and minimum trigger values are listed in Table 6.

Table 6
UZ Air vs. N2 Self-Break and Minimum Trigger Voltages

Cathode Target Polarity – UZ Air			
Pressure (psia)	Self-Break (kV)	Minimum Trigger (kV)	Minimum Trigger (%SB)
20	15.6	7.1	46%
30	22.4	12.2	54%
40	29.2	18.4	63%
Cathode Target Polarity – N2			
Pressure (psia)	Self-Break (kV)	Minimum Trigger (kV)	Minimum Trigger (%SB)
20	16.6	5.9	36%
30	23.6	8.6	36%
40	30.2	11.9	39%
Anode Target Polarity – UZ Air			
Pressure (psia)	Self-Break (kV)	Minimum Trigger (kV)	Minimum Trigger (%SB)
20	15.7	8.7	55%
30	22.4	14.0	63%
40	29.4	19.1	65%
Anode Target Polarity – N2			
Pressure (psia)	Self-Break (kV)	Minimum Trigger (kV)	Minimum Trigger (%SB)
20	16.6	9.5	57%
30	23.7	15.7	66%
40	30.4	21.8	72%

These results show that the use of air as a switching medium has a significant impact on the laser-triggered breakdown process when compared to nitrogen. The greatest impact is that the air shows very little difference in triggering range between the cathode target and anode target polarities, whereas the nitrogen shows significant difference between the two polarities. The roughly 1 kV reduction in self-break voltage between the nitrogen and UZ air is expected due to the slightly lower dielectric strength of air [83].

The run time and jitter data obtained from the experiments with air also show significant differences between the behavior in the UZ air and the baseline experiments in nitrogen. Figure 76 through Figure 79 provide plots of the run time and jitter data for the UZ air and the nitrogen tests. In the anode target polarity, the differences between the UZ air and nitrogen are minimal and do not seem to follow any particular pattern. However, in the cathode target polarity, the UZ air data shows a very large pressure dependence that is not seen in the nitrogen data. Below 80% of self-break the UZ air shows run times and jitters between 1 and 2 orders of magnitude larger than the nitrogen control data.

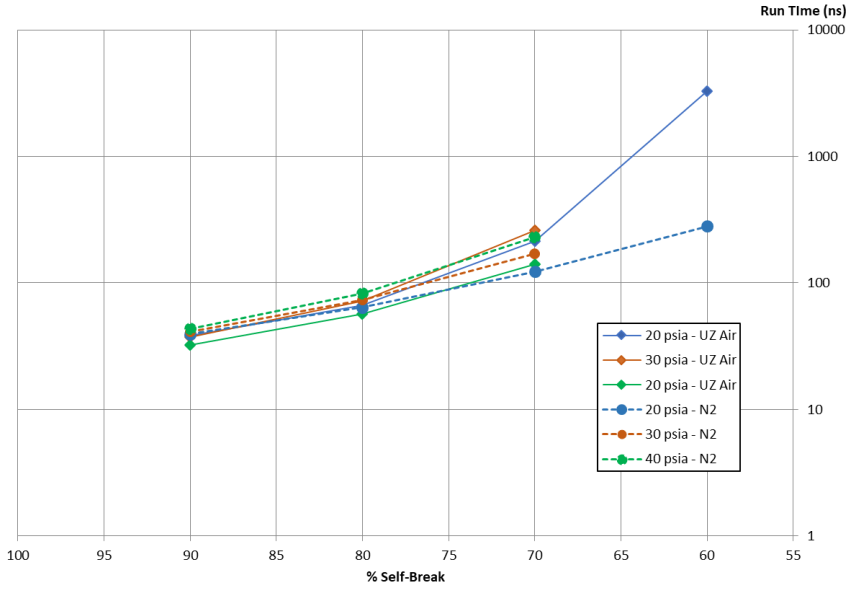

Figure 76 - Plot comparing the run times of the switch as a function of percent of self-break voltage for the anode target polarity in UZ air and N2. The run times are very similar between the two gasses except for the difference for the N2 at 20 psia – which is not understood.

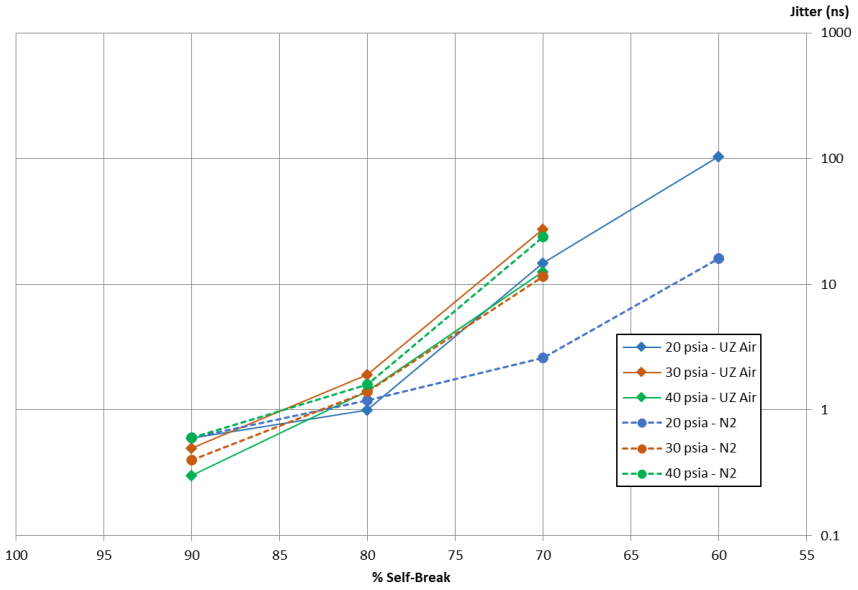

Figure 77 - Plot comparing the run time jitter of the switch as a function of percent of self-break voltage for the anode target polarity in UZ air and N2. The jitter follows the same trends as the run times.

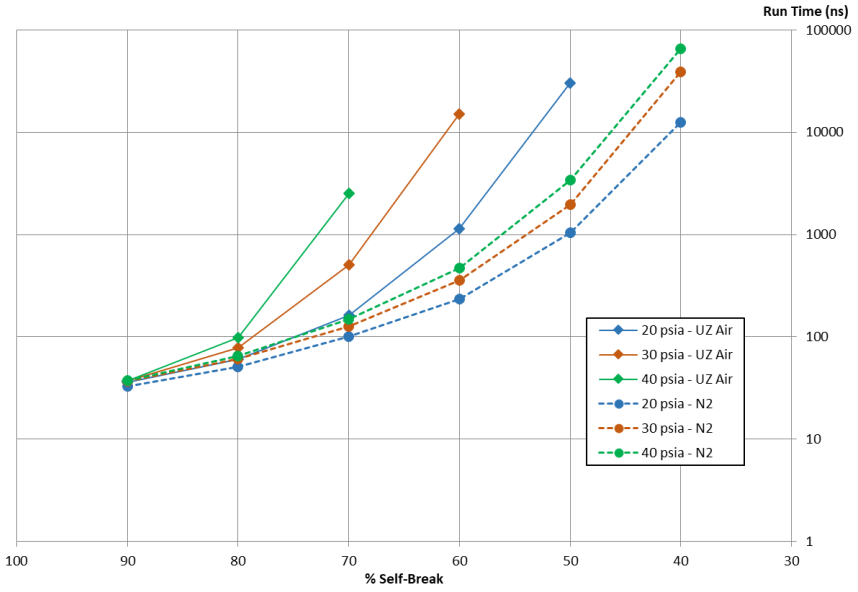

Figure 78 - Plot comparing the run times of the switch as a function of percent of self-break voltage for the cathode target polarity in UZ air and N2. The N2 data is as expected, but the run times for the UZ air are much higher and show a significant pressure dependence at lower percentages of self-break.

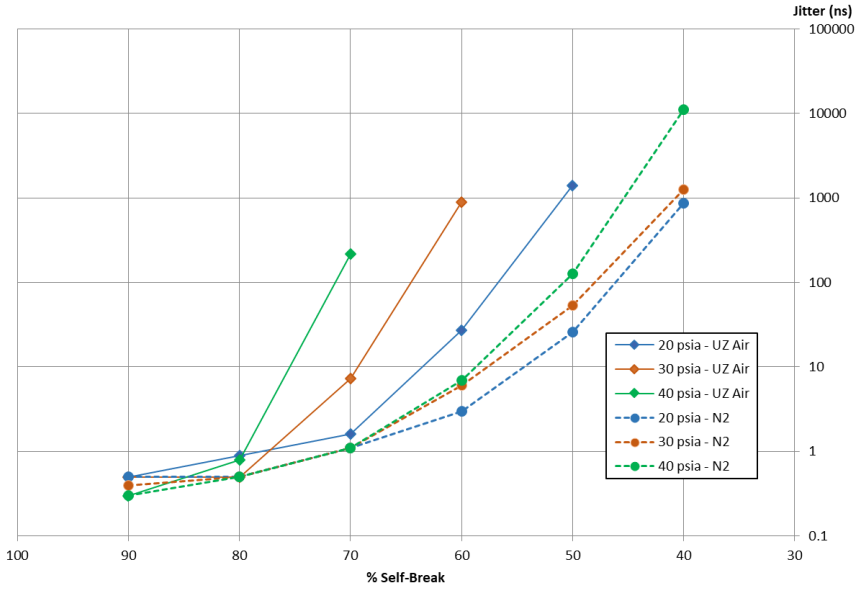

Figure 79 - Plot comparing the run time jitter of the switch as a function of percent of self-break voltage for the cathode target polarity in UZ air and N2. The jitter follows the same trends as the run times.

4.6.4 Sulfur Hexafluoride Experiments

SF6 has been a common insulating gas in pulsed power systems from the beginning of the field. The two principal advantages of SF6 over air or nitrogen are its high breakdown field strength [83] and its high heat capacity [81] (both approximately 3 times nitrogen). The high heat capacity permits the SF6 to absorb more heat from an arc for a given temperature rise. This effect is more important in power industry uses of SF6 than in pulsed power systems. The high breakdown strength permits the use of higher electric fields in devices and – in the case of switches – smaller gaps for a given voltage. This leads to reduced arc channel inductance. The greater dielectric strength of SF6 is due to the very high electronegativity imparted by the six fluorine atoms on each molecule, which capture free electrons and form relatively low-mobility negative ions. SF6 is commonly used in laser-triggered spark gaps for large pulsed power machines where the strong absorption and low ionization potential of SF6 for UV light is exploited to generate the laser plasma in the middle of the spark gap. This has been shown to produce very low jitter switching [65] [85]. However, this requires a UV laser – either a

krypton-fluoride laser or a frequency-quadrupled Nd:YAG laser – with several millijoules of pulse energy. These are large, expensive lasers.

The experiments using SF6 in the micro-laser triggered switch setup were conducted using a 1.3 mm gap in order to permit the collection of data at multiple pressures while remaining under the 35 kV limit of the test system. Measurements of self-break voltage, minimum trigger voltage, run time, and jitter were made at three pressures in the anode target polarity and four pressures in the cathode target polarity. Self-break and minimum trigger values are listed in Table 7.

Table 7
SF6 Self-Break and Minimum Trigger Voltages

Cathode Target Polarity			
Pressure (psia)	Self-Break (kV)	Minimum Trigger (kV)	Minimum Trigger (%SB)
20	16.9	12.3	73%
25	21.5	14.4	67%
30	25.7	17.6	68%
35	30.1	20.9	69%
Anode Target Polarity			
Pressure (psia)	Self-Break (kV)	Minimum Trigger (kV)	Minimum Trigger (%SB)
20	16.8	12.3	73%
25	19.4	14.8	76%
30	22.2	17.9	81%

These results show that the SF6 has a significant impact on the laser-triggered breakdown process when compared to nitrogen. The greatest impact is that the SF6 shows very poor triggering range with little difference between the cathode target and anode target polarities. In order to discount the possibility that the laser was being absorbed by the SF6, a measurement of transmitted energy was made through a test cell filled first with air and then with SF6. No additional absorption was measured for the SF6. The setup used for these measurements was the same as that used for the oil absorption experiments described in section 4.8.

The run time and jitter data obtained from the experiments with SF6 also show significant differences between the behavior in this gas and the baseline experiments in nitrogen. Figure 80 through Figure 83 provide plots of the run time and jitter data. The most significant difference is that the run times and jitter are two to three orders of magnitude higher for SF6 compared to nitrogen at the same percentage of self-break, despite the fact that the gap was smaller in the SF6 experiments. A very significant pressure dependence on the run time was noted for the anode target polarity, but this was not the case in the cathode target polarity. Another interesting observation was the pronounced saturation of run time and jitter at lower percentages of self-break – i.e. the rate of increase of these parameters slows significantly as the minimum trigger voltage is approached. This is in direct contrast to the nitrogen data where the rate of increase was continuously increasing as the minimum trigger voltage was approached.

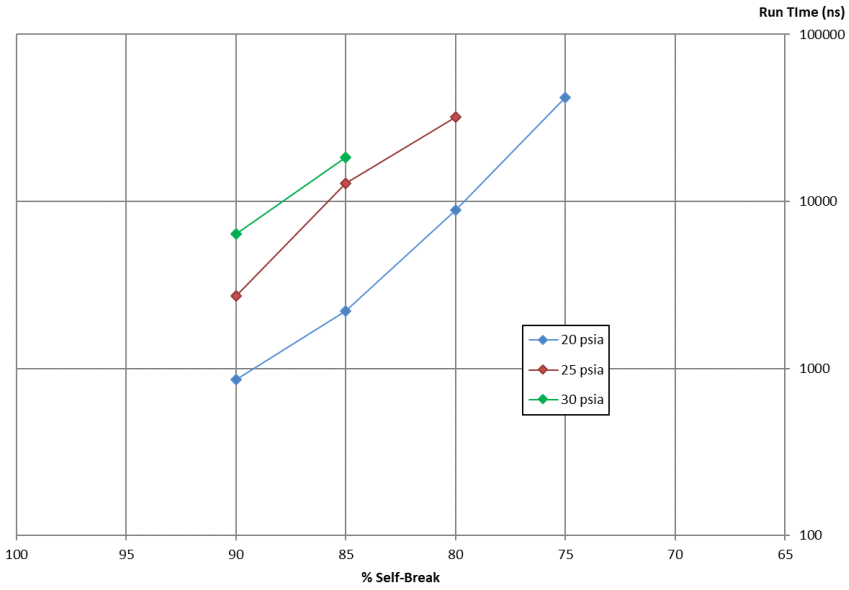

Figure 80 - Plot of the run times of the switch as a function of percent of self-break voltage for the anode target polarity in SF6. The gap was set at 1.3 mm. Note that the run times are two to three orders of magnitude greater than for N2.

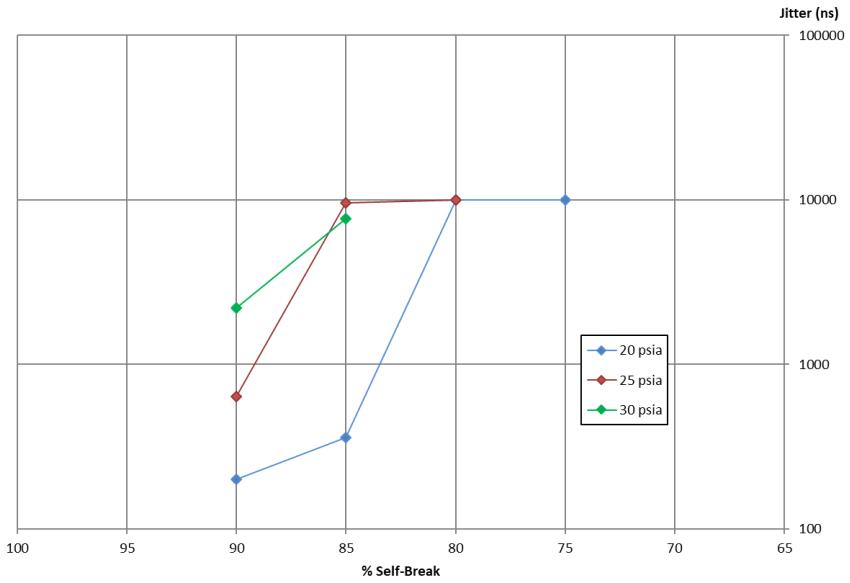

Figure 81 - Plot of the run time jitter of the switch as a function of percent of self-break voltage for the anode target polarity in SF6.

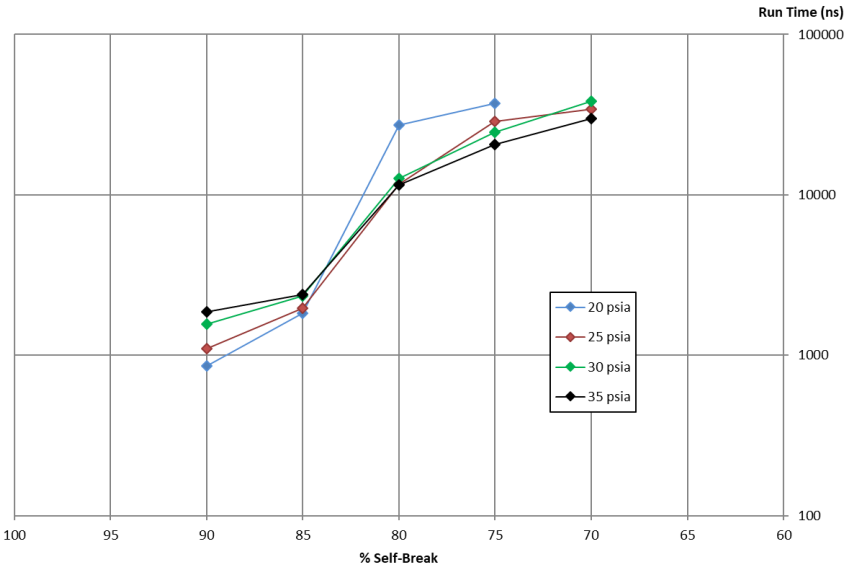

Figure 82 - Plot of the run times of the switch as a function of percent of self-break voltage for the cathode target polarity in SF6. The run times are of the same order as those in the anode target polarity. In SF6, the cathode target polarity results only slightly improved triggering range. Also note the saturation-like behavior at lower percentages of self-break.

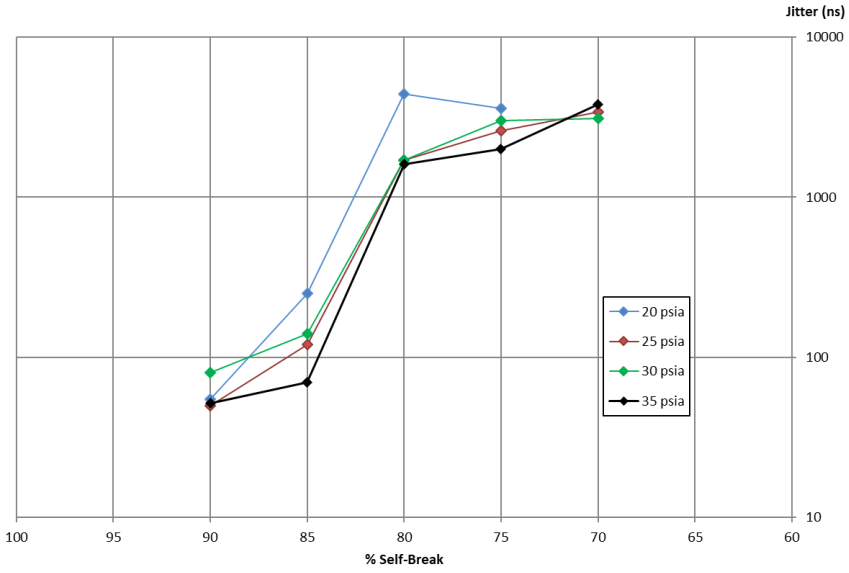

Figure 83 - Plot of the run time jitter of the switch as a function of percent of self-break voltage for the cathode target polarity in SF6.

4.6.5 Discussion of Results for Alternative Gasses

The results obtained from these experiments provide insight into a potential theory of the development of the breakdown from the effects of the laser-induced plasma and the source of the polarity asymmetry observed in the baseline tests in nitrogen. It appears that the large number of free electrons – estimated to be on the order of 10^9 to 10^{12} – produced by the laser plasma have the ability to enhance the discharge formation process in the cathode target case, but only if they are not inhibited by attachment to electronegative gas molecules.

The large increase in run time for the SF6 experiments is more difficult to explain. T.H. Martin proposed a formulation for the run time of any gas based on heating effects [27]. His result, which was successfully used in the spark gap model described in Chapter 2, is given as a function of electric field E and gas density ρ:

$$t_{runtime} = 98{,}700 \times \frac{\rho^{2.44}}{E^{3.44}} \tag{23}$$

This equation shows that increasing the density of the gas will increase the run time. Given that SF6 is almost six times denser than nitrogen, this could explain the run time difference. To determine if this is the case, the theoretical run times of the SF6

experiment and the nitrogen control in section 4.6.3 were compared. The data is plotted in Figure 84.

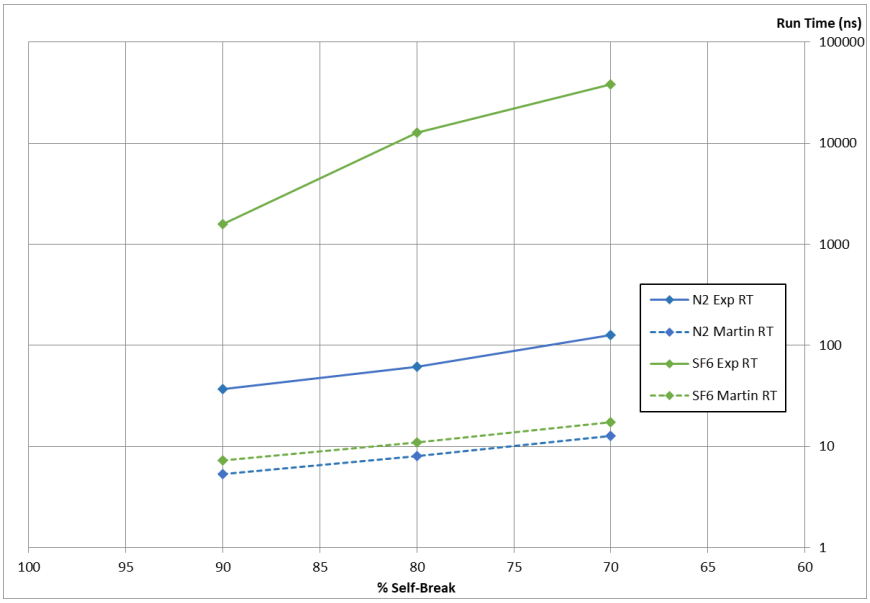

Figure 84 - Plot of experimental and theoretical run times for N2 and SF6 at 30 psia in the cathode target polarity. Note that the Martin run time equation does not predict the very large difference between the N2 and SF6 run times.

This plot shows that the Martin equation does not predict the very large difference in run times. The results are similar for other pressures and the anode target polarity. Thus, some other mechanism must be contributing to the extremely long run times measured for the SF6.

4.7 Laser Target Electrode Damage Effects

4.7.1 Motivation

A common concern regarding the triggering of a switch with a laser focused on an electrode surface is the damage done to the electrode by the laser and the effect of this damage on the reliability of the switch. This concern was particularly relevant for early experiments in laser triggering that made use of 100's of mJ to Joule levels of laser energy. While the energy of the present laser is orders of magnitude less than this, the preliminary experiments did show that a small hole was drilled into the target by the

laser over the course of many shots. Qualitatively, it appeared that several thousand shots produced enough of a hole that the laser focus was affected sufficiently to produce visible differences in the laser plasma plume size. Based on this observation, a series of experiments were developed to quantitatively investigate the behavior of this switch over a large number of shots with parameters relevant to a compact pulsed power system.

4.7.2 Scope

The electrode damage experiments were designed to develop some understanding of the behavior of the micro-laser triggered switch. They were not intended to constitute a program of lifetime or reliability testing. In addition to the effect of the laser on the electrode, the combined effects of the laser and the discharge arc are thought to be important in determining the lifetime of this type of switch.

4.7.3 Experimental Methodology

The methodology of the experiment sought to examine the laser and arc damage effects individually and collectively. This was accomplished by preparing three electrodes with new laser target inserts that were made as identical as possible. This included matching the overall length of the electrodes precisely (to +/- 0.03 mm) such that the laser focus would be identical between experiments. The three electrode and target insert assemblies were then each subjected to a different test with the remainder of the switch hardware unchanged. The first electrode assembly was subjected to 1000 shots of the laser at its maximum repetition rate of 10 Hz. This rate was used for all of the lifetime tests to produce the maximum stress on the electrode and more closely mimic the operating conditions that would be experienced by a switch in a compact pulsed power application. The second electrode assembly was subjected to 1000 shots of laser triggered switching of a 60 nF capacitor charged to 30 kV and discharging through a 5 Ω load. The peak current was limited to 4 kA by the load resistance and circuit inductance. These values were chosen based on available components and a desire to achieve a discharge in the kA range and 10's of J of energy since this is a relevant parameter range

for a compact pulsed power system. The third electrode assembly was then operated with the same discharge parameters until the laser no longer produced reliable triggering of the switch. These experiments were carried out for two laser target materials – commercial graphite and W-Cu. These materials and the reasons for using them for the laser targets were described in sections 4.2.2 and 4.4.5. Electrode preparation was performed in the same manner as described in section 4.2.2.

4.7.4 Setup Modifications

The electrical configuration of the test setup was altered significantly for this experiment while the optical configuration remained the same. The ceramic capacitor was replaced with a plastic-case Maxwell film capacitor rated for 75 kV and 60 nF. A low-inductance load was fabricated from a stack of five 1 Ω ceramic resistors in series. The capacitor was charged using a TDK-Lambda model 202A capacitor charging power supply that provides constant-current charging at approximately 100 mA. These changes were made to permit operation of the switch at the desired 10 Hz repetition rate and kA discharge current with a charge voltage of 30 kV. The energy per shot was 27 J and the peak current was 4 kA with a 10%-90% rise time of 90 ns. The current pulse had a FWHM of 370 ns. Figure 85 provides an image of the electrical components used in these experiments.

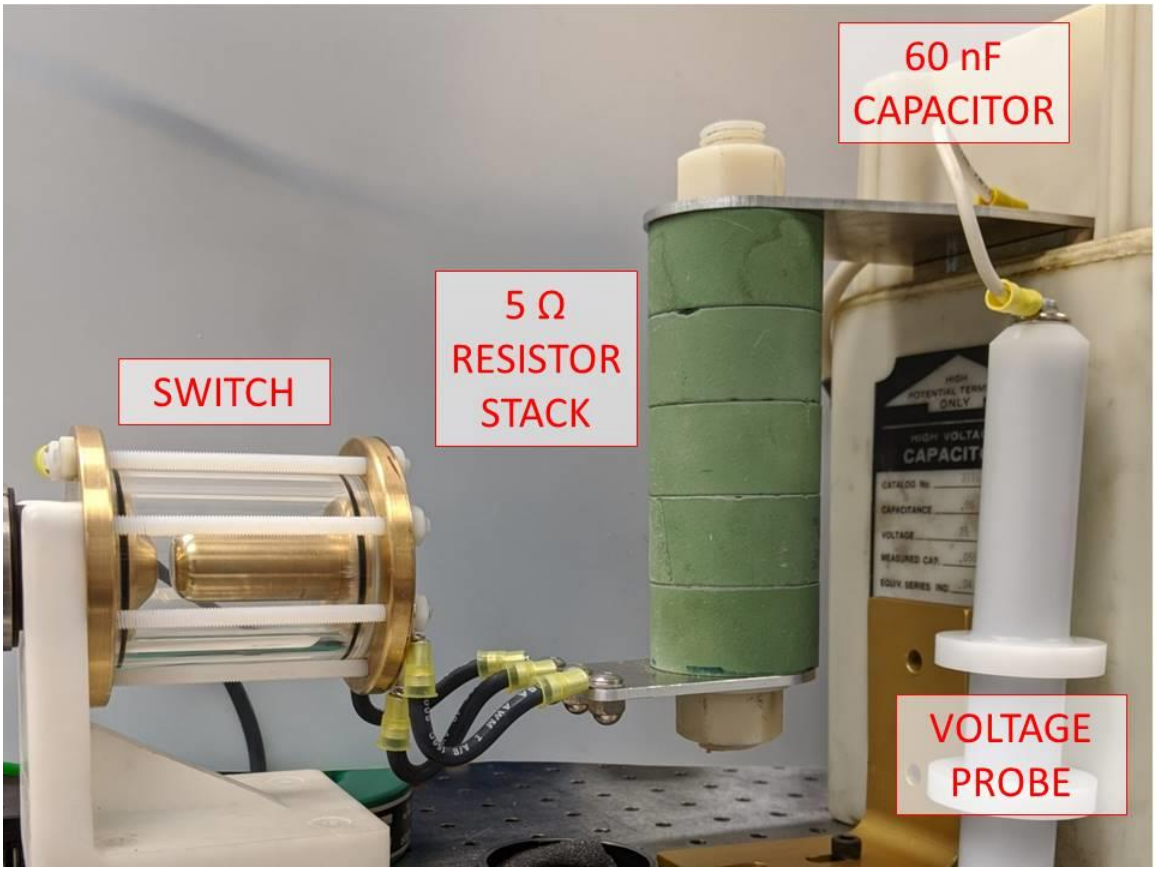

Figure 85 - Labeled photograph of the high-current electrode damage test setup.

4.7.5 Graphite Laser Target Insert Damage

The following sections describe the observations made during and after testing the three graphite laser target inserts.

4.7.5.1 Damage Due to Laser Alone

The first graphite laser target insert was tested using only the laser, with a switch charge voltage of zero. The switch was filled with atmospheric pressure (12.1 psia or 84 kPa in Albuquerque) air. Photographs taken before and after the shot through an optical microscope are shown in Figure 86. The laser damage appears as a small, well-defined hole surrounded by a light-colored region which is itself surrounded by a ring that is somewhat darker than the material outside the affected area. The diameters of these

three features are estimated to be 25 µm, 250 µm, and 400 µm respectively by scaling from the known diameter of the target insert.

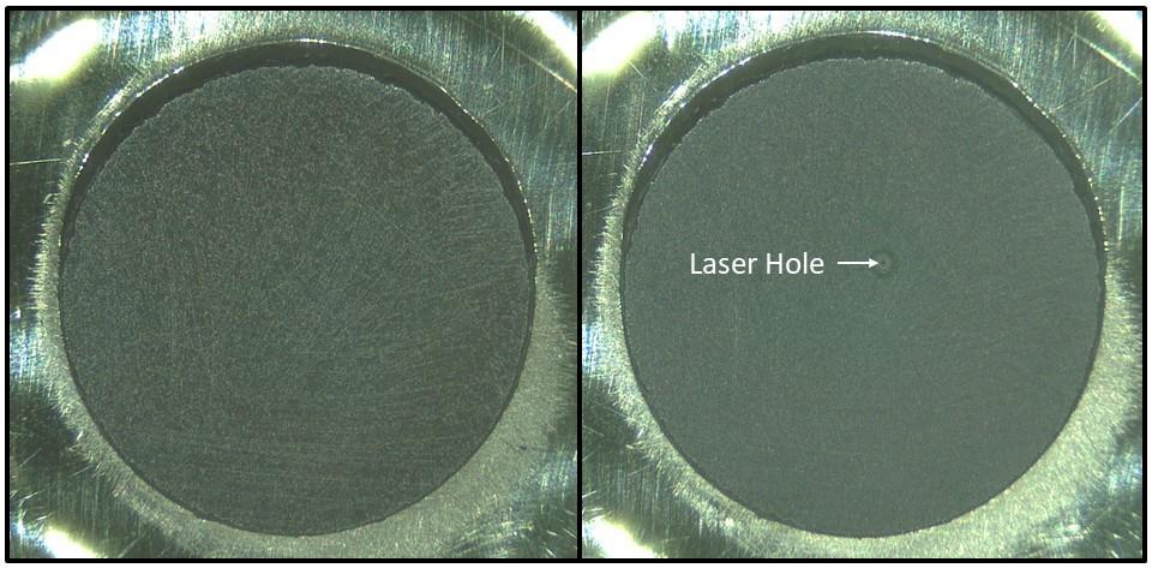

Figure 86 - Micro-photographic comparison of graphite target number one before and after 1000 shots of the laser at 10 Hz. The laser hole and surrounding discoloration are easily discernable. The slight difference in appearance of the bulk of the insert is due to lighting differences between the two photos.

4.7.5.2 Combined Damage Due to Laser and High Current Discharge

The second graphite laser target insert was installed in the switch after the laser-only test was conducted on the first insert. The laser focus was not adjusted – the precise matching of the lengths of the first and second electrodes was sufficient to ensure that the laser focus remained the same. The switch was operated at 45 psig (approximately 57 psia or 393 kPa). This pressure was chosen based on scaling from the previous self-break data such that 30 kV would be approximately 80% of the self-break voltage. The 1000 shot run was conducted without any prior conditioning of the electrode. The run resulted in 998 data captures, of which 983 were good shots where the switch closed within the data acquisition window of 1.6 µs. It is believed that the 2 missing captures are due to glitches in the delay generator that resulted in failure to trigger the charge-fire sequence. The 15 shots where the switch did not discharge are thought to be the result of pre-fires where the switch broke down before arrival of the laser pulse, thus

leaving the capacitor discharged at the time of the laser pulse. These pre-fires are clearly audible during operation of the switch, and it is believed that they are due to particles of electrode material remaining in the gap between shots. This could be reduced by flowing gas through the switch during operation, but that was not tested during these experiments. The average switch run time was 98 ns with a 1-σ jitter of 8 ns. Figure 87 is a screen capture from the oscilloscope showing an overlay of all of the shots.

Figure 87 - Screen capture of the 1000 shots taken with the second graphite laser target insert.

One behavior that was seen in this run that was not readily apparent in the shorter 100 shot runs used for the other experiments was the tendency of the run time to increase with the number of accumulated shots. This is illustrated by the plot of run time vs. shot number shown in Figure 88. A linear fit to this data gives a rate of increase of approximately 10 ps/shot. It is also interesting to note that the short run time shots that

are visible in the oscilloscope overlay are distributed relatively evenly across all of the shots.

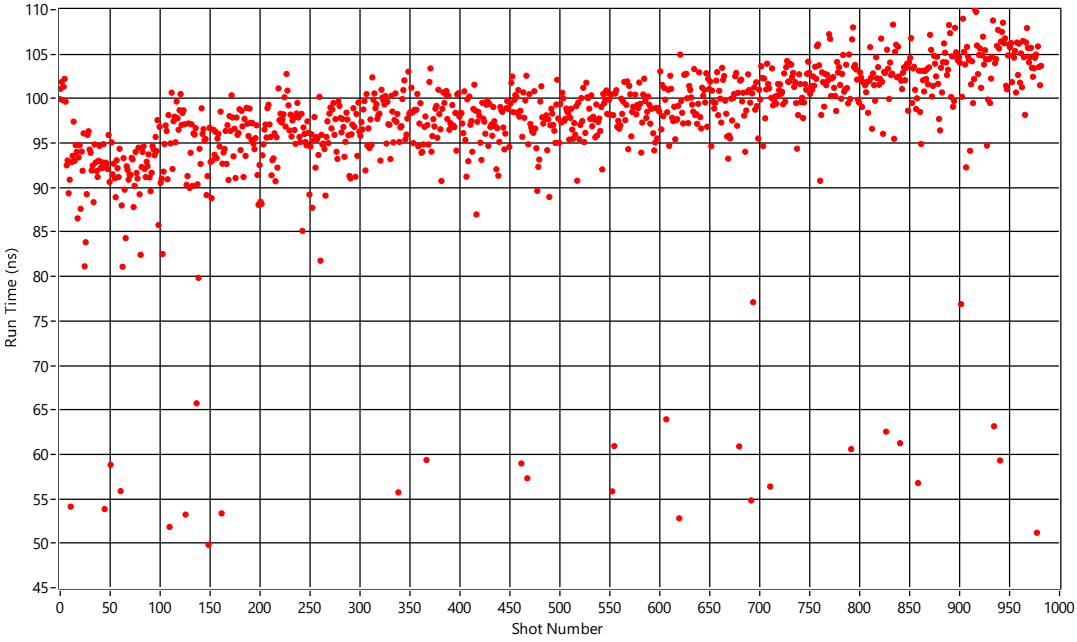

Figure 88 - Plot of run time vs. shot number for the 1000 shot run with the graphite target insert. The slope of the trend of increasing run time with accumulated shots is approximately 10 ps/shot.

Figure 89 provides before and after photographs of the second laser target insert. The damage caused by the discharges is clearly visible as a dark patch with an irregular border approximately 1.5 mm in diameter surrounded by a light-colored region approximately 3.5 mm in diameter. There is no laser hole visible in the center of the discharge area.

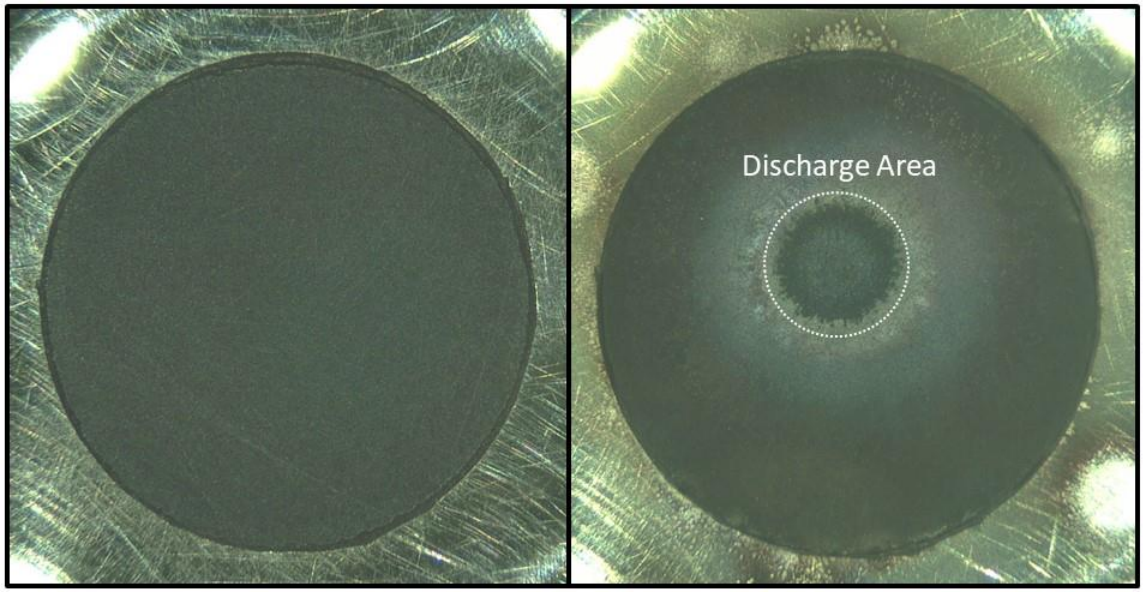

Figure 89 - Micro-photographic comparison of graphite target number two before and after 1000 shots of the high-current test setup at 10 Hz. The laser hole is not readily apparent in the discharge area.

4.7.5.3 Run to Failure

The third graphite laser target insert was installed in the switch after removal of the second insert. The switch was then operated at a repetition rate of 10 Hz for 1000 shot runs with the intention of operating the switch until the laser was no longer able to consistently trigger the switch or some other failure occurred. Pre-fires were not considered a failure unless they continued for 10 or more consecutive shots. Initially, the switch was operated at 45 psig, but this was increased to 47 psig in the middle of the second run (i.e. after approximately 1500 shots total) due to a greater than desired number of pre-fires. The pressure was increased again between the third and fourth runs to 50 psig for the same reason. This pressure was maintained until the end of the experiment. Approximately 5 minutes elapsed between each 1000 shot run due to the time required to save the oscilloscope data and take notes. The switch gas was not changed between runs.

The switch completed 11 runs and then quit firing near the mid-point of the 12^{th} run. The transition from firing to charging but not firing was relatively sudden. There were only a few missed shots before it stopped completely. The total number of shots

captured was 10774. The total number of good shots was 8093. The difference is attributed to pre-fires. Figure 90 shows screen captures of from the oscilloscope of the first run (919 shots) and the last run (431 shots).

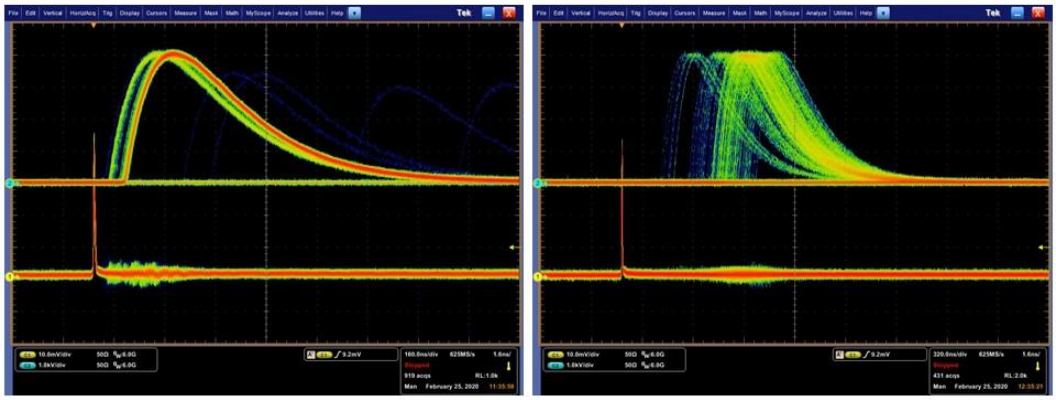

Figure 90 - Oscilloscope screen captures of the first and last runs from the graphite target insert run to failure experiment. Note that the time scale has changed by a factor of two between the two captures.

The run time and jitter increased significantly over the course of the experiment. This is clearly illustrated by a plot of run time vs. shot number as shown in Figure 91. A linear regression fitted to this data yields an average rate of increase of 80 ps/shot. For each of the 1000 shot runs, there is an obvious trend where the run time is initially higher than that of the preceding run and it slowly decreases over the course of the run. This trend becomes more pronounced for later runs and is almost completely absent in the first few runs. The source of this trend is unknown. One theory is that the heating of the target insert during the run results in an increase in plasma and/or electron emission and that this effect is more important as the electrode wears and the average run time increases. Also noticeable in this data are the step increases in run time at 1500 and 2500 shots corresponding to the two increases in switch gas pressure.

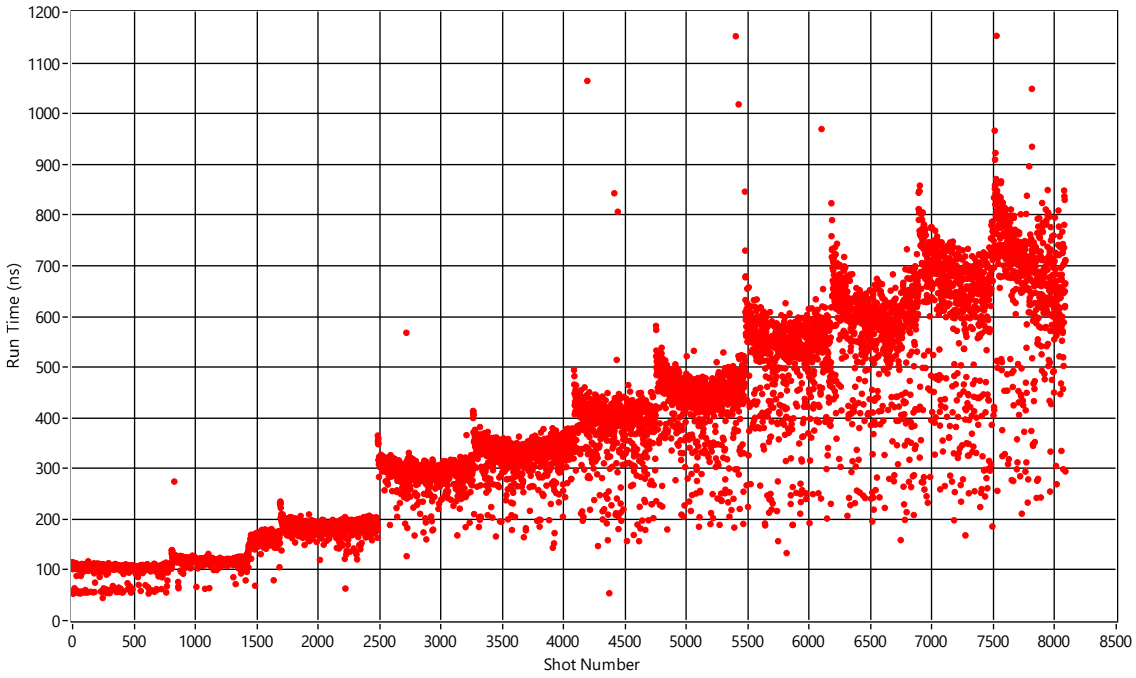

Figure 91 - Plot of the run time vs. shot number for the run to failure experiment with the graphite laser target insert. The general trend shows a linear increase in run time at a rate of approximately 80 ps/shot.

After the test was discontinued, the switch was disassembled and the components were inspected and photographed. The damage done to the target insert is shown in comparison to the pre-test insert in Figure 92. The discharges left a very obvious crater at the site of the laser focus. The laser-drilled hole is visible in the bottom of this crater. The diameter of the crater is approximately 1.5 mm and the laser hole is approximately 40 µm. The depth of the crater is difficult to estimate, but it appears to be in the range of 25% of the diameter or around 0.3 to 0.4 mm. A photograph of the entire switch is shown in Figure 93. The discoloration of the housing is a very fine soot-like material that was easily removed. This material was also found coating the majority of the laser target electrode as shown in Figure 94. However, the area immediately around the discharge crater remained clean – presumably due to the scouring effect of the discharge shock wave.

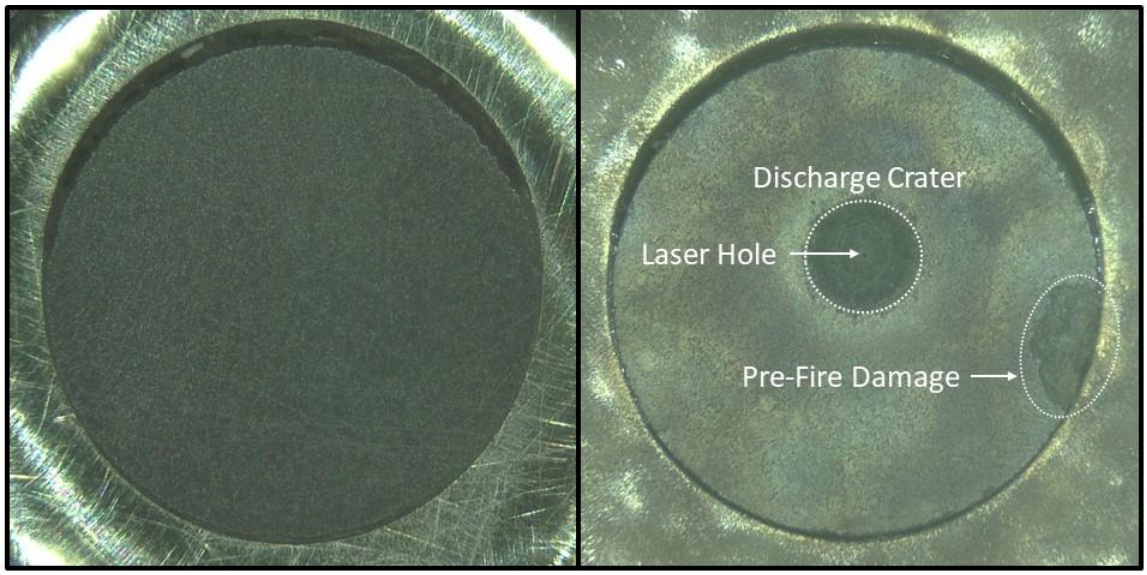

Figure 92 - Micro-photographic comparison of graphite target number three before and after the 10 Hz run to failure experiment. Note the small laser hole visible in the center of the discharge crater. The irregular-shaped dark area on the side of the target insert is where a piece of the graphite has broken off, likely due to a pre-fire discharge.

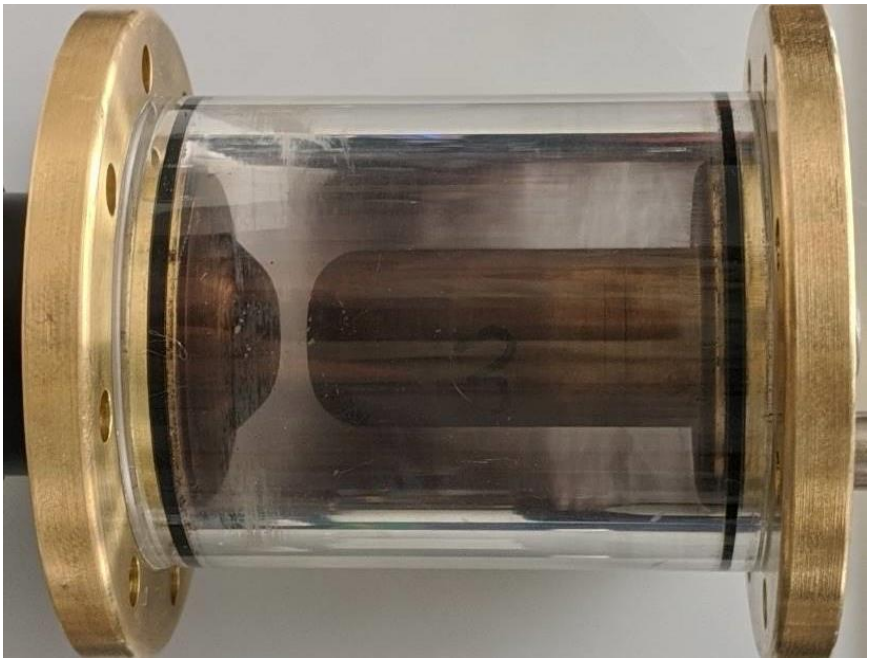

Figure 93 - Photograph of the complete switch assembly after the graphite target insert run to failure test.

Figure 94 - Target electrode assembly after graphite insert run to failure experiment before and after cleaning. Note that the area immediately around the discharge crater remains relatively clean.

The laser entrance window was also removed and inspected. It was found to have a thin coating of the same soot-like material in the area exposed to the inside of the switch. This can be seen in the photograph of the dirty window shown in Figure 95.

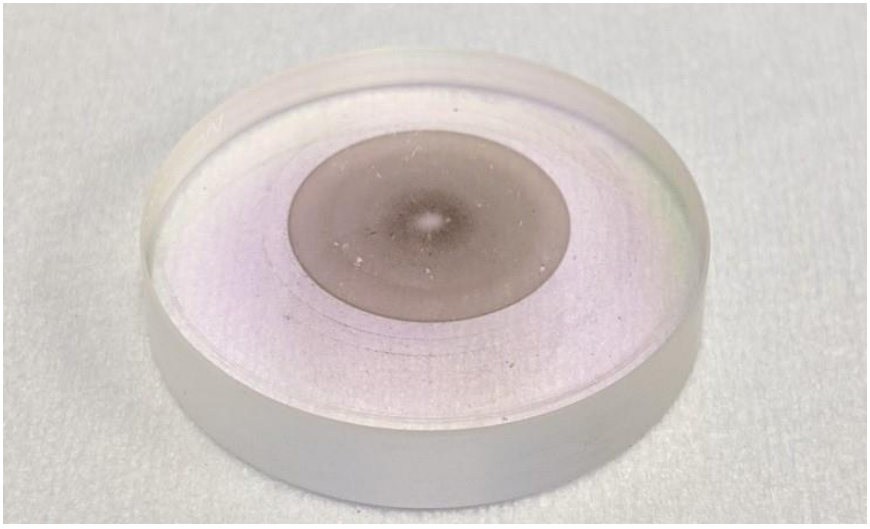

Figure 95 - Laser entrance window after graphite insert run to failure experiment. The dark discoloration in the middle of the window is the fine soot-like material. The purple color of the glass is due to the IR AR coating.

The material was deposited on the window over a circular area approximately 13 mm in diameter, but the deposition was not uniform. A central clear spot was present that was approximately the diameter of the laser entrance hole in the electrode. The clearing of this area could be due to a high-pressure jet of gas driven through the hole by the discharge. The remaining variation in the deposited material density does not have a readily apparent explanation. It is important to note that, due to the short focal length of the lens used, the beam is still relatively large diameter (approximately 3 mm) where it passes through this face of the window. This can be seen in Figure 53. In order to determine how much effect the material deposited on the window had on the energy focused on the target, measurements were made using the laser energy meter. The results showed that the dirty window absorbed approximately 20% of the energy. After cleaning the window, the absorption was unchanged from an unused window.

4.7.6 Tungsten-Copper Laser Target Insert Damage

The following sections describe the observations made during and after testing the three W-Cu laser target inserts.

4.7.6.1 Damage Due to Laser Alone

The first W-Cu laser target insert was tested using only the laser, with a switch charge voltage of zero. The switch was filled with atmospheric pressure air. Photographs taken before and after the shot through an optical microscope are shown in Figure 96. The laser damage appears as a small, well-defined hole surrounded by a ring that is somewhat darker than the material outside the affected area. The diameter of the hole is estimated to be 40 µm, while the dark ring has an inner and outer diameter of 630 µm and 900 µm respectively. These were estimated by scaling from the known diameter of the target insert.

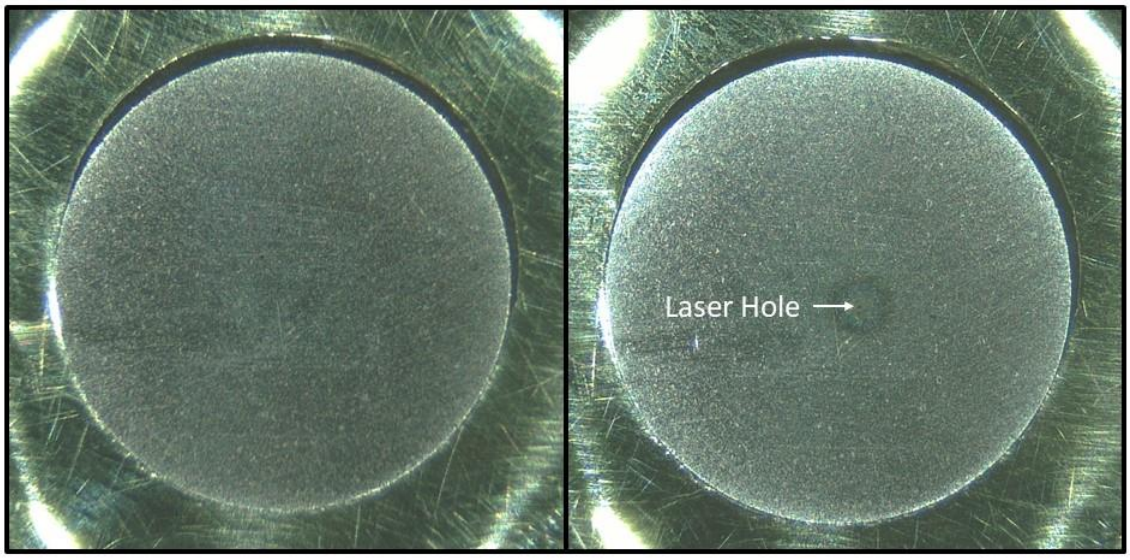

Figure 96 - Micro-photographic comparison of W-Cu target number one before and after 1000 shots of the laser at 10 Hz. The laser hole is the very small black dot in the center of the dark circular ring located near the center of the right-hand photo.

4.7.6.2 Combined Damage Due to Laser and High Current Discharge

The second W-Cu laser target insert was installed in the switch after the laser-only test was conducted on the first insert. The laser focus was not adjusted – the precise matching of the lengths of the first and second electrodes was sufficient to ensure that the laser focus remained the same. The switch was operated at 45 psig (approximately 57 psia or 393 kPa). This pressure was chosen based on scaling from the previous self-break data such that 30 kV would be approximately 80% of the self-break voltage. The 1000 shot run was conducted without any prior conditioning of the electrode. The run resulted in 1000 data captures, of which 991 were good shots where the switch closed within the data acquisition window of 1 μs. The 9 shots where the switch did not close are thought to be the result of pre-fires where the switch broke down before arrival of the laser pulse – thus leaving the capacitor discharged at the time of the laser pulse. These pre-fires are clearly audible during operation of the switch. It is believed that they are due to particles of electrode material remaining in the gap between shots. This could be reduced by flowing gas through the switch during operation, but that was not

tested during these experiments. The average switch run time was 117 ns with a 1-σ jitter of 8 ns.

The run time of the switch increased steadily during the run, similar to the 1000 shot run with the second graphite target insert. This is illustrated by the plot of run time vs. shot number shown in Figure 97. A linear fit to this data gives a rate of increase of approximately 6 ps/shot – slightly slower than the graphite target test.

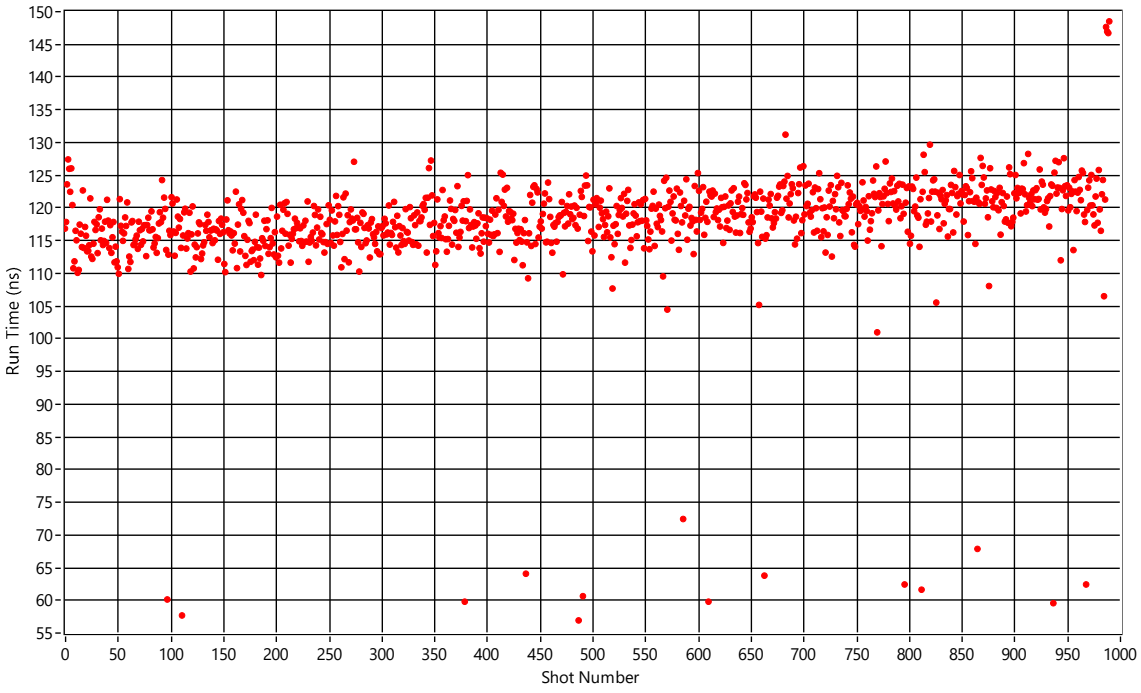

Figure 97 - Plot of run time vs. shot number for the 1000 shot run with the second W-Cu target insert. The slope of the trend of increasing run time with accumulated shots is approximately 6 ps/shot.

Before and after microscope photos of the second W-Cu laser target insert are shown in Figure 98. The electrode was cleaned with isopropyl alcohol before taking the photo after the 1000 shot run to remove the fine black dust that coated the entire electrode except for the discharge area. The laser hole is visible in the center of a large ring of light-colored material that appears to have a coarse texture. The laser hole is estimated at 40 µm in diameter. The light-colored region is approximately 670 µm inside diameter and 1.3 mm outside diameter. The discoloration of the entire remainder of the surface of the insert is presumably due to heating, since similar coloration can be

achieved on the W-Cu material by heating it with a torch. One pre-fire discharge spot is visible on the insert above the laser-triggered discharge area. This spot looks significantly different, but this cannot be attributed to the differing discharge mechanisms because the pre-fire spot is due to no more than a few discharges, while the laser-triggered discharge area experienced 991 discharges.

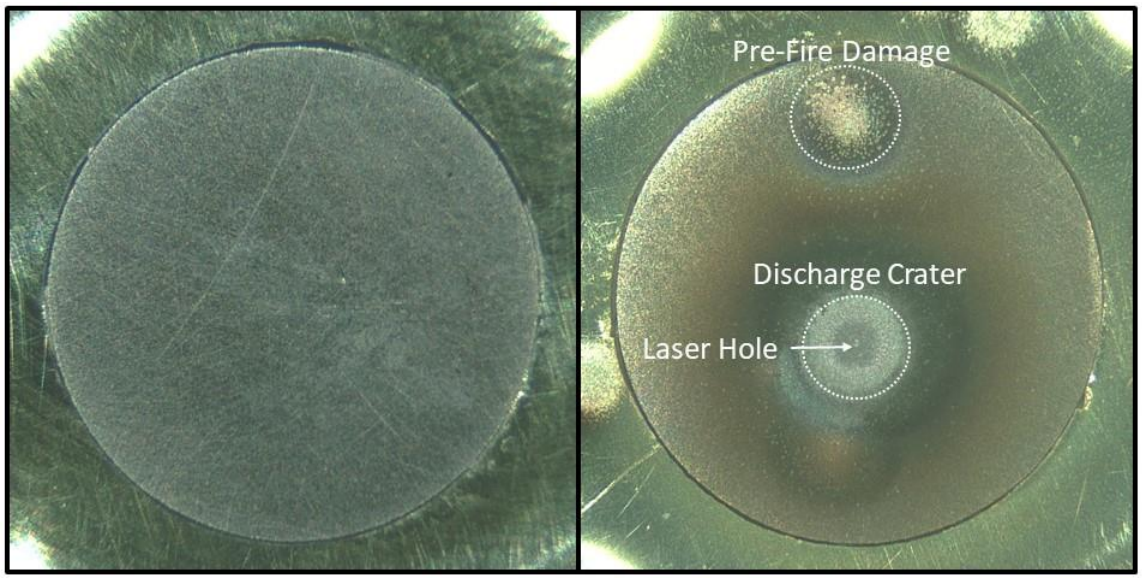

Figure 98 - Micro-photographic comparison of W-Cu target number two before and after 1000 shots of the high-current test setup at 10 Hz. The main discharge crater with laser hole is located just below center. The spot near the top of the image is due to pre-fire discharges.

4.7.6.3 Run to Failure

The third W-Cu laser target insert was installed in the switch after removal of the second insert. The switch was then operated at a repetition rate of 10 Hz for 1000 shot runs with the intention of operating the switch until the laser was no longer able to consistently trigger the switch or some other failure occurred. Pre-fires were not considered a failure unless they continued for 10 or more consecutive shots. The switch was operated at 45 psig. The first 10,000 shots were conducted in 1000 shot runs and data was recorded for all of the shots. However, the data for shots 1001 through 2000 and 5001 through 7000 was lost due to user error. This data is plotted in Figure 99. This plot shows the same general trend as was seen in the graphite target insert tests, but

the rate of increase is significantly slower at 9 ps/shot compared to the 80 ps/shot trend for the graphite. Each run also shows the tendency for the run times to start high and decrease for the first few hundred shots, with the magnitude and time scale of this effect becoming more prominent at higher shot totals. The source of this effect is unknown, but given the number of shots involved, it could be due to electrode heating increasing the amount of material and/or electrons ejected from the surface by the laser. The fact that the effect is more pronounced as shots accumulate could be due to the reduction in laser irradiance as the electrode surface recedes from the original focal plane.

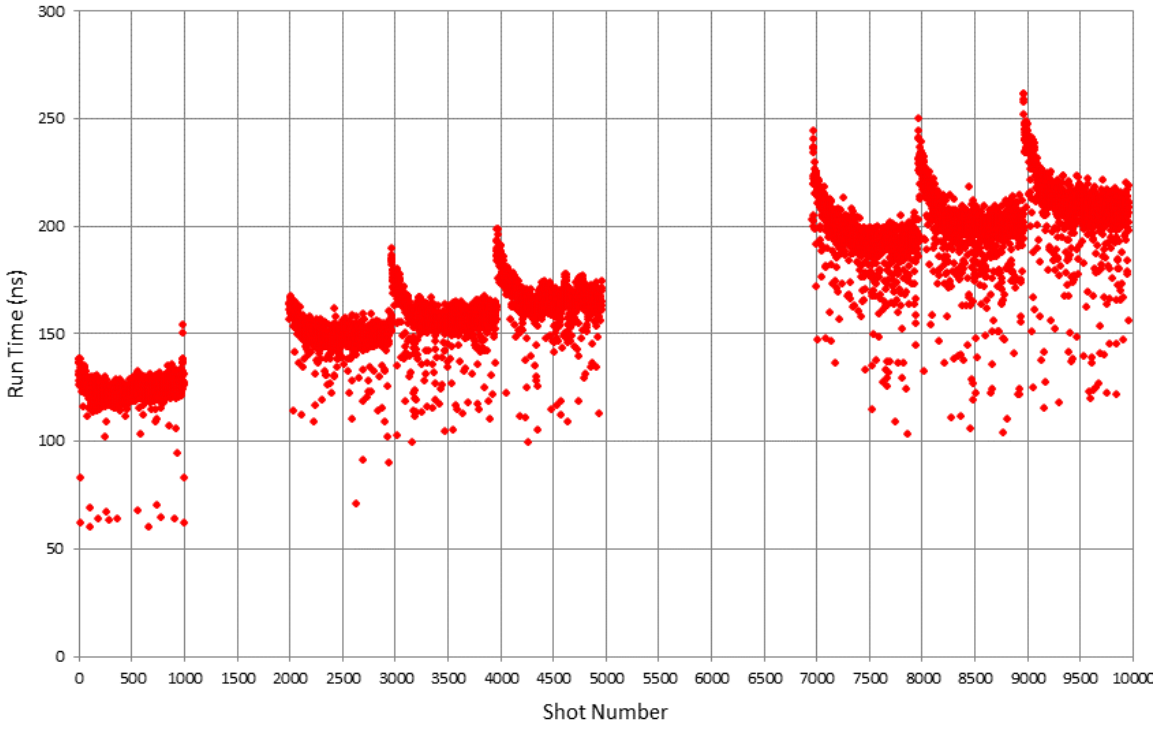

Figure 99 - Plot of the run time vs. shot number for the first 10,000 shots of the run to failure experiment with the W-Cu laser target insert. The data for shots 1001-2000 and 5001-7000 was lost due to user error. The general trend shows a linear increase in run time at a rate of approximately 9 ps/shot.

After the first 10,000 shots, the switch with the W-Cu insert was still working well, so the number of shots per run was increased. Due to the limitations of the data collection system, data could not be captured for every shot. However, at least 1000 shots were

recorded for each run. Table 8 provides a listing of the shots conducted in this experiment. The test was terminated after 129,500 shots due to failure of the laser to continue triggering the switch. Total charge transferred was approximately 233 C. The results show a general trend of increasing run time and jitter as shots are accumulated. Figure 100 plots the average run time and jitter for the shots that were recorded during each of the runs. The large increases in run time for the first runs after the switch sits overnight and when the switch was cleaned after 100,000 shots could be attributed to changes of the surface chemistry of the target insert (e.g. formation of oxides) caused by the target's exposure to the atmosphere. It is also interesting to note that the rate of increase in run time per shot seems to have slowed significantly after the first 20,000 shots. The slope during the shots after 20,000 is approximately 1 ps/shot.

Table 8
W-Cu Target Insert Run to Failure Shot Record

Run Number	Start Shot	End Shot	Recorded Shots	Good Shots	Average Run Time (ns)	Jitter (ns)	Notes
1	1	1000	1000	987	123	8	
2	1001	2000	-	-	-	-	Data lost
3	2001	3000	1000	998	149	8	
4	3001	4000	1000	999	157	11	
5	4001	5000	1000	997	166	11	
6	5001	6000	-	-	-	-	Data lost
7	6001	7000	-	-	-	-	Data lost
8	7001	8000	1000	1000	193	15	
9	8001	9000	1000	1000	199	18	
10	9001	10000	1000	999	209	19	
11	10001	13000	-	-	-	-	Data lost
12	13001	23000	-	-	-	-	Data lost
13	23001	24000	1000	1000	273	40	
14	24001	25000	1000	998	346	73	New day of testing
15	25001	35000	3000	2985	246	51	
16	35001	45000	2067	2064	272	48	
17	45001	55000	3000	2985	226	40	
18	55001	65000	3000	2970	227	40	
19	65001	75000	3000	2989	300	61	
20	75001	85000	3000	2986	356	109	New day of testing
21	85001	95000	3000	2997	305	63	

Run Number	Start Shot	End Shot	Recorded Shots	Good Shots	Average Run Time (ns)	Jitter (ns)	Notes
22	95001	100000	2000	1995	368	80	
23	100001	101000	1000	975	528	75	Cleaned and inspected switch before this run
24	101001	102000	1000	996	519	61	
25	102001	122000	1000	986	295	58	
26	122001	129500	1000	806	384	93	Stopped due to triggering failure

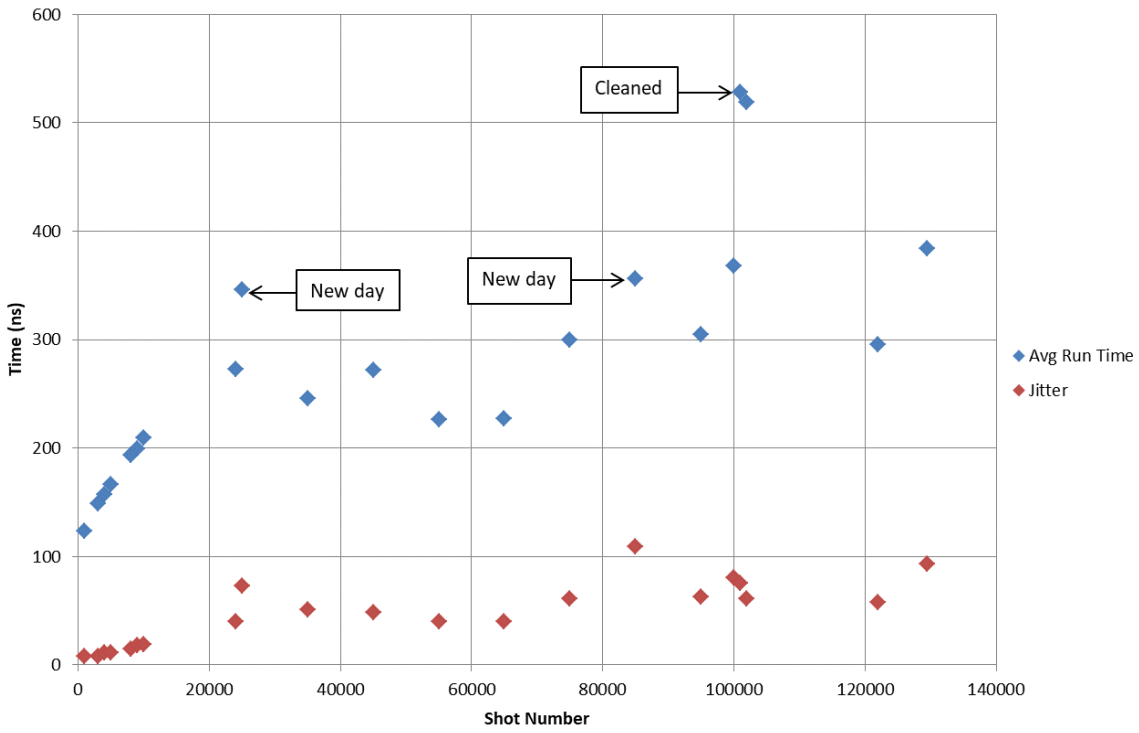

Figure 100 - Plot of average run time and jitter for the shots recorded during the W-Cu target insert run to failure experiment. The data points are placed at the position of the last shot of the run in which they were recorded.

When the test reached 100,000 shots, the switch was disassembled and the components were inspected and cleaned. The switch was then reassembled and testing resumed. Based on the minimal degradation in switch performance, it was thought that it may continue to run for another 100,000 shots. However, failure occurred after only 29,500 more shots. After failure the switch was disassembled again for inspection. The damage done to the target insert is shown in comparison to the pre-test insert in Figure

101. Like the graphite target case, the discharges eroded a crater at the site of the laser focus with the laser hole still visible in the center. The diameter of the crater is estimated as 1.1 mm and the laser hole is approximately 30 µm. The edge of the crater is surrounded by a raised ridge of light silver colored material. The crater appears to be deeper and more conical than the one in the graphite target insert.

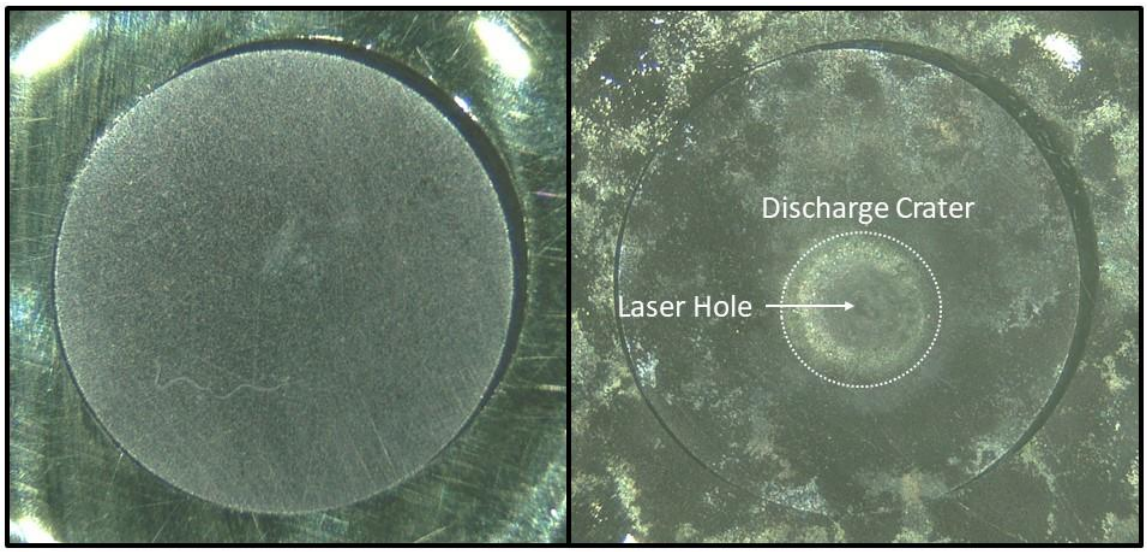

Figure 101 - Micro-photographic comparison of W-Cu target number two before and after the 10 Hz run to failure experiment (129,500 shots). Pre-fires have resulted in extensive discoloration of the brass electrode around the target insert.

A photograph of the entire switch as it appeared after 100,000 shots is shown in Figure 102. Similar to the graphite insert test, a light coating of fine dust was deposited on the inside of the housing, but this material was easily cleaned off. However, the acrylic housing remained discolored on the inner surface in a ring centered on the gap. This area was exposed to the ultraviolet emissions of the arc, which are known to cause discoloration of acrylic with sufficient exposure. The dusty material also completely coated the target and laser entrance electrodes except for the discharge crater, which retained its bright metallic appearance. The area around the hole in the laser entrance electrode was significantly eroded and was likely the source of much of the material deposited throughout the switch housing. This electrode was fabricated from 360 alloy brass, which contains copper, zinc, and lead as its three main constituents. The erosion

and re-deposition of material could be significantly reduced by using a more robust refractory metal such as W-Cu for this electrode.

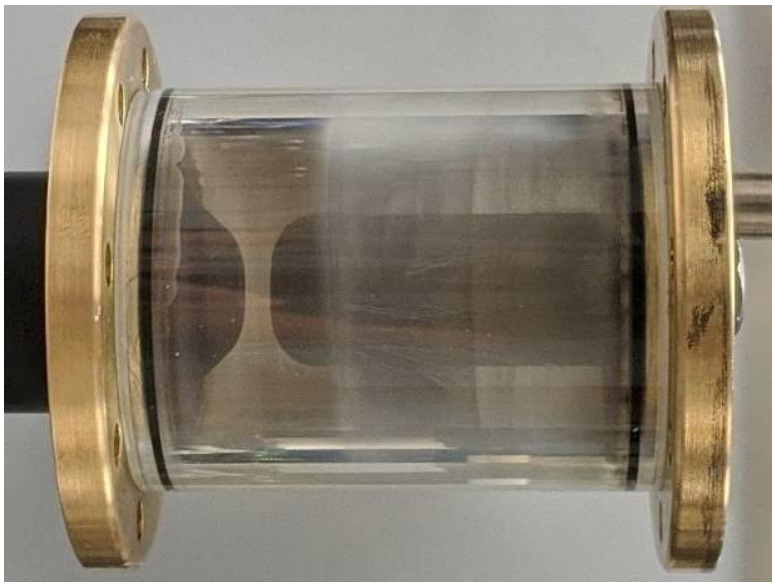

Figure 102 - Photograph of the complete switch assembly after the first 100,000 shots of the W-Cu target insert run to failure test.

The laser entrance window was removed and examined as well. The same fine dusty material was found to be deposited on the window as shown in Figure 103.

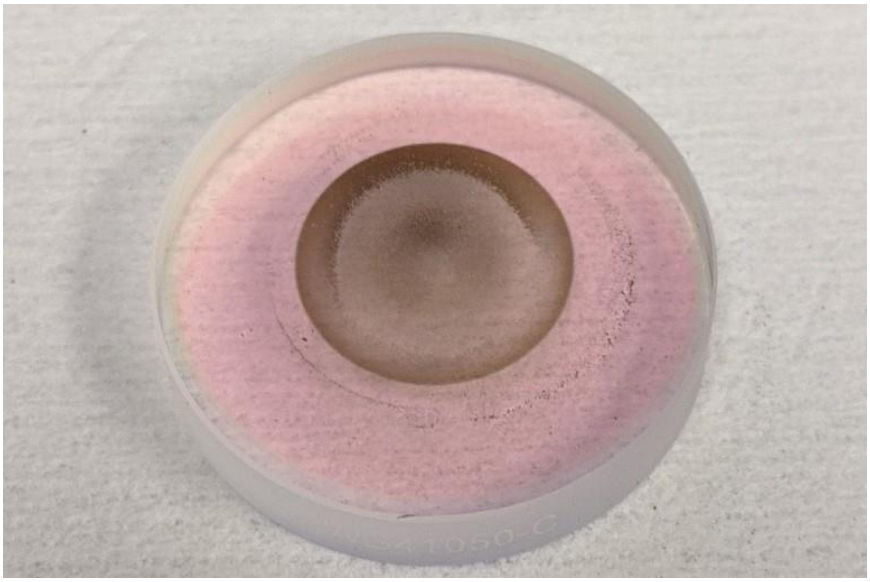

Figure 103 - Laser entrance window after W-Cu target insert run to failure experiment (129,500 shots).

The material was deposited on the window over a circular area approximately 13 mm in diameter, but the deposition was not uniform. Similar to the window used in the graphite insert experiment, the deposits took the form of concentric rings, with the inner-most spot relatively clear. The outer-most ring of material on the window is very dark and has an irregular edge. Under magnification, this edge looks like material was sprayed outward, as can be seen in Figure 104. This is consistent with the material being driven against the window by the high-pressure shock wave of the discharge. In order to determine how much this material deposited on the window affected the energy focused on the target, measurements were made using the laser energy meter. The results showed that the dirty window absorbed approximately 19% of the energy compared to no window. After cleaning the window, the absorption was approximately 3%. This represents a permanent degradation of the window. The area where the deposits had been showed a very slight visible change after cleaning.

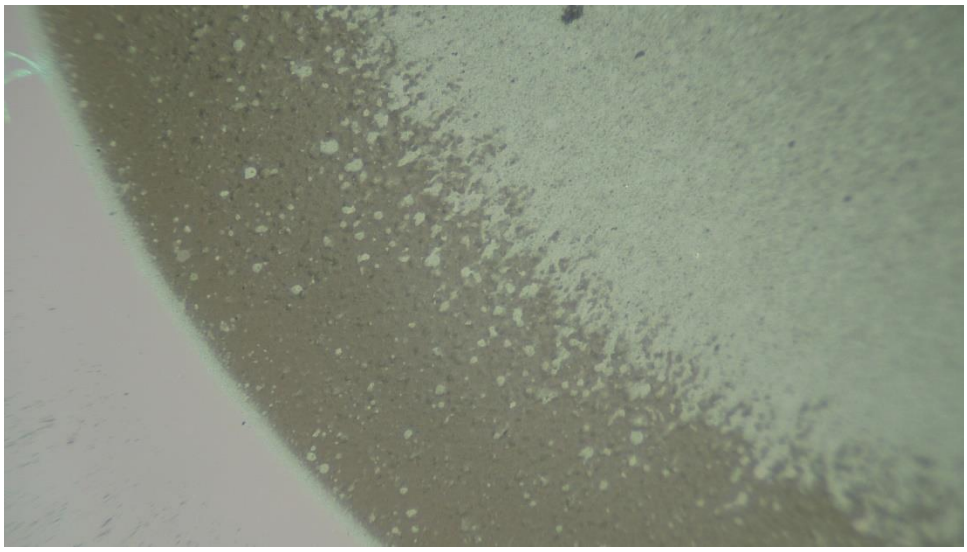

Figure 104 - High magnification image of the outer ring of deposited material on the laser entrance window. The material appears to have been sprayed outward from the center and built up where the window met the edge of the aperture in the switch electrode.

4.7.7 Discussion of Laser Target Damage Experiments

The experiments described in this section have provided some insight into the effects of a large number of shots at relevant repetition rates and discharge characteristics. The

principal observation to be made is that the discharge does significantly more damage to the electrode than the laser. However, the fact that the laser-triggered discharge always occurs in the same location on the electrode tends to concentrate this damage. Some means of moving the laser focus around on the surface of the electrode – either automatically or through routine maintenance activities – could significantly extend the lifetime of the switch. Based on the current results, W-Cu is a superior material for use as a laser target material for this type of laser triggered switch in repetitive, high current discharge applications. However, further experimentation with better grades of graphite – in particular those developed for use in electrical discharge machining – should be made before discounting graphite as a laser target material.

4.8 Absorption of 1535 nm Laser Pulses in Insulating Oils

Because laser triggering using the 1535 nm wavelength has not been explored by pulsed power researchers, there are many open questions with respect to the integration of this type of laser into pulsed power systems. One of the major engineering challenges to the incorporation of laser triggering in a pulsed power system is the design of the beam transport system. Since one of the benefits of laser triggering is galvanic isolation between the switch and the laser electronics, the beam must often be routed over a complex path to the switch. Often the beam must cross the high voltage insulation of the system. If this insulation is a liquid, the beam must either be provided with a gas filled path, or it must pass through the liquid. The first option – gas filled beam pipes – introduces a weakness in the insulation. Direct transport through the insulating liquid is much more convenient but necessitates that the liquid have minimal absorption of the laser energy. This technique has been employed using visible wavelength laser light in a water-insulated system [86]. However, the absorption of near infrared wavelengths is not closely related to the visible transparency of a fluid as is evidenced by the extremely high absorption of 1535 nm light in water [87]

Insulating oil – also commonly called transformer oil – is a common high voltage dielectric in compact pulsed power systems. Insulating oil can be divided into two

principal types: hydrocarbon oils and silicone oils. Hydrocarbon oils are manufactured from highly refined petroleum base stock or synthesized from natural gas [88]. Silicone oils are synthetic polymers formed from the dimethylsiloxane base molecule [89]. All types of insulating oil are transparent in appearance when new, although petroleum-based oils sometimes have a slight yellow tint. Hydrocarbon oils will visibly darken with age and exposure to elevated temperatures due to oxidation [90]. Silicone oil does not visibly change with age if it remains uncontaminated. While transmission spectra of some insulating oils have been measured for the mid-infrared range of wavelengths [91], data is not available at 1535 nm. Thus, a simple experiment has been conducted to quantify the absorption of this wavelength for some commonly available insulating oils.

4.8.1 Experimental System

The complete experimental setup used to obtain triggering data is shown in Figure 105 and the major components are described in the following sections – except the laser, which was described in section 4.2.1.

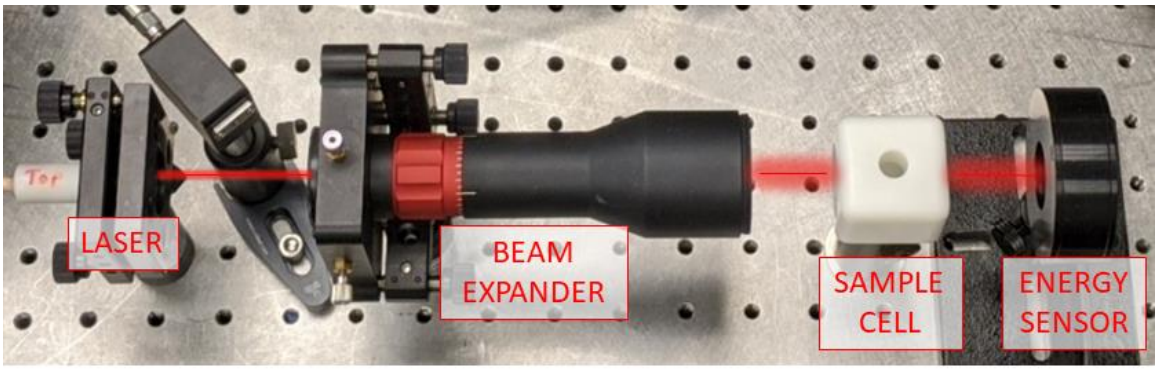

Figure 105 - Labeled photograph of the absorption experiment optical system with an overlaid illustration of the laser beam path.

4.8.1.1 Sample Cells

Three sample cells were fabricated by stereolithography additive manufacturing. These cells are fitted with O-ring sealed laser windows and feature a 12.7 mm bore that can be filled with the oil under test. Both windows (Thor Labs P/N WG41050-C) have a broad-band infrared AR coating on both surfaces. The total loss due to reflection at the optical interfaces is estimated at less than 5% for the complete optical system based on

manufacturer's data. The sample cells are filled and drained through a hole on the top surface. The laser path length through the sample volume is different between the three cells to permit calculation of the absorption coefficient as described in section 4.8.3. A photograph of the 2 cm sample cell is shown in Figure 106.

Figure 106 - Photograph of 2 cm sample cell filled with insulating oil. Visible reflection of the room lights on the window is due to infrared AR coating.

4.8.1.2 Optics and Diagnostics

Before the beam passes through the sample cell, it is expanded by a factor of 10 using a telescope with AR coated optics (Thor Labs P/N GBE10-C). This is done to limit the power density on the surface of the pyroelectric sensor. The sample cell under test is placed between the beam expander and the sensor as shown in Figure 105. The sensor is an Ophir Photonics model PE25-C sensor that is capable of measuring laser pulse energy from 8 µJ to 10 J. The sensor has a noise level of 0.5 µJ and a calibration accuracy of ± 3% when operating in the energy range used for these experiments. Data was collected as delimited text files using the StarLab software application.

4.8.1.3 Dielectric Oil Samples

A selection of dielectric oils from three major manufacturers – Royal Dutch Shell, Petro Canada, and Dow Chemical – were chosen for this experiment. Oil types were selected

to represent the variety of oils used in pulsed power applications. The oils tested are listed in Table 9. A photograph of the oil samples is provided in Figure 107.

Table 9
Dielectric Oils

Oil Type	Manufacturer	Base
Diala™ S2 ZX-A	Shell	Naphthenic Hydrocarbon
LUMINOL™ TR-i	Petro Canada	Paraffinic Hydrocarbon
LUMINOL™ LS	Petro Canada	Paraffinic Hydrocarbon
XIAMETER™ 561	Dow Chemical	Polydimethylsiloxane

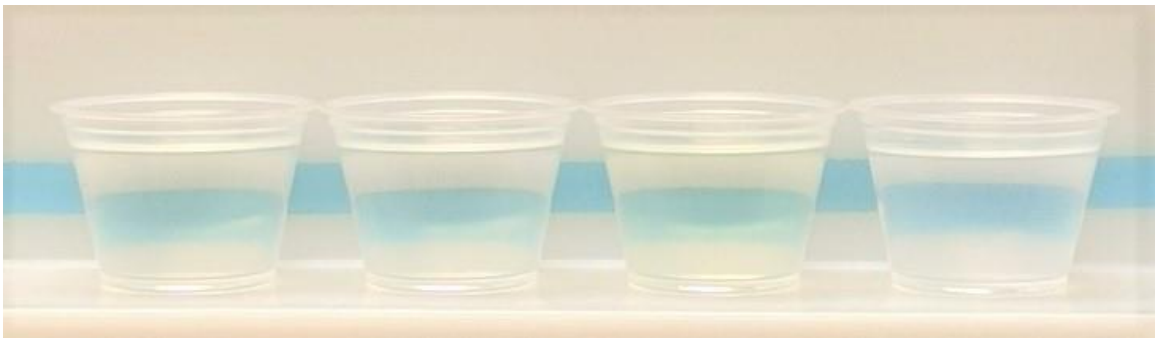

Figure 107 - Photograph of samples of the four oils tested in this experiment. From left to right: LUMINOL LS, LUMINOL TR-i, Diala S2 ZX-A, and XIAMETER 561. The three hydrocarbon oils have a very similar appearance except that the Diala has a slightly yellow tint. The XIAMETER is perfectly clear with a lower refractive index as indicated by the different refraction of the blue line.

4.8.1.3.1 Shell Diala

Diala is the brand name of Royal Dutch Shell's line of insulating oils developed for use in transformers and other power industry systems. While there are many types of Diala, only the S2 ZX-A type (previously called Diala AX) is available in the United States. It is a refined petroleum oil with a primarily naphthenic base and added oxidation inhibitors [92]. Diala is the most commonly used insulating oil in pulsed-power applications in the United States due to the ready availability, relatively low cost, and familiarity. New Diala S2 ZX-A has a visual appearance that is nearly clear with a very slight yellow tint. With age and exposure to the atmosphere it becomes more yellow and eventually an orange-

brown color. This can take months to years depending on ambient conditions. This coloration does not affect the dielectric properties.

4.8.1.3.2 Petro Canada LUMINOL

LUMINOL is the name of the line of paraffinic base transformer oils manufactured by Petro Canada. The two types of LUMINOL tested in this experiment are the TR-i formulation and the LS formulation. TR-i consists of a highly refined paraffinic base along with oxidation inhibitors and negative-gassing additives. This product is intended for use in power transformers and switchgear. LUMINOL LS is a formulation developed for special applications. The principal difference between the two is that the LS lacks the negative-gassing additive of the TR-i formulation. This additive is responsible for the majority of the odor of TR-i, thus LS is very low (almost imperceptible) odor [93]. Both types of LUMINOL are completely clear when new. They will gain color with age and atmospheric exposure at a slower rate than naphthenic base oils.

4.8.1.3.3 Dow XIAMETER

XIAMETER 561 is a polydimethylsiloxane-based transformer oil manufactured by Dow Chemical. Silicone transformer oils have the principal advantage of having a very low flammability – thus making them advantageous for transformers located indoors and in other high-risk locations. Additionally, the silicone polymers are more stable over long periods at elevated temperatures [89]. Silicone transformer oils are not as widely used as hydrocarbon oils in the power industry due to significantly higher cost and concern about their lack of biodegradability.

4.8.2 Methodology

4.8.2.1 Procedure

Each oil type was tested using the following procedure. First, the test cells and windows were cleaned with isopropyl alcohol and methanol to remove any traces of previous oil samples. The 1 cm test cell was then placed in the laser beam path with no oil fill. The

laser was energized and set to a repetition rate of 0.5 Hz and allowed to run until the energy stabilized. This repetition rate was chosen due to the improved pulse-to-pulse energy stability exhibited by the laser at this slower rate. A run of 100 shots was recorded and the average energy calculated. The measured standard deviation of the laser after it stabilized was always approximately equal to the sensor noise floor of 0.5 μJ. After the laser stabilized, it was allowed to continue running at 0.5 Hz for the remainder of the experimental series to maintain the stability.

Without removing the test cell from the beam path, it was filled with the oil under test. A run of 100 shots was recorded and the average energy calculated. The 1 cm cell was then removed from the beam path and emptied. The windows were removed and transferred to the 2 cm cell using a suction optic holder to prevent contamination of the outer surfaces. The 2 cm cell was then placed in the beam path and filled with oil. After ensuring that the newly measured energy was stable for several shots, a run of 100 shots was recorded. This process was repeated with the 4 cm cell.

4.8.2.2 Data Collection and Analysis

Data for each set of shots was collected using the StarLab software provided with the Ophir laser energy sensor. The data is saved in a delimited text file which includes information on the statistics of the shots. The average energy figure provided in this file was used as the basis for calculating the absorption coefficient as described in the following section.

4.8.3 Calculation of Absorption Coefficient

Lambert's law for the transmission of light in a uniformly absorbing material can be expressed in the form:

$$W = W_0 \cdot exp(-\alpha d) \tag{24}$$

where W is the transmitted energy, W_0 is the incident energy, α is the Lambert absorption coefficient, and d is the optical path length through the absorbing material. In this experiment, W and d are the known quantities. To accurately calculate α, the

incident energy, W_0, must be adjusted to account for all losses in the optical path not due to the absorbing material. Since the test cell includes windows whose reflectance depends on the refractive index of the material in contact with the window, it is impossible to determine W_0 based on the measured transmission without the oil in the cell. Instead, the measurements are taken with two different values of *d* and the ratio of the transmitted energy can be used to calculate α as shown below. First, re-arranging Lambert's law for the two measurements results in:

$$W_0 = \frac{W_1}{exp(-\alpha d_1)} \tag{25a}$$

$$W_0 = \frac{W_2}{exp(-\alpha d_2)} \tag{25b}$$

Since the non-absorption losses are the same for the two path lengths, W_0 is the same for both measurements and the right-hand sides can be set equal to each other:

$$\frac{W_1}{exp(-\alpha d_1)} = \frac{W_2}{exp(-\alpha d_2)} \tag{26}$$

Re-arranging and taking the natural logarithm of both sides results in:

$$\ln\left(\frac{W_1}{W_2}\right) = \alpha(d_2 - d_1) \tag{27}$$

Thus, one obtains an expression for α in the known quantities:

$$\alpha = \frac{\ln\left(\frac{W_1}{W_2}\right)}{(d_2 - d_1)} \tag{28}$$

4.8.4 Absorption Coefficients

Since three data points were measured for each of the oils, a choice had to be made on which points to use in calculating α using (28). The choice was made to use the data for the 1 cm and 4 cm path lengths to calculate α. The value of W_0 was calculated by inserting this α value into (25a) and (25b). The 2 cm data was then used as a check of the fit. This was done by calculating the difference between the measured value at 2 cm with the expected 2 cm value calculated from the exponential fit and expressing the

result as a percentage of the expected value. For the fit to be acceptable, the error should be within the estimated experimental uncertainty of +/- 3%.

The results of the measurements and calculations described above are summarized in Table 10. The recorded energy and standard deviation (SD) for each of the oil path lengths is shown, along with the energy and SD for the clean and empty 1 cm test cell. The SD value for the 1 cm LUMINOL LS run is much higher than the others due to a couple of consecutive shots of very low energy from the laser that occurred during that run. The cause of this is unknown. For all of the oils, except the LUMINOL LS, the error between the exponential fit and the 2 cm data was less than 1%. For the LUMINOL LS, the error was 2.9%, which is still within the 3% tolerance of the energy meter calibration. The difference between the clean cell transmitted energy and the calculated values of W_0 can be attributed to the refractive index mismatch between the window AR coating – which is designed to work in air – and the oil. This creates additional loss from reflection at the interface.

Figure 108 provides a graphical representation of the data and the exponential fits. The measured values have been normalized by dividing them by the calculated values of W_0. This plot illustrates the similarity of the two types of LUMINOL, which is to be expected given their nearly identical composition. The Diala exhibits the lowest absorption which is interesting given that it is visually the least clear oil. The XIAMETER exhibits about twice the absorption of the hydrocarbon oils.

Table 10
Absorption Measurement Results

Parameter / Oil Type	LUMINOL LS	LUMINOL TR-i	Diala S2 ZX-A	XIAMETER 561	Water*
Clean 1 cm Cell Avg Energy ± 1 SD (μJ)	218 ± 0.51	208 ± 0.43	217 ± 0.50	218 ± 0.47	N/A
1 cm Avg Energy ± 1 SD (μJ)	167 ± 1.38	160 ± 0.42	169 ± 0.42	130 ± 0.31	N/A
2 cm Avg Energy ± 1 SD (μJ)	128 ± 0.44	127 ± 0.36	136 ± 0.44	80.3 ± 0.35	N/A
4 cm Avg Energy ± 1 SD (μJ)	82.0 ± 0.33	79.4 ± 0.33	90.0 ± 0.35	31.4 ± 0.34	N/A
α (cm^{-1})	0.237	0.234	0.210	0.474	12.1
1/e Depth (cm)	4.22	4.28	4.76	2.11	0.08
W_0 (μJ)	212	202	208	209	N/A
Exp Fit Error at 2 cm	2.9%	0.3%	0.7%	0.8%	N/A

* Water data from [87] for comparison

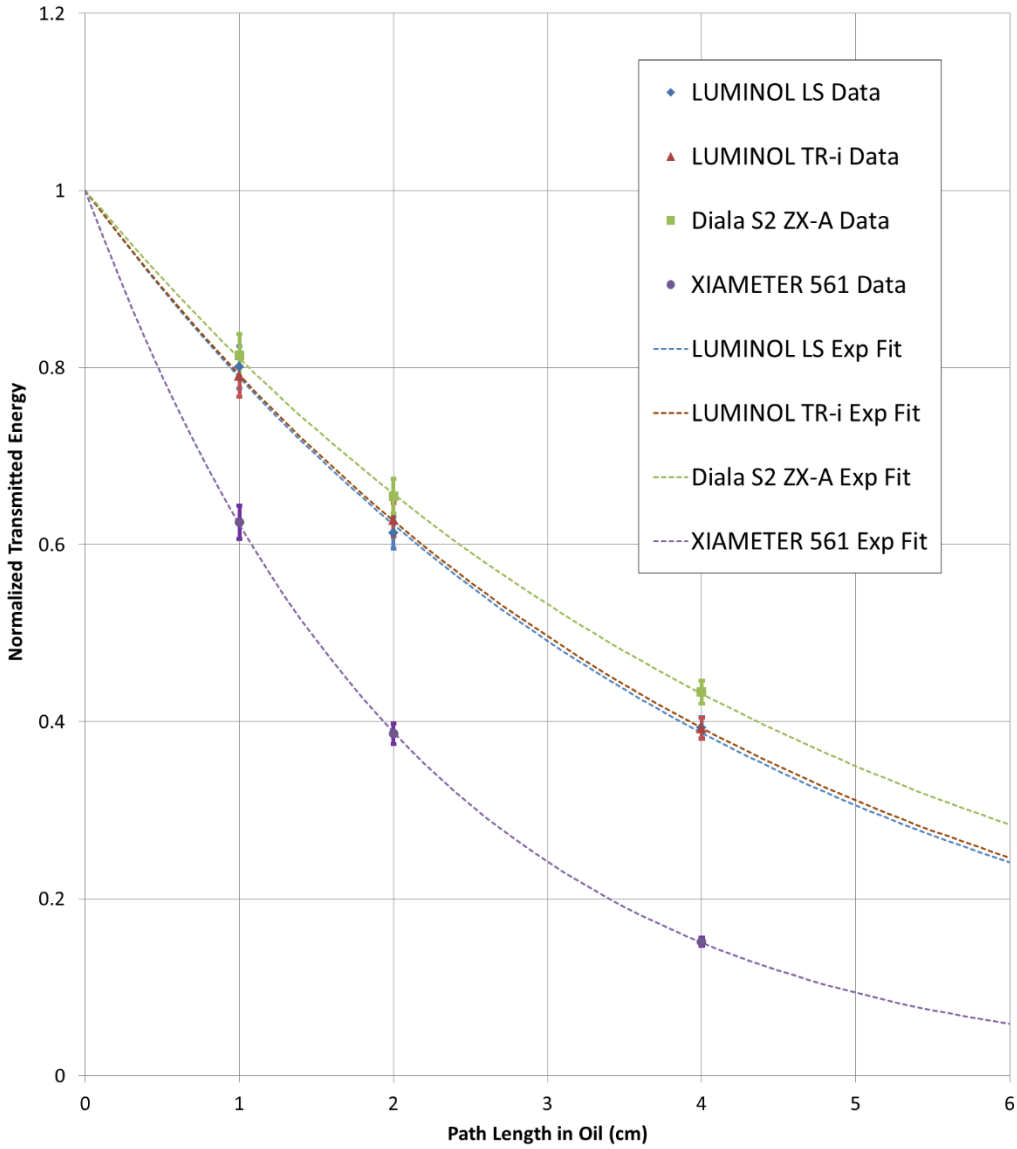

Figure 108 - Plots of the normalized transmitted energy data points measured for each of the four insulating oils and exponential fit lines calculated from the values of α listed in Table 10. The error bars represent the 3% uncertainty in the energy meter calibration.

The insulating oils sampled in this experiment showed absorption coefficients for 1535 nm light between 0.2 and 0.5 cm^{-1}. This gives an optical depth of less than 5 cm for a 63% reduction in energy. The three hydrocarbon oils had very similar values of absorption coefficient, while the silicone oil was approximately twice as high. Since most compact pulsed power systems have dimensions on the order of 100 cm, the short optical depth will make beam transport through the insulating oil impractical for all but

the most compact configurations. Fortunately, the very small size of this type of laser opens up new packaging possibilities for the compact pulsed power engineer – including the possibility of incorporating the laser directly into the switch. This is an area of ongoing research.

CHAPTER 5
CONCLUSIONS

5.1 Overview

This dissertation has presented contributions to three research topics to advance the development of compact pulsed power technology. Advancing compact pulsed power technology holds the key to the deployment of a wide variety of new technologies in fields as diverse as national defense and plasma agriculture. As an enabling technology, pulsed power often receives less attention than the applications that it makes possible. However, effective systems engineering necessitates knowledge of and tools for all aspects of the system – even those behind the scenes.

5.2 SPICE Modeling of Gas Switches

Chapter 2 described a parametric spark gap model developed for the ubiquitous SPICE circuit simulation algorithm. The goal of developing this model was to provide a tool for engineers to use in the simulation of circuits within a familiar software platform during the development of new compact pulsed power systems. The ability of the model to predict the behavior of a spark gap switch was demonstrated with two examples that cover a wide range of pulsed power applications. Since the initial publication of this model [94], the interest from the pulsed power community has been encouraging. The model has been shared with dozens of researchers around the world and the conference paper has been downloaded over 1,000 times.

5.3 Erection Dynamics of Compact Marx Generators

Chapter 3 described an analysis of fundamental Marx operation that was initiated when a newly built generator had difficulty erecting, even with a robust trigger source. A survey of the literature revealed that a detailed study of the Marx erection process had not been documented using modern computational techniques. Moreover, numerous anecdotes from practitioners indicate that, in general, the erection sequence was not

adequately understood to produce reliable designs prior to fabrication. The presented analysis shows the prevailing description of Marx operation is incomplete and explains the often noted, non-sequential pre-fire of the final spark gap. Further analysis of the effects of various stray capacitances on the operation of a Marx have shown that proper consideration of these stray capacitances is necessary for the development of Marx generators for reliable triggered operation. Because compact, low energy Marx generators often exhibit very large values of stray capacitance, this is even more true for this class of pulsed power devices.

This analysis was limited to the case of a resistively charged four stage, single polarity Marx generator terminated in a resistive load. The sequential erection of the stages is the primary goal. The switches are assumed to be spark gaps but the analysis remains valid for other switches such as transistors provided the magnitude of the switch capacitance C_g is considered. The analysis starts by considering the baseline case where stray capacitance is absent and we conclude that sequential erection of the Marx cannot, in fact, occur. The last gap fires directly after the first stage starts the erection process because the last gap is held to ground potential and sees twice the initial stage potential while the other stages remain charged to the stage potential.

The next case incorporates the capacitance associated with the switching elements. When the first stage is triggered, the remaining circuit is a capacitive voltage divider. The switches are overvolted by a factor related to the remaining number of open gaps and this overvoltage decays with time. The load also sees a pre-pulse. The Marx resistor network allows the final gap to gain additional charge and raises the potential to approximately twice the charge voltage while the middle stage gaps decay towards V_0. This explains the observation that the last gap often breaks down directly after the first stage is triggered. Thus, the effect of gap capacitance allows sequential operation of the Marx generator – but with very tight restrictions on the number of stages and operating voltage. An example of this Marx, with gap capacitance but no stray capacitance, is a physically long gas insulated Marx such as those found in impulse simulators.

Next, the case with stray capacitance to ground is considered. The introduction of significant stray capacitance to ground aids the erection process because it maintains a voltage between the switches that remain open during erection as well as providing a charging path that is independent of the load. The full overvoltage appears across the second switch. When both the capacitance to ground and gap capacitance are greater than zero, the circuit forms a voltage divider and the voltage on the second stage depends on the ratio of these, with larger ratios producing larger overvoltages on the second stage. This case is operative when a Marx generator is enclosed in a grounded metal housing.

The final case is where the inter-stage capacitance is considered. Here it is the ratio of the inter-stage capacitance to gap capacitance that determines the overvoltage on the second stage. Coupling between alternate stages may be accomplished either through the physical layout or by introducing coupling capacitors. This case exhibits unusual behavior: once the first stage closes, the voltage on stages 2 and 4 rises while the voltage on stage 3 drops to zero. In the realistic case with both non-adjacent inter-stage capacitance and gap capacitance, the overvoltage depends on the ratio of the two, with higher voltages achieved with larger ratios.

One effective means of engineering to achieve the desired erection behavior is to increase the ratio of stray capacitance to ground to the gap capacitance for each stage. A computational analysis of the scaling of this ratio with variations in the geometry of a notional compact Marx was described. This showed that, in general, improving this ratio requires reduction in energy density and/or increasing electric field stress in the Marx insulation. Some examples of systems that employed discrete capacitors to couple down-stream stages to ground were given. The erection performance improvements shown by this technique are significant and can be achieved with relatively small impacts on system size and complexity if incorporated into the design from the beginning.

5.4 Micro-Laser Triggered Gas Switches

Chapter 4 described the experiments that demonstrated reliable, high performance triggering of a pressurized gas switch using a COTS 1535 nm Er:glass DPSS laser with a pulse energy of less than 250 μJ. In addition to proving the viability of this laser as a trigger source, additional experiments were conducted to explore the effects of switch charging polarity, laser target material, laser pulse energy, gas composition, and laser-induced electrode damage. The absorption of this particular laser wavelength in common insulating oils was also explored to provide information relevant to compact pulsed power system engineering.

The initial proof-of-concept experiments described in section 4.4 were concerned with the basic operation of the switch and the effects of gas pressure, charge voltage, charge polarity, and target material on the trigger range, run time, and jitter of the switch. These experiments were conducted with nitrogen as the switch gas. The results showed that the trigger range of the switch was weakly dependent on gas pressure, strongly dependent on polarity, and essentially independent of laser target material. The run time and jitter were also strongly dependent on charge voltage and polarity and independent of target material. In all cases, the cathode target polarity provided better performance – larger trigger range, lower run time, and lower jitter.

Based on the success of the proof-of-concept experiments, it was theorized that the threshold energy for triggering with this laser could be significantly lower than the full output. An experiment, described in section 4.5, was conducted to explore the limits of triggering at lower laser energy. This led to the surprising observation that reliable triggering was possible to an energy of less than 10 μJ for the cathode target polarity and less than 80 μJ for the anode target polarity. Another interesting result from this experiment was the very low observed dependence of run time and jitter on laser energy, as these variables have been previously shown to be strong functions of laser energy [74]. The ability to trigger the switch at such low energy opens the possibility of splitting the energy of this laser to trigger multiple switches or multiple spark channels in a single switch. These possibilities are under investigation in ongoing experiments.

While nitrogen is a gas commonly used in pressurized spark gaps, other gasses are also in common use and may be preferred by certain pulsed power engineers or for certain applications. The most common switch gasses other than nitrogen are air and sulfur hexafluoride (SF6). A series of experiments, described in section 4.6, were conducted to determine the effects of using each of these on the performance of the laser triggered operation of the test switch. The results showed that there were significant effects. In particular, both gasses reduced the charge polarity difference observed in the previous experiments. The SF6 also significantly increased the run time and jitter of the switch compared to nitrogen. It is thought that these differences can be attributed to the electronegativity of these gasses. This is supported by the increased effect of SF6 compared to air. Further investigation into the origin of this effect could provide important insight into the physics of the laser triggering processes, which are poorly understood.

The low energy of this laser makes the triggering of a gas switch dependent on the interaction of the laser with the surface of one of the electrodes. This leads to the natural question of laser-induced damage to the electrode. A series of experiments, described in section 4.7, were conducted to address this question. The results showed that, while the laser does create measurable damage of the electrode surface, it is relatively minimal compared to the damage caused by the subsequent discharge when the discharge parameters are typical of a compact pulsed power system. With a tungsten-copper laser target, a run to failure test concluded at 129,500 shots, which is a useful lifetime for a compact pulsed power system. The experiment with a graphite target gave a significantly lower lifetime, but this may have been caused more by the low quality of the graphite employed than the intrinsic suitability of graphite as a target material.

One recurring engineering challenge for incorporating laser triggering is beam transport from the laser to the switch. In addition to the problems of alignment, absorption of the laser energy in the system's insulating medium can become significant. For the 1535 nm wavelength employed in these experiments, absorption in

common dielectric gasses is not an issue, but the absorption in common insulating liquids was unknown. Thus, an experiment to measure the absorption in common insulating oils, described in section 4.8, was undertaken. The results of this experiment showed that the absorption is such that transport of the beam through more than a few cm of oil will likely cause unacceptable loss. This is important information for the potential application of this laser. Fortunately, the very small size of this type of laser opens up new packaging possibilities for the compact pulsed power engineer.

While the benefits of using this type of laser in a compact pulsed power system must be considered in the context of engineering the complete system, the results described in this chapter show that this type of laser has great promise. The low energy, compact size, and eye-safe wavelength of this laser are key features that will enable the incorporation of laser triggering into compact pulsed power systems. The benefits of laser triggering – especially the excellent triggering range, compact size, and galvanic isolation of the trigger electronics – will provide significant improvements in the field of compact pulsed power systems. The ability to operate reliably at lower percentages of self-break will improve switch recovery characteristics thus enabling higher repetition rates. The low power requirements – 0.5 W average at 10 Hz – and compact size of this laser system could provide significant advantages in size, weight, and power for a compact pulsed power system.

REFERENCES

[1] E. Schamiloglu, "Compact pulsed power requirements for high power microwaves," in *IEEE Symposium on Pulsed Power 2001*, 2001.

[2] X. Gu, Q. Shui, C. Jiang, Y. Sun and M. A. Gundersen, "High energy density ceramic film capacitors for compact pulsed power," in *Conference Record of the Twenty-Sixth International Power Modulator Symposium, 2004 and 2004 High-Voltage Workshop*, San Francisco, CA, 2004.

[3] S. Zhang et al, "High energy density film capacitors," in *2009 IEEE Pulsed Power Conference*, Washington, DC, 2009.

[4] X. Zhou, B. Chu, Y. Wang and Q. Zhang, "Polyvinylidene Fluoride based polymeric dielectrics for high energy density capacitor application," in *2009 IEEE 9th International Conference on the Properties and Applications of Dielectric Materials*, Harbin, 2009.

[5] K. A. O'Connor and R. D. Curry, "Recent results in the development of composites for high energy density capacitors," in *2014 IEEE International Power Modulator and High Voltage Conference (IPMHVC)*, Santa Fe, NM, 2014.

[6] J. R. Harris, "Multilayer High-Gradient Insulators," in *2006 International Symposium on Discharges and Electrical Insulation in Vacuum*, Matsue, 2006.

[7] J. G. Leopold et al, "More on High-Gradient Insulators," in *2005 IEEE Pulsed Power Conference*, Monterey, CA, 2005.

[8] R. J. Adler, J. Gilbrech and D. New, "Reducing PFN marx generator size using nested solid insulation," in *2011 IEEE Pulsed Power Conference*, Chicago, IL, 2011.

[9] C. D. Harjes et al, "Insulator Technologies to Achieve Maximum Electric Field Holdoff," in *2019 IEEE Pulsed Power & Plasma Science (PPPS)*, Orlando, FL, 2019.

[10] M. Giesselmann, B. McHale and T. Heeren, "New developments in high power capacitor charging technology," in *Conference Record of the Twenty-Sixth International Power Modulator Symposium, 2004 and 2004 High-Voltage Workshop*, San Francisco, CA, 2004.

[11] W. Shen, F. Wang, D. Boroyevich and C. W. Tipton IV, "High-Density Nanocrystalline Core Transformer for High-Power High-Frequency Resonant Converter," *IEEE Transactions on Industry Applications,* vol. 44, no. 1, pp. 213-222, 2008.

[12] D. Dayan, M. Evzelman and M. M. Peretz, "Multilevel High-Voltage Modular Rapid Capacitor Charger," in *2019 20th Workshop on Control and Modeling for Power Electronics (COMPEL)*, Toronto, ON, Canada, 2019.

[13] E. Schamiloglu, R. J. Barker, M. Gundersen and A. A. Neuber, "Modern Pulsed Power: Charlie Martin and Beyond," *Proc. IEEE,* vol. 92, no. 7, pp. 1014-1020, 2004.

[14] J. C. Martin, J.C. Martin on Pulsed Power, T. H. Martin, A. H. Guenther and M. Kristiansen, Eds., Boston, MA: Springer, 1996.

[15] K. Michals, "Project Y Atomic Bomb Detonator System," September 2012. [Online]. Available: https://www.flickr.com/photos/rocbolt/8061681156/in/photostream/. [Accessed March 2020].

[16] D. H. Hornig, "Low impedance switch". United States of America Patent US3956658A, 1976.

[17] J. C. Pouncey, "Optimizing Swap for Directed Energy –Detection of Buried Conductors with Low-Energy High-Voltage Pulses," University of New Mexico, Albuquerque, NM, 2017.

[18] M. V. Fazio and H. C. Kirbie, "Ultracompact Pulsed Power," *Proc. IEEE,* vol. 92, no. 7, pp. 1197-1204, 2004.

[19] S. F. Locke, "Blackout Bomb: Air Force's High-Powered Microwave Weapons Fry Enemy Equipment," *Popular Science,* July 2009.

[20] C. Basso, "Spark Gap Modeling," *Intuitsoft Newsletter,* no. 50, pp. 9-13, September 1997.

[21] M. Narui and F. P. Dawson, "A SPICE Model for Simulating Arc Discharge Loads," in *Conf. Rec. 1991 IEEE IAS Annual Mtg.*, Dearborn, MI, 1991.

[22] J. G. Zola, "Gas Discharge Tube Modeling With PSpice," *IEEE Trans. Electromagnetic Compatibility,* vol. 50, no. 4, pp. 1022-1025, November 2008.

[23] B. Martin, P. Raymond and J. Wey, "New Model for Ultracompact Coaxial Marx Generator Simulations," *Review of Scientific Instruments,* vol. 77, no. 4, April 2006.

[24] L. W. Nagel, "Life of Spice," April 2006. [Online]. Available: www.designers-guide.org/perspective/life-of-spice.pdf.

[25] C. Warwick, "Everything You Always Wanted to Know About SPICE but Were Afraid to Ask," *EMC Journal,* no. 82, pp. 27-29, 2009.

[26] M. Engelhardt, "LTspice IV Help File," Dec 2014. [Online]. Available: http://www.linear.com/designtools/software/#LTSPICE. [Accessed Mar 2020].

[27] T. H. Martin, "An empirical formula for gas switch breakdown delay," in *7th Pulsed Power Conf*, Monterey, CA, 1989.

[28] F. M. Bruce, "Calibration of uniform-field spark-gaps for high-voltage measurement at power frequencies," *J. Inst. Electr. Eng. - Part II: Power Eng.,* vol. 94, no. 38, pp. 138-149, 1947.

[29] H. H. Skilling and W. C. Brenner, "The electric strength of air at high pressure - II," *Trans. Am. Inst. Electr. Eng.,* vol. 60, no. 3, pp. 112-115, 1941.

[30] T. G. Engel, M. Kristiansen and A. L. Donaldson, "The pulsed discarge arc resistance and its functional behavior," *IEEE Trans Plasma Sci.,* vol. 17, no. 2, pp. 323-329, 1989.

[31] A. E. Vlastos, "The resistance of sparks," *J. Applied Phys.,* vol. 43, no. 4, pp. 1987-1989, 1972.

[32] M. Toepler, "Zur Kenntnis der Gesetze der Gleitfunkenbildung," *Ann. Phys.,* vol. 21, no. 2, pp. 193-222, 1906.

[33] M. J. Kushner, W. D. Kimura and S. R. Byron, "Arc resistance of laser triggered spark gaps," *J. Applied Phys.,* vol. 58, no. 5, pp. 1744-1751, 1985.

[34] S. I. Braginskii, "Theory of the development of a spark channel," *J. Exp. Theor. Phys.,* vol. 34, pp. 1068-1074, 1958.

[35] C. Basso, "SPICE analog behavioral modeling of variable passives," *Power Electronics,* p. 57, April 2005.

[36] F. W. Grover, "Parallel Elements of Equal Length," in *Inductance Calculations*, Mineola, NY, Dover Publications Inc., 2009, p. 35.

[37] S. E. Calico, M. C. Scott and M. C. Clark, "Development of a compact Marx generator for high-power microwave applications," in *Digest of Tech. Papers, 11th IEEE Int. Pulsed Power Conf.*, Baltimore, MD, 1997.

[38] A. Sharma, "Development and Characterization of Repetitive 1-kJ Marx-Generator-Driven Reflex Triode System for High-Power Microwave Generation," *IEEE Trans. Plasma Sci.,* vol. 39, no. 5, pp. 1262-1267, 2011.

[39] D. H. Barnett, K. Rainwater, J. C. Dickens, A. A. Neuber and J. J. Mankowski, "160 J, 100 HZ repetition rate, compact Marx generator and high power microwave system," in *Proc. of the IEEE Int. Pulsed Power Conference*, Austin, TX, 2017.

[40] J. R. Mayes and W. J. Carey, "The direct generation of high power microwaves with compact Marx generators," in *14th Int Conf on High-Power Particle Beams (BEAMS)*, Albuquerque, NM, 2002.

[41] C. J. Buchenauer, Interviewee, [Interview]. September 2017.

[42] M. Skipper, Interviewee, [Interview]. July 2017.

[43] J. M. Lehr and P. H. Ron, "Marx Generators and Marx-Like Circuits," in *Pulsed Power Technology*, Hoboken, NJ, IEEE Wiley, 2017, pp. 1-57.

[44] J. M. Lehr and P. H. Ron, "Closing Switches," in *Pulsed Power Teechnology*, Hoboken, NJ, IEEE Wiley, 2017, pp. 147-235.

[45] R. W. Morrison and A. M. Smith, "Overvoltage and breakdown patterns of fast Marx generators," *IEEE Trans. Nuclear Sci.,* vol. 19, no. 4, pp. 20-31, 1972.

[46] J. F. Francis, "High Voltage Pulse Techniques," Lubbock, TX, 1976.

[47] J. R. Mayes, W. J. Carey, W. C. Nunnally and L. Altgilbers, "Sub-nanosecond jitter operation of Marx generators," in *Proc. 2001 Pulsed Power and Plasma Sci. Conf.*, Las Vegas, NV, 2001.

[48] C. J. Buchenauer, "Optimizing compact Marx generator networks," *IEEE Trans. Plasma Sci.,* vol. 38, no. 10, pp. 2771-2784, 2010.

[49] D. Goerz, "An ultra-compact Marx-type high-voltage generator," in *Proc. 2001 Pulsed Power and Plasma Sci. Conf.*, Las Vegas, NV, 2001.

[50] D. A. Platts, "10 Joule High voltage Trigger MicroMarx," in *Proc. Int. Pulsed Power conference*, Lubbock, TX, 1981.

[51] M. Kekez, "Simple Sub-50-ps Rise-Time High Voltage Generator," *Review of Scientific Instruments,* vol. 62, no. 12, pp. 2924-2930, 1991.

[52] F. E. Peterkin, D. C. Stoudt, B. J. Hankla, K. A. Boulais and J. S. Bernardes, "Performance characteristics of a 1 MV miniature Marx bank," in *Digest of Technical Papers. 12th IEEE International Pulsed Power Conference*, Monterey, CA, 1999.

[53] J. R. Mayes, M. G. Mayes and M. B. Lara, "A Novel Marx Generator Topology Design for Low Source Impedance," in *2005 IEEE Pulsed Power Conference*, Monterey, CA, 2005.

[54] J. Benford, J. A. Swegle and E. Schamiloglu, High Power Microwaves - Second Edition, Boca Raton, FL: CRC Press, 2007.

[55] D. A. Phelps, "High density compact tunable PFN-Marx modulators," in *Nineteenth IEEE Symposium on Power Modulators*, San Diego, CA, 1990.

[56] M. M. Kekez, "PFN-MARX pulsers for HPM testing application," in *1996 11th International Conference on High-Power Particle Beams*, Prague, Czech Republic, 1996.

[57] H. Li, H. Ryoo, J. Kim, G. Rim, Y. Kim and J. Deng, "Development of Rectangle-Pulse Marx Generator Based on PFN," *IEEE Trans. Plasma Sci.,* vol. 39, no. 1, pp. 190-194, 2009.

[58] F. Lassalle, "Development and Test of a 400-kV PFN Marx With Compactness and Rise Time Optimization," *IEEE Trans. Plasma Sci.,* vol. 46, no. 10, pp. 3313-3319, 2018.

[59] D. Platts, M. P. Hockaday, D. Beck, W. Coulter and R. C. Smith, "Compact flash X-ray units," in *Digest of Technical Papers. Tenth IEEE International Pulsed Power Conference*, Albuquerque, NM, 1995.

[60] F. J. McClung and R. W. Hellwarth, "Characteristics of giant optical pulsations from ruby," *Proc. IEEE,* vol. 51, no. 1, pp. 46-53, 1963.

[61] R. G. Meyerand and A. F. Haught, "Gas breakdown at optical frequencies," *Phys. Rev. Lett.,* vol. 11, no. 9, pp. 401-403, 1963.

[62] W. K. Pendleton and A. H. Guenther, "Investigation of a laser triggered spark gap," *Rev. Sci. Inst,* vol. 36, no. 11, pp. 1546-1550, 1965.

[63] A. H. Guenther and J. Bettis, "Laser-triggered megavolt switching," *IEEE J. Quantum Elect.,* vol. 3, no. 11, pp. 581-588, 1967.

[64] A. H. Guenther and R. H. McKnight, "Aa laser-triggered 50 PPS high-voltage switch with nanosecond jitter," *Proc. IEEE,* vol. 55, no. 8, p. 1504, 1967.

[65] W. R. Rapoport, J. Goldhar and J. R. Murray, "KrF Laser-Triggered SF6 Spark Gap for Low Jitter Timing," *IEEE Trans. Plasma Sci,* vol. 8, no. 3, pp. 167-170, 1980.

[66] D. R. Humphreys, "RIMFIRE, a six megavolt laser-triggered gas-filled switch for PBFA II," in *Proc. 5th IEEE Pulsed Power Conf.*, Arlington, VA, 1985.

[67] A. E. Siegman, "Defining, measuring, and optimizing laser beam quality," *Proc. SPIE 1868, Laser Resonators and Coherent Optics: Modeling, Technology, and Applications,* 1993.

[68] P. Yankov, "Cr4+:YAG Q-switching of Nd:host laser oscillators," *J. Phys. D: Appl. Phys.,* vol. 27, pp. 1118-1120, 1994.

[69] S. J. Hamlin, A. D. Hays, C. W. Trussell and V. King, "Eyesafe Erbium Glass Microlaser," *Proc. SPIE 5332, Solid State Lasers XIII: Technology and Devices,* 2004.

[70] J. M. Lehr, *Unpublished,* 2011.

[71] D. L. Sullivan, S. D. Kovaleski, B. T. Hutsel and J. M. Gahl, "Study of laser target triggering for spark gap switches," *IEEE Trans. Dielectrics and Electrical Insulation,* vol. 16, no. 4, pp. 956-960, 2009.

[72] V. N. Rai and S. N. Thakur, Laser-Induced Breakdown Spectroscopy, Amsterdam: Elsevier, 2007.

[73] S. J. MacGregor, F. A. Tuema and S. M. Turnbull, "Repetitively operated spark gap switches," in *'94 IEE Colloquium on Pulsed Power*, London, UK, 1994.

[74] A. H. Guenther and J. R. Bettis, "A review of laser-triggered switching," *Proc. IEEE,* vol. 59, no. 4, pp. 689-697, 1971.

[75] S. H. Khan and D. Walsh, "Effect of cathode material in a laser triggered spark gap," *J. Phys. D: Appl. Phys,* vol. 4, no. 2, 1971.

[76] A. L. Donaldson and M. Kristiansen, "The Erosion Performance Of Graphite Electrodes In High Current, High Coulomb, Spark Gaps," in *Eighth IEEE International Conference on Pulsed Power*, San Diego, CA, 1991.

[77] L. Dong, M. Ahangarkani, W. Chen and Y. Zhang, "Recent progress in development of tungsten-copper composites: Fabrication, modification and applications," *International Journal of Refractory Metals and Hard Materials,* vol. 75, pp. 30-42, 2018.

[78] A. Larsson, D. Yap, J. Au and T. E. Carlsson, "Laser-triggering of spark gap switches," in *2013 19th IEEE Pulsed Power Conference (PPC)*, San Francisco, CA, 2013.

[79] H. C. Harjes et al, "Laser Triggering through Fiber Optics of a Low Jitter Spark Gap," *IEEE Trans. Plasma Sci.,* vol. 8, no. 3, pp. 170-176, 1980.

[80] S. F. Glover et al, "Laser triggering of spark gap switches with less than 100μJ's of energy," in *2007 16th IEEE International Pulsed Power Conference*, Albuquerque, NM, 2007.

[81] J. R. Rumble, Ed., CRC Handbook of Chemistry and Physics, 100th Edition (Internet Version 2019), Boca Raton, FL: CRC Press/Taylor & Francis, 2019.

[82] J. R. Beveridge, S. J. Macgregor, M. J. Given, I. V. Timoshkin and J. M. Lehr, "A corona-stabilised plasma closing switch," *IEEE Transactions on Dielectrics and Electrical Insulation,* vol. 16, no. 4, pp. 948-955, 2009.

[83] J. M. Meek and J. D. Craggs, Electrical Breakdown of Gasses, London: Oxford at the Clarendon Press, 1953.

[84] Airgas, an Air Liquide Company, "Specialty Gasses and Equipment Product Reference Guide," Feb 2018. [Online]. Available: http://airgassgcatalog.com/catalog/. [Accessed March 2020].

[85] J. R. Woodworth, R. G. Adams and C. A. Frost, "UV-Laser Triggering of 2.8-Megavolt Gas Switches," *IEEE Trans. Plasma Sci.,* vol. 10, no. 4, pp. 257-261, 1982.

[86] N. D. Zameroski et al., "Multimegavolt Laser-Triggered Gas Switching With a Green Laser and Beam Transport Through Water," *IEEE Trans. Plasma Sci.,* vol. 35, no. 3, pp. 696-701, 2007.

[87] K. F. Palmer and D. Williams, "Optical Properties of Water in the Near Infrared,," *J. Optical Soc. America,* vol. 64, no. 8, pp. 1107-1110, 1974.

[88] Royal Dutch Shell PLC, *The Perfect Partner,* 2014.

[89] The Dow Chemical Company, *XIAMETER™ 561 Silicone Transformer Liquid,* 2019.

[90] W. McDermid, M. Partyka and T. Black, "Experience with ISO-Paraffinic Insulating Oil for Power Transformers," in *IEEE International Conference on High Voltage Engineering and Application (ICHVE)*, Athens, Greece, 2018.

[91] S. Karmakar, A. Dutta and H. Kalathiripi, "Investigation of the Effect of High Voltage Impulse Stress on Transformer Oil by Infrared Spectroscopy," in *2019 International Conference on High Voltage Engineering and Technology (ICHVET)*, Hyderabad, India, 2019.

[92] QC Lubricants, "Shell Diala S2 ZX-A," [Online]. Available: https://qclubricants.com/aeroshell/diala.htm. [Accessed 25 Nov 2019].

[93] N. Lukenda and P.-C. L. I. Technical Services Advisor – LUMINOL Dielectric Insulating Liquids, Interviewees, [Interview]. October 2019.

[94] J. C. Pouncey and J. M. Lehr, "A spark gap model for LTspice and similar circuit simulation software," in *2015 IEEE Pulsed Power Conference (PPC)*, Austin, TX, 2015.